

Systematic Control Strategy for Inverter-Based Microgrids

by

Po-Hsu Huang

B.S., Electrical Engineering, National Cheng Kung University (2007)

M.S., Electrical Engineering, National Taiwan University (2009)

M.S., Electrical Power Engineering, Masdar Institute of Science and
Technology (2013)

Submitted to the

Department of Electrical Engineering and Computer Science
in partial fulfillment of the requirements for the degree of

Doctor of Philosophy

at the

MASSACHUSETTS INSTITUTE OF TECHNOLOGY

February 2019

© Massachusetts Institute of Technology 2019. All rights reserved.

Author
.....

Department of Electrical Engineering and Computer Science
December 19, 2018

Certified by
.....

James L. Kirtley
Professor of Electrical Engineering and Computer Science
Thesis Supervisor

Accepted by
.....

Leslie A. Kolodziejski
Professor of Electrical Engineering and Computer Science
Chair, Department Committee on Graduate Students

Systematic Control Strategy for Inverter-Based Microgrids

by

Po-Hsu Huang

Submitted to the
Department of Electrical Engineering and Computer Science
on December 19, 2018, in partial fulfillment of the
requirements for the degree of
Doctor of Philosophy

Abstract

Small-scale power systems, microgrids (MGs), are becoming economically and technically feasible due to cost-effective battery storage with high-bandwidth inverter interfaces, thus facilitating efficient energy utilization from renewable sources to maintain autonomous operation without a grid connection. Therefore, control of inverter-based or inverter-dominant systems is gaining a lot of attention while posing different challenges compared to traditional power systems.

Conventional droop-based control architectures can provide power-sharing capability, and are considered to be a cost-effective and reliable solution for microgrids. However, experimental studies have revealed that for small-scale microgrids, stability is significantly compromised by the droop control due to low X/R ratios and short lines. Therefore, a proper modeling framework for obtaining concise and accurate models becomes important to understand the physical nature of the instability. Such a framework can further facilitate a systematic control design for stability enhancement, allowing the development of power-sharing strategies and plug-and-play functionality for efficient microgrid operation.

In this thesis, high-fidelity reduced-order models for microgrids are first developed and investigated. Then, based on the proposed models, concise and simple stability certificates are derived along with virtual impedance methods for local and global stability enhancement. Detailed discussions are carried out on the control design that aims at achieving both droop stability and controller robustness. Finally, a power and energy management scheme based on secondary compensation is developed to enhance operational efficiency. The integrated solution provides a comprehensive reference for the development of stable, reliable, and flexible inverter-based microgrids. All results are validated through both simulation and experimental studies.

Thesis Supervisor: James L. Kirtley

Title: Professor of Electrical Engineering and Computer Science

Acknowledgments

My deepest appreciation goes to my advisor, Prof. James L. Kirtley for his continuous support of my research, for his patience, guidance, and encouragement. I will never forget about his valuable advice and suggestions. He was always there for me whenever I needed him and I feel really privileged to have him as my research advisor and, also, my life mentor. I would also like to show my sincere gratitude to my thesis committee member: Prof. Konstantin Turitsyn and Prof. David Perreault. They were always open for any discussion from theoretical frameworks, mathematical derivations, to microgrid experiment. Special thanks to Prof. Steven Leeb for his great efforts on renovating the lab space so I can complete productive tasks for my experiment.

I also want to thank my collaborators and co-authors: Dr. Petr Vorobev, Dr. Jorge Elizondo Martinez, Prof. Mohamed Al Hosani, Prof. Weidong Xiao, Prof. Jimmy Peng, Dr. Richard Zhang, and Salish Maharjan. Great appreciation for their significant efforts on all the collaborative projects. I cannot imagine how I would have accomplished all the projects without their support.

My sincere thanks also go to the Picogrid team members for their tremendous time and effort spent on the experimental prototype: Colm O'Rourke and Matthew Overlin. Moreover, I would like to thank the people who helped in the Picogrid project: Eoin Fallon, Edwin Fonkwe, Mohammad Qasim, Krishan Kant, and Nelson Wang.

Besides, I would like to thank the people in the Laboratory of Electromagnetic and Electronic Systems (LEES), for all the time we spent together for solving research problems, completing problem sets, and accomplishing group projects. Particularly, I would like to express my sincere gratitude to Alex Hanson, Lukasz Huchel, Manuel Gutierrez, Alexander Jurkova, Yiou He, Rakesh Kumar, Anas Al Bastami, Juan Santiago, and David Otten.

A special mention to my Taiwanese friends in Cambridge who are the source of my energy to push forward and I am deeply grateful for all their emotional and physical

support. More importantly, I want to thank my parents who raised me and educated me so I am able to be here to accomplish my Ph.D. degree.

Finally, this work was funded by Masdar Institute of Science and Technology and Khalifa University and the real-time platform was supported by Typhoon HIL. Many thanks to them as this work would not happen without their financial assistance.

Contents

1	Introduction	17
1.1	Background	17
1.2	Power Sharing for Microgrids	20
1.3	Droop Instability	26
1.4	Contributions	28
1.5	Thesis Organization	29
2	Modeling of Droop-Controlled Inverter-Based Microgrids	31
2.1	Introduction	31
2.2	5 th -order Electromagnetic Model	36
2.3	Model Order Reduction	38
2.3.1	3 rd -order Conventional Model	38
2.3.2	3 rd -order High-Fidelity Model	40
2.4	Network Generalization	45
2.5	Model Accuracy and Efficiency	48
2.6	Conclusions	51
3	Stability Assessment	53
3.1	Introduction	53
3.2	Two-Bus Example	53
3.3	Network Generalization	58
3.4	Conclusions	59

4 Stability Enhancement	61
4.1 Introduction	61
4.2 Approximated Stability Rules	62
4.3 Plug-and-Play Compliant Control Rules	66
4.4 Power Sharing of Multiple Inverters	68
4.5 Implementation of Virtual Impedances	70
4.5.1 Conventional Virtual Impedance Control	70
4.5.2 Proposed Virtual Impedance Control	73
4.5.3 Voltage and Power Quality	77
4.6 Conclusions	78
5 Secondary Compensation	79
5.1 Introduction	79
5.2 Set-Point Restoration	81
5.2.1 Naive Compensation	81
5.2.2 Average Secondary Compensation	82
5.3 Power Dispatch via Secondary Compensation	84
5.4 Conclusions	85
6 Validation	87
6.1 Introduction	87
6.2 Stability Region	87
6.3 Time-domain Analysis	90
6.3.1 Droop Control	90
6.3.2 Secondary Compensation	95
6.4 Conclusions	97
7 Conclusions and Future Work	99
7.1 Conclusions	99
7.2 Future Work	100

Appendix A Derivations and Notes	103
A.1 Generalized Stability Criteria for Networks	103
A.2 Two-Loop Control	104
Appendix B Microgrid Validation	107
B.1 Detailed Average Simulation Models	107
B.1.1 Realization of ODEs	107
B.1.2 dq reference frames	108
B.1.3 Networks and loads	109
B.2 Small-Signal Analysis	111
B.3 Experimental Prototype	112
B.3.1 System Modules	112
B.3.2 Central Control Center	114
B.3.3 Inverter Module	115
B.3.4 Measurement Unit	117
B.3.5 Communication and Peripherals	118
B.3.6 Load and Network	118

List of Figures

1-1	Two DC sources and a load.	20
1-2	Two DC sources and a load with virtual resistances.	22
1-3	DC droop chart.	23
1-4	Simple two-bus AC circuit.	23
1-5	AC droop charts.	24
1-6	Eigenvalue locus of a typical inverter-based microgrid: (a) Zoom-out plot; (b) Zoom-in plot.	27
2-1	(a) Single phase representation of the three-phase inverter system connected to the PCC; (b) Internal control; (c) Droop (Power) Control. .	32
2-2	Phasor diagram of the relationship between rotating and stationary reference frames.	34
2-3	Comparison of stability regions predicted by the 5 th -order EM and 3 rd -order conventional models: $X = 0.42\%$, $R = 0.28\%$, and $\tau = 0.0318$. .	38
2-4	Variation of B' with respect to: (a) Line length (km); (b) X/R ratio. .	42
2-5	Comparison of stability regions predicted by different models: $Z = 0.5\%$; (a) $X/R = 0.7$; (b) $X/R = 1.0$; (c) $X/R = 1.7$	43
2-6	Zoom-in comparison of stability regions predicted by different models: $Z = 0.5\%$; (a) $X/R = 0.7$; (b) $X/R = 1.0$; (c) $X/R = 1.7$	44
2-7	System configuration of inverter-based microgrid under study.	49
2-8	Dynamic responses (with adjusted initial conditions) of different models with different droop gains. (a) $k_p = 0.5\%$, $k_q = 3\%$. (b) $k_p = 1.3\%$, $k_q = 3\%$	50

2-9	Eigenvalue plots of different models ($k_p = 0.35\% - 1.23\%$).	51
3-1	Small-signal stability regions of the two-bus system based on different models with respect to the voltage and frequency droop gains ($ Z = 3\%$): (a) $X/R = 0.667$; (b) $X/R = 1$; (c) $X/R = 1.5$	57
4-1	Variation of $B'\omega_0$ and Γ with respect to the line length ($X_{mc} = R_{mc}1\%$, and $X_l/R_l = 0.5$).	62
4-2	Star topology of a microgrid by aggregating the network into a single node.	63
4-3	Comparison of low-dimensional projected stability regions of (4.17) and (2.51) for a microgrid with five inverters ($n = 5$, star topology) of different scales with symmetric droop gains and controlled impedances: $k_{p,i} = k_p$, $k_{q,i} = k_q$, $X_{mc,i} = R_{mc,i} = 2\%$ (line parameters are shown in Table 4.1).	67
4-4	Comparison of projected stability regions with respect to k_{p1}, k_{p4} : $X_{mc,i} = R_{mc,i} = 2\%$; (a) $k_{p2} = k_{p3} = k_{p5} = 4\%$, $k_{q,i} = 0\%$; (b) $k_{p2} = k_{p3} = k_{p5} = 3\%$, $k_{q,i} = 1\%$, (c) $k_{p2} = k_{p3} = k_{p5} = 2\%$, $k_{q,i} = 2\%$ (line parameters are shown in Table 4.1).	69
4-5	Comparison of projected stability regions with respect to k_{p1}, k_{p4} : $X_{mc,i} = R_{mc,i} = 2\%$, $k_{p2} = k_{p3} = k_{p5} = 4\%$, $k_{q,i} = 0\%$ (line parameters are shown in Table 4.1).	70
4-6	Equivalent circuit of the virtual impedance.	71
4-7	Block diagram of the virtual reactance method.	73
4-8	Bode plots of (4.24) for different X_m (zero line length).	73
4-9	(a) Filter current injection into the PCC; (b) Block diagrams of the internal control.	74
4-10	The equivalent circuit of (4.27).	75
4-11	The equivalent circuit of the virtual impedance.	75
4-12	Bode plots of the transfer functions with different line lengths.	76

4-13 Output voltage responses for a sudden load change (1 pu resistive) with different controlled impedances (virtual and coupling impedances)	77
5-1 Hierarchical control of AC Microgrids [1]	80
6-1 Three-inverter test system	88
6-2 Comparison of projected stability regions: $k_{p,i} = k_p/s_i$, $k_{q,i} = k_q/s_i$, $X_{mc,i} = R_{mc,i} = 2/s_i\%$	88
6-3 Comparison of projected stability regions with respect to k_{p1} and k_{p2} : $s_1 : s_2 : s_3 = 1 : 0.67 : 0.33$, $X_{mc,i} = R_{mc,i} = 2/s_i\%$; (a) $k_{q,i} = 0$, $k_{p3} = 12.12\%$; (b) $k_{q,i} = 2/s_i\%$, $k_{p3} = 6.06\%$	90
6-4 Time-domain results for a step change of sharing ratios, s_i , form 1 : 1 : 1 to 1 : 0.67 : 0.33: $k_{p,i} = k_{q,i} = 2/s_i\%$, $X_{mc,i} = R_{mc,i} = 2/s_i\%$; (a) Output voltages; (b) Filtered active power.	91
6-5 Time-domain results for a step change of sharing ratios, s_i , form 1 : 1 : 1 to 1 : 0.67 : 0.33: (a) Filtered reactive power; (b) Frequency.	92
6-6 Droop oscillations beyond critically stable conditions: sharing ratios 1 : 0.67 : 0.33, $X_{mc,i} = R_{mc,i} = 2/s_i\%$; (a) $k_{p,i} = \sim 2.8/s_i\%$, $k_{q,i} = 2/s_i\%$; (b) $k_{p,i} = \sim 4.3/s_i\%$, $k_{q,i} = 0/s_i\%$	93
6-7 Dynamic responses of output voltages during load stepping: sharing ratios 1 : 0.67 : 0.33, $k_{p,i} = 2/s_i\%$, $k_{q,i} = 2/s_i\%$; (a) $X_{mc,i} = R_{mc,i} = 2/s_i\%$; (b) $X_{mc,i} = R_{mc,i} = 5/s_i\%$	94
6-8 Dynamic responses of filtered active power during load stepping: sharing ratios 1 : 0.67 : 0.33, $k_{p,i} = 2/s_i\%$, $k_{q,i} = 2/s_i\%$; (a) $X_{mc,i} = R_{mc,i} = 2/s_i\%$; (b) $X_{mc,i} = R_{mc,i} = 5/s_i\%$	95
6-9 Time-domain results for the activation of the secondary compensation: $k_{p,i} = k_{q,i} = 4/s_i\%$, $X_{mc,i} = R_{mc,i} = 5/s_i\%$; (a) Output voltages; (b) Filtered active power.	96
6-10 Time-domain results for the activation of the secondary compensation: $k_{p,i} = k_{q,i} = 4/s_i\%$, $X_{mc,i} = R_{mc,i} = 5/s_i\%$; (a) Filtered reactive power; (b) frequency.	97

A-1	Circuit diagram of the inverter system.	104
B-1	Simulink model of the droop control in equations (2.16)-(2.18).	108
B-2	An example of a load bus	111
B-3	System diagram of the experimental prototype.	112
B-4	Photograph of the entire system.	113
B-5	Photograph of the central controller board and the relay drivers.	114
B-6	Screenshot of the LabVIEW control panel.	115
B-7	Photograph of the local controller board and inverter.	116
B-8	Photograph of the measurement unit.	117
B-9	Photograph of the network.	119
B-10	Photograph of the inductive load bank.	119
B-11	Photograph of the resistive load bank.	120

List of Tables

2.1	Parameters of Five Inverter-Based Microgrid	51
2.2	Computational Time Comparison	52
4.1	Distances in Kilometers to PCC of Five-Inverter Test Cases: $X_l = 0.28\%\text{km}^{-1}$, $R_l = 0.56\%\text{km}^{-1}$	66
6.1	Parameters of Three Inverter Test System	89

Chapter 1

Introduction

1.1 Background

Recent development in renewable energy technologies, cost-effective storage devices, and high-bandwidth power electronics inverters lead to increased interest in microgrid (MG) development. The advantages given by introducing microgrids are their capability in operating in both islanded and grid-connected modes. Such a functionality allows microgrids to provide flexibility to maintain the local supply in case of any grid contingencies [2–4]. In grid-connected modes, inverters are normally operating in current-controlled modes with voltage and frequency references provided by the presence of the grid. Any power imbalance is, therefore, handled by interconnections. With the increasing share of distributed generation and battery storage, the possibility of islanded operations becomes more likely and thus there is an urgent need for the proper control of individual inverters in islanded modes [2, 5].

Various research works in recent years have investigated intensively in microgrid control for islanded operations [6–12]. Among different control schemes, droop-based control is widely appreciated due to many advantages such as power-sharing capability without communication, high reliability, expandability with Plug-and-Play (PnP) functionality, and similar power control structure to synchronous machine systems [1, 6, 10, 13].

Droop control is based only on the local actions that allow desired power distri-

bution among multiple inverters operating in islanded modes, which ensures proper power sharing and system resiliency. The strong coupling of active power to frequency and reactive power to voltage due to high X/R ratios allows such adoption for the conventional power systems. Similarly, such a strategy was proposed for the inverters connected to AC grids [14] or inverter-based microgrids (IBMGs) [1, 10, 13]. However, due to much smaller X/R ratios, which are around unity for IBMGs [13], the coupling between power and frequency becomes distorted, due to which studies have hypothesized limited small-signal stability regions for allowable droop gains as compared to conventional power systems [15]. To investigate this issue, most studies utilized a seem-to-be-reasonable assumption by neglecting electromagnetic network dynamics (an approximation routinely used for conventional power systems) based on the justification of a distinct time scale separation between network and power control modes [16–19]. However, both experimental and detailed simulation results for IBMGs have shown that true stability regions are much smaller than the ones obtained from such a quasi-stationary approximation, signifying the importance of electromagnetic transients despite their small time scale [13, 20]. In a recent work [21], the influence of these fast dynamics on slow power controller modes had been analytically demonstrated. In particular, for typical IBMGs, the small relative impedance of networks (strong coupling between different inverters) was identified as one of the main reasons for instability, which is fully consistent with the experimental results presented in [22].

Before the recognition of the importance of electromagnetic transients, the idea of suppressing the natural strong coupling in IBMGs had led to various studies aiming at the increase of effective line impedance by physical or virtual means [19, 23–28]. Particularly, the emulation of inductive dynamics through digital controllers helps to save bulky and costly inductors with enhancement of power sharing accuracy and stability. In general, the emulation is realized by manipulating voltage set-points with output current measurements to mimic the dynamic behavior of impedances, so that an inverter behaves like an internal voltage source connected to its terminal through a virtual impedance [23]. However, proper sizing of virtual impedance for droop

instability was not well covered in literature. In fact, the conventional approaches rely on either detailed models based on eigenvalues analysis [22] or very simplified models, like Kuramoto’s oscillators [16]. Working with the detailed models of high order is very non-intuitive and time-consuming while simplified models tend to be erroneous in predicting true stability boundaries [21]. Thus, there is a practical need to develop a guideline that maintains both simplicity and fidelity for control engineers.

The foundation of the proposed work is the development of a systematic approach for stability enhancement from an analytic perspective. The problem is first formulated using a simple two-bus example and reduced-order models are then presented in consistent with the framework proposed in [21] to allow physical insights into the origin of droop instability. Lyapunov function candidates are proposed based on the reduced-order models to obtain concise stability criteria, followed by further generalization to network settings. Finally, Plug-and-Play (PnP) compliant control rules for sizing virtual and coupling impedances are obtained, allowing for simple and flexible integration of inverters into microgrids by satisfying only a set of local rules.

With the desired amount of virtual impedance based on the proposed PnP rules, control schemes are then investigated. For the standard voltage/current two-loop controllers, placing an additional feedback loop to realize virtual impedance might compromise closed-loop stability, especially when the amount of impedance added is significant as compared to physical lines. As such, the proper choice of the size of virtual impedance becomes critical. That is, one has to enhance the stability region for droop control without compromising the stability of inverter internal control loops. Following that a new method for virtual impedance is proposed to eliminate the redundant voltage control loop. Such an architecture allows for a significant increase of the margin for virtual impedance, thus enabling more flexibility.

Finally, it has been pointed out that droop control enables certain flexibility of power sharing, but it also induces set-point deviations. Therefore, the last part of the thesis focuses on the secondary control scheme that restores the frequency and voltage set points. Moreover, enhanced features of power dispatch functionality and energy management based on the secondary compensation is developed to allow

further flexibility for microgrid operations.

1.2 Power Sharing for Microgrids

The main objective of MG operation is to maintain both power sharing and power balance based on pre-defined set-points for voltage and frequency. In many applications, the Master-Slave architecture has been commonly adopted due to the ease of control design. In such a scheme, a selected unit with an oversized capacity is normally referred as *Master*, whereas other units are referred as *Slave*. The function of a master is to take on the responsibility of regulating both voltage and frequency and, additionally, dispatching signals through communication channels to the slaves so as to achieve power balance. The quality of power balance heavily depends on the capacity of a master to absorb transient energy mismatch and communication bandwidth to frequently command slaves for adjusting their power output. That is, there is an essential trade-off between the size of a master and communication bandwidth. Also, such systems are likely to suffer from reliability issues due to heavy reliance on communication or an oversized master for maintaining power balance. Therefore, it is not a favorable option for microgrid operations as systems become quite vulnerable to failures and disturbances.

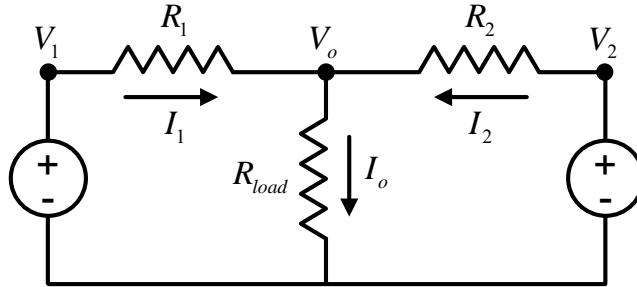


Figure 1-1: Two DC sources and a load.

A more desirable option is to employ the commonly-used droop control, which is based on local actions without the need of communication. In such a setting, individual units pre-define their set-points and negotiate through the droop mechanism.

There is no need to employ hierarchy among the units; thus, every unit is a master or there is simply no master in the system. The advantage given is that the system becomes highly resilient to failures since there is no oversized master and the control can operate without communication.

To illustrate the core concept of droop control for power sharing, a simple DC example is used to illustrate the problem. Consider now a case with two DC sources, two cables, and a resistive load shown in Fig. 1-1. The objective here is to share the load equally among two sources. Since there is no communication, two sources are given the identical set-points ahead of the operation so that, ideally, they are expected to supply the same amount of current. However, in reality, voltage regulation is far from perfect so that there exists small voltage differences (reference errors) between sources. Given a particular set of numerical values: $V_1 = 1.5V$, $V_2 = 1.49V$, $R_1 = R_2 = 10\text{m}\Omega$, $R_{load} = 7.5\Omega$, the solution of the system can be computed as: $I_1 = 599\text{mA}$, $I_2 = 400\text{mA}$, $V_o = 1.494V$, and $I_o = 199\text{mA}$. The results are not desired as the intention is to ensure equal current sharing (100mA each) among the sources. In this scenario, the source 1 is actually charging both the load and source 2. This current, flowing through the source 2, is normally referred as *circulating current*. The remedy for such an issue is to increase the resistance of the cables. For example, an increase of both cable resistances to 1Ω leads to a new solution of the system: $V_o = 1.401V$, $I_1 = 99\text{mA}$, $I_2 = 88\text{mA}$, and $I_o = 187\text{mA}$. Although the current sharing is much improved, the cables induce significant energy losses due to their high resistance. In addition, the voltage at the load side is significant lower due to some voltage drops across the cables. In general, such a solution is not practical, but the idea of increasing cable resistance does give an insight for preventing circulating current and improving current sharing. A more ideal solution is to regulate the source in a way that it appears as like an internal voltage source connected in series to a virtual resistance as shown in Fig. 1-2. The control can be realized by using the

following rules:

$$V_1 = V_1^{set} - R_1^* I_1 \quad (1.1)$$

$$V_2 = V_2^{set} - R_2^* I_2 \quad (1.2)$$

where V_1^{set} and V_2^{set} denote the internal voltage set-points and R_1^* and R_2^* are the virtual resistances, which are in fact referred as *droop gains* in DC systems since they result in the *droop* drop of the output voltage. The effect of these droop terms can be illustrated using the droop chart shown in Fig. 1-3. It can be seen that the larger droop gains improve current sharing between the sources while causing greater droop drops (voltage drops).

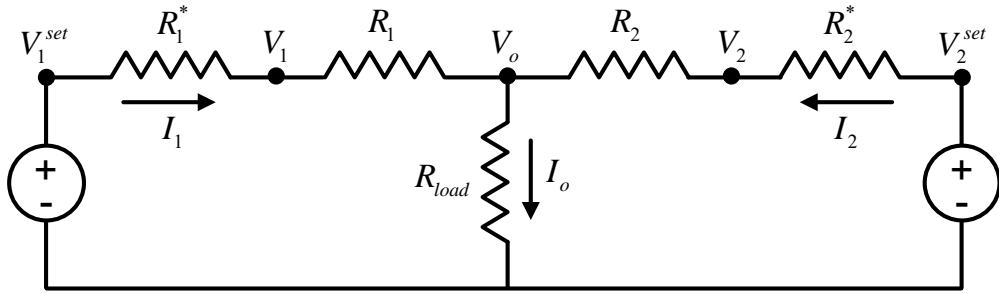


Figure 1-2: Two DC sources and a load with virtual resistances.

In DC systems, the linear coupling between voltage and current is straightforward so that the resistive behavior of the droop term is used. However, the coupling relationship in AC systems becomes more complicated. Consider an example with two AC sources and an inductive line, as shown in Fig. 1-4. The steady-state power flow equations can be described as:

$$P = \frac{VV_s \sin \theta}{X} \quad (1.3a)$$

$$Q = \frac{VV_s \cos \theta}{X} - \frac{V_s^2}{X} \quad (1.3b)$$

where X is the reactance between the sources, V and V_s represent voltage magnitudes with the subscript s denoting a stiff source, and θ is the angle deviation between two

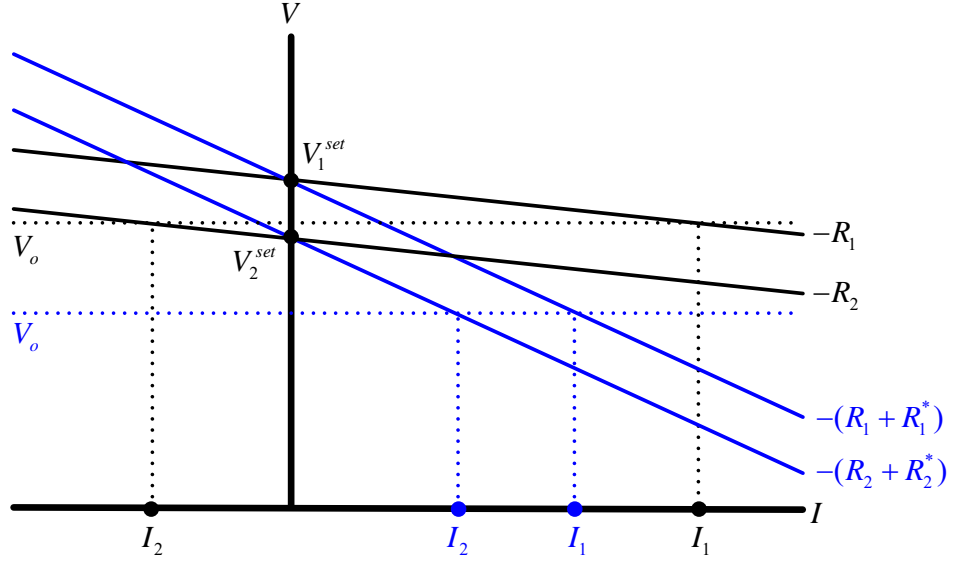


Figure 1-3: DC droop chart.

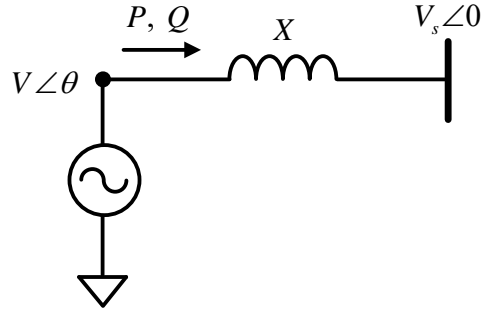


Figure 1-4: Simple two-bus AC circuit.

sources. These correlations are essentially non-linear; thus, small perturbations on both V and θ are applied to obtain (linearization):

$$\delta P = \frac{V_s \sin \theta}{X} \delta V + \frac{V_s \cos \theta}{X} \delta \theta \quad (1.4a)$$

$$\delta Q = \frac{V_s \cos \theta}{X} \delta V - \frac{V_s \sin \theta}{X} \delta \theta \quad (1.4b)$$

where the terms with $\sin \theta$ can be neglected due to a near-zero angle deviation by

assuming a small reactance. Thus, (1.4) becomes:

$$\delta P = \frac{V_s \cos \theta}{X} \delta \theta \quad (1.5a)$$

$$\delta Q = \frac{V_s \cos \theta}{X} \delta V \quad (1.5b)$$

It can be seen that as long as the angle is small the approximation is fairly accurate to reflect the strong coupling between active power to angle and reactive power to voltage. Since angle deviations are just the integral of frequency deviations, active power is also coupled to frequency. Thus, typical droop control is implemented as (with i denoting the i -th unit):

$$\omega_i = \omega_i^{set} - k_{pi} P_i \quad (1.6a)$$

$$V_i = V_i^{set} - k_{qi} Q_i \quad (1.6b)$$

where ω_i and V_i are frequency and voltage references, respectively, ω_i^{set} and V_i^{set} are frequency and voltage set-points, respectively, and k_{pi} and k_{qi} are active and reactive power droop gains, respectively. It should be noticed that equations (1.6a) and (1.6b) resemble closely to (1.1). In fact, the negative product terms, $k_p P$ and $k_q Q$, introduce penalty for both voltage and frequency set-points so as to balance the strong competition between sources (which has been illustrated in the DC example).

The equivalent droop charts are shown in Fig. 1-5.

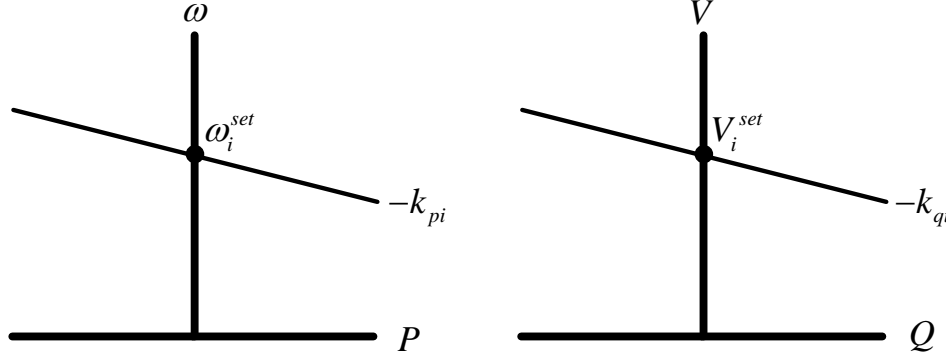


Figure 1-5: AC droop charts.

For active power sharing, frequency is an universal signal so that in steady-state (neglecting frequency reference errors):

$$\omega_{ss} = \omega_1 = \omega_2 = \dots = \omega_i, \quad \forall i \in \{1\dots N\} \quad (1.7)$$

where ω_{ss} is the steady-state frequency and N denotes the total number of participants. Assuming $\omega_1^{set} = \omega_2^{set} = \dots = \omega_N^{set}$, (1.6a) can be used to derive:

$$k_{p1}P_1 = k_{p2}P_2 = k_{pi}P_i, \quad \forall i \in \{1\dots N\} \quad (1.8)$$

(1.8) identifies that active power sharing is inversely proportional to active power droop gains, and the sharing does not depend on the absolute values of droop gains but relative ratios.

Similarly, the same concept can be directly extended to reactive power sharing; however, voltage potential is not an universal signal so that the sharing of reactive power involves with solving network flows, which is more complicated than active power sharing. For the networks with negligible impedance, reactive power sharing, in a rough approximation, can be derived in a similar form:

$$k_{q1}Q_1 = k_{q2}Q_2 = k_{qi}Q_i, \quad \forall i \in \{1\dots N\} \quad (1.9)$$

The above derivation is based on the ideal assumption; however, in practice, the presence of reference errors among devices would essentially violate both (1.8) and (1.9). Particularly, local control units are normally implemented using commercial Microcontrollers (MCUs) or Digital Signal Processors (DSPs). There exists frequency and voltage reference/measurement errors among units. For active power sharing, to quantify such errors, (1.6a) can be modified as:

$$\omega_i + \epsilon_{\omega i} = \omega^{set} - k_{pi}P_i \quad (1.10)$$

where $\epsilon_{\omega i}$ is the error of the i -th unit. Using a two-inverter case as an example, in

steady-state the following equations can be obtained ($\omega_1 = \omega_2$):

$$\omega^{set} - \epsilon_{\omega 1} - k_{p1}P_1 = \omega^{set} - \epsilon_{\omega 2} - k_{p2}P_2 \quad (1.11)$$

By assuming that the droop gains are identical, $k_{p1} = k_{p2} = k_p$, (1.11) becomes:

$$\epsilon_{\omega 2} - \epsilon_{\omega 1} = k_p(P_1 - P_2) \quad (1.12)$$

where it can be seen that droop gains enhance sharing accuracy against tolerance errors. For example, based on the typical MCU frequency tolerance of $\approx 0.05\%$ [29], choosing a limited droop gain at 0.5% will result in 10% sharing inaccuracy among two units. This shows that the absolute values of active power droop gains become important when non-ideal factors are considered (although reactive power sharing suffers less than the tolerance issue due to dominant network impedances). In generally, it is recommended to properly increase both droop gains for better sharing performance (this constraint poses on the lower bound of the droop gains). However, choosing large droop gains, particularly the active power one, might result in system instability. Such an issue will be discussed in the next section.

1.3 Droop Instability

IBMGs suffer from limited active power droop gains due to unique characteristics of microgrids with short lines and near-unity X/R ratios. To investigate the problem, the authors in [13] started to model IBMGs in details and describe system dynamics using a set of ordinary differential equations (ODEs):

$$\frac{d\mathbf{x}}{dt} = f(\mathbf{x}) \quad (1.13)$$

where \mathbf{x} is the vector containing the system states. Since, in general, microgrids are non-linear systems, for studying small-signal stability linearization around system

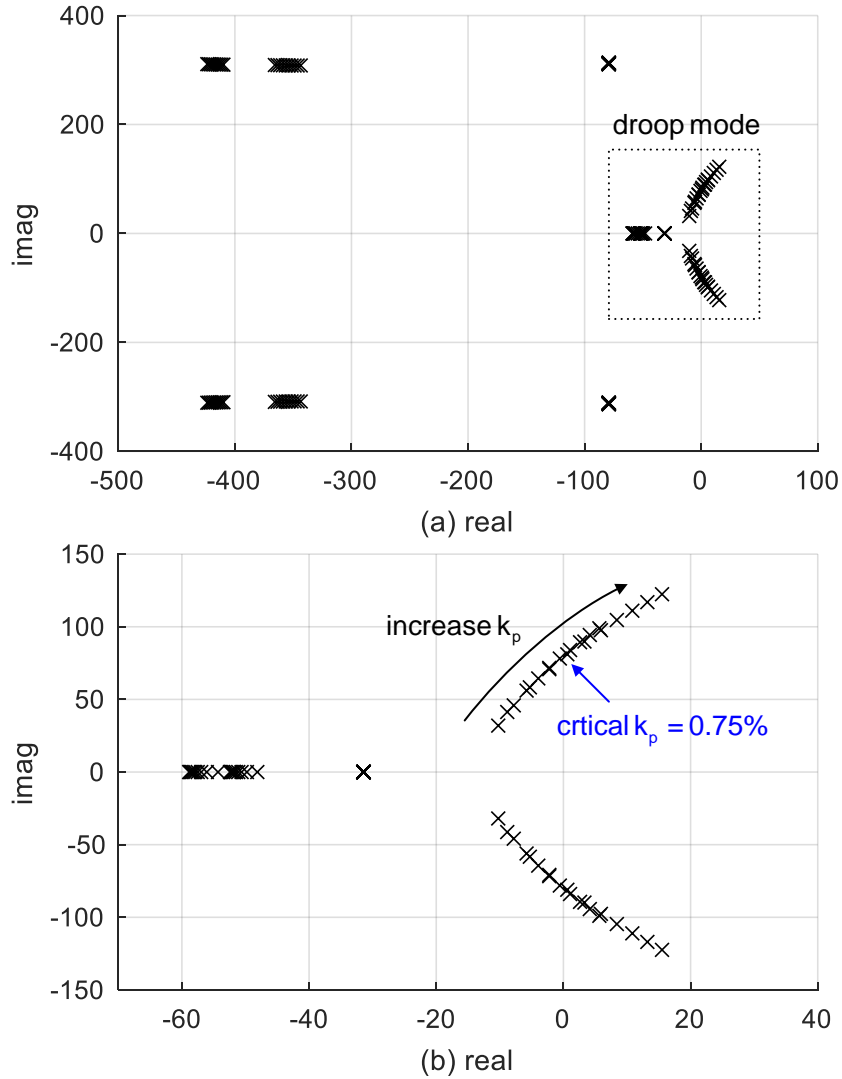


Figure 1-6: Eigenvalue locus of a typical inverter-based microgrid: (a) Zoom-out plot; (b) Zoom-in plot.

equilibrium points was taken to derive the following form:

$$\frac{d\delta \mathbf{x}}{dt} = \mathbf{J}\delta \mathbf{x} \quad (1.14)$$

where $\delta \mathbf{x}$ denote small-signal states and \mathbf{J} is a linearized state transition matrix - *Jacobian Matrix*. Then, the eigenvalues of the derived Jacobian matrix, \mathbf{J} , is computed. If any eigenvalue has positive real part (equivalently, any eigenvalue exists on the right-hand plane of a complex plot), the system is unstable around the equilibrium

point. Such a procedure is normally referred as small-signal stability analysis. It is convenient, then, to perturb certain control parameters to draw the trajectories of eigenvalues - *eigenvalue locus*. Based on the eigenvalue plot, in [13] IBMGs were found to be particularly vulnerable to an increase of the active power droop gain as shown in Figure 1-6(a). In the figure, the eigenvalues with relatively slow dynamics (inside the dashed square) suffer significantly as compared to the fast eigenvalues (the zoom-in plot is shown in Figure 1-6(b)). More specifically, the eigenvalues moving toward the right-hand plane are characterized as droop modes and are directly correlated to droop control. Through the analysis, it can be seen that the active power droop gain, k_p , is significantly constrained to a limited value ($\approx 0.75\%$), affecting the small-signal stability of microgrids.

The above-mentioned eigenvalue analysis based on a detailed model guides a good starting point regarding which parameters lead to instability. However, it gives very little insights into the fundamental of the problem due to its numerical nature for complicated networks. Therefore, in this thesis the problem is intended to be investigated from a different perspective based an an analytical formulation than the commonly-used numerical methods. The proposed approach would greatly benefit the systematic design of microgrid control.

1.4 Contributions

This thesis discloses a physical insight into droop instability and presents a novel control strategy for IBMGs. The investigations into the system would be highly useful for engineers when it comes to the development of microgrid control. Moreover, based on the developed framework, the stability enhancement rules and techniques are proposed in simple and concise forms with high applicability. The key contributions of this thesis are summarized as follows:

1. A reliable and concise reduced-order model for microgrids is investigated in details to uncover the main factors affecting microgrids stability (reported in the author's collaborative paper [21]).

2. Generalization of reduced-order models from a simple two-bus case to arbitrary network settings are discussed and investigated (reported in the author's collaborative paper [21]).
3. Simple and reliable criteria for the sizing of virtual impedance to achieve a desired stability region are derived and analyzed.
4. Plug-and-Play (PnP) compliant control rules for the flexible integration of droop-controlled inverters to form a IBMG are proposed.
5. Comprehensive verification of the proposed approaches based on both simulation and experiment is performed to demonstrate their effectiveness and practicality.

1.5 Thesis Organization

The thesis is organized as follows:

- Chapter 2 begins to investigate the modeling of IBMGs by using a simple two-bus case. The effect of electromagnetic dynamics is illustrated to explain the principal causes of droop instability. It further investigates the generalization of the models to network settings with the consideration of arbitrary network configurations.
- Chapter 3 proposes concise and simple stability criteria for a two-bus case and investigates the generalization procedure for network settings. Based on the Lyapunov stability theorem, quadratic Lyapunov function candidates are developed to certify system stability.
- Chapter 4 analyzes the details of the proposed stability enhancement techniques. The plug-and-play (PnP) compliant control rules are proposed to allow flexible integration of additional inverters. Moreover, the implementation of virtual impedance method is developed to ensure proper internal stability for the control design.

- Chapter 5 investigates on the utilization of communication to achieve secondary compensation. The set-point deviations induced by both droop control and virtual impedance methods can be easily resolved with a simple integral compensator. It further extends the development to allow flexible and accurate power dispatch capabilities for microgrid operations.
- Chapter 6 demonstrates the validation of the proposed approaches through both simulation and experiment. All the detailed parameter are also included.
- Appendix A provides additional derivations and notes.
- Appendix B discloses the details of the simulation models and experimental prototype used for validating the proposed approaches.

Chapter 2

Modeling of Droop-Controlled Inverter-Based Microgrids

2.1 Introduction

A typical configuration of a single droop-controlled inverter contains an external droop (power) controller, which provides references for an inverter internal control system (voltage and current controllers) to regulate the inverter output voltage and frequency. The principle structure of such an inverter connected to a point of common coupling (PCC) is shown in Figure 2-1 [13]. The details of the system are described as:

- Internal Control: The main objective is to regulate inductor filter current and capacitor voltage. Normally, the current control loop is of very high bandwidth based on Pulse-Width-Modulation (PWM) switching techniques. Then the voltage control loop is designed based upon the assumption of instantaneous current regulation.
- Droop/Power Control: First, the measurements of capacitor voltage and output current are taken to compute instantaneous active and reactive power. Low-pass filters (LPFs) are then applied to extract only the low-frequency components of the power measurements so as to remove noise and undesired harmonics. A typical filter bandwidth is around one-tenth of the fundamental frequency of

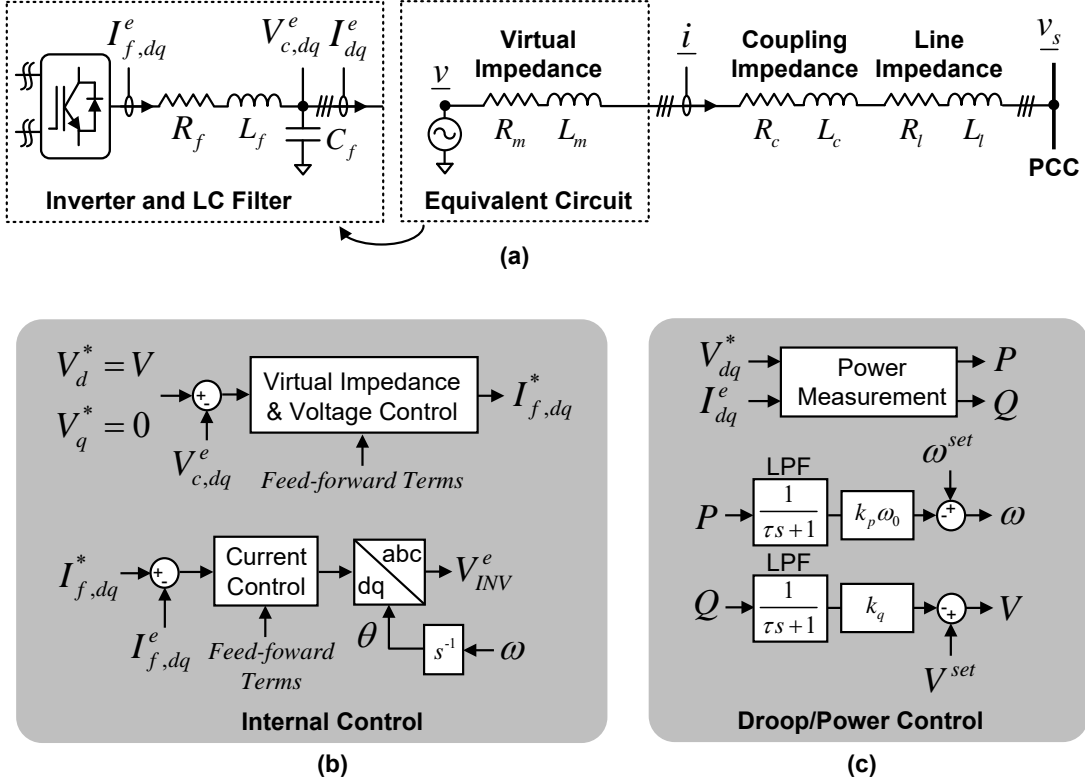


Figure 2-1: (a) Single phase representation of the three-phase inverter system connected to the PCC; (b) Internal control; (c) Droop (Power) Control.

a system. Finally, droop control is applied using the filtered measurements to perform power sharing.

Recently, various modified forms of the internal control have been proposed [12, 23, 26, 30]. Particularly, the emulation of virtual impedance has been shown effective for different purposes including stability enhancement, harmonics sharing, reactive power sharing, etc. Since the dynamics of droop control is much slower as compared to the internal control (due to the slow time constant of the LPFs), for studying power sharing instability it is sufficient to consider the internal control as the equivalent series impedance (R_m, L_m shown in Figure 2-1) connected between the inverter terminal and the internal voltage source. The details of the internal control will be discussed in Chapter 4. For now, this assumption simplifies the investigation on inverters by

considering only droop control, which is of the following form:

$$\omega = \omega^{set} - k_p \omega_0 P_m \quad (2.1a)$$

$$V = V^{set} - k_q Q_m \quad (2.1b)$$

where ω^{set} and V^{set} are the set-points for frequency and voltage, respectively and the values of k_p and k_q are the per-unit frequency and voltage droop gains, respectively (around 0.5% – 3% typically [13]). It should be noticed that this representation is slightly different from the previous chapter as both ω and ω_0 are now measured in rad s^{-1} and θ is in rad with other variables measured in per-unit. As mentioned previously, P_m and Q_m in (2.1) are the active and reactive power filtered by means of passing the measured instantaneous values through LPFs:

$$P_m = \frac{1}{\tau s + 1} P \quad (2.2a)$$

$$Q_m = \frac{1}{\tau s + 1} Q \quad (2.2b)$$

where $\tau = \omega_c^{-1}$ is the filter time constant.

After the simplification is taken, the inverter is now considered to be connected to its terminal through virtual impedance as shown in Figure 2-1 (a) (the representation is a single-phase equivalent circuit for describing the original three-phase system). For studying the network dynamics, dealing with a three-phase system is rather cumbersome; therefore, it is convenient to transform three-phase quantities with respect to a rotating reference frame by using the Park transformation:

$$\begin{bmatrix} U_d \\ U_q \\ U_0 \end{bmatrix} = \frac{2}{3} \begin{bmatrix} \sin(\omega_0 t) & \sin(\omega_0 t - \frac{2}{3}\pi) & \sin(\omega_0 t + \frac{2}{3}\pi) \\ \cos(\omega_0 t) & \cos(\omega_0 t - \frac{2}{3}\pi) & \cos(\omega_0 t + \frac{2}{3}\pi) \\ \frac{1}{2} & \frac{1}{2} & \frac{1}{2} \end{bmatrix} \begin{bmatrix} u_a \\ u_b \\ u_c \end{bmatrix}, \quad (2.3)$$

where $\omega_0 t$ is the angle of an arbitrary rotating reference frame, u_a , u_b , and u_c are the three-phase components, and U_d , U_q , and U_0 are the direct, quadrature, and zero-sequence components, respectively. The inverter under study has only three wires

with no neutral line so that the zero-sequence component becomes zero ($U_0 = 0$). Thus, for convenience, the following notation is used:

$$\underline{u}(t) = (U_d(t) + jU_q(t))e^{j\omega_0 t} = \underline{U}(t)e^{j\omega_0 t} \quad (2.4)$$

where the underline denotes a complex value and all the functions with (t) indicate that they are varying by time. Also, $\underline{u}(t)$ is with respect to stationary reference frames, whereas $\underline{U}(t)$ is with respect to rotating reference frames. The above relationship is further illustrated in Figure 2-2.

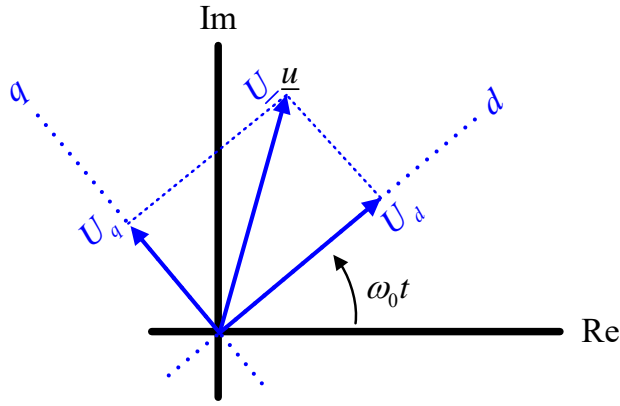


Figure 2-2: Phasor diagram of the relationship between rotating and stationary reference frames.

In stationary reference frames, the current dynamics for the circuit shown in Figure 2-1(a) can be described as:

$$L \frac{di}{dt} = v - \underline{v}_s - R_i \quad (2.5)$$

where (t) is neglected for simplicity and L , R denote the aggregated resistance and inductance of the virtual, coupling, and line impedances ($R = R_m + R_c + R_l$, $L = L_m + L_c + L_l$). Substituting (2.4) into (2.5) for all variables, the following form can be obtained:

$$L \frac{dI}{dt} e^{j\omega_0 t} + j\omega_0 L I e^{j\omega_0 t} = \underline{V} e^{j\omega_0 t} - \underline{V}_s e^{j\omega_0 t} - R I e^{j\omega_0 t} \quad (2.6)$$

It is obvious now that (2.6) can be simplified by multiplying $e^{-j\omega_0 t}$ on both sides (the procedure is privileged by the employment of the Park transformation). In fact, this

leads to the representation of the current dynamics in rotating reference frames:

$$L \frac{d\underline{I}}{dt} + j\omega_0 L \underline{I} = \underline{V} - \underline{V}_s - R \underline{I} \quad (2.7)$$

where by substituting d/dt using the Laplace operator s , the impedance of a typical RL component in nominal frequency ω_0 can be written in the form:

$$\underline{Z}(s) = \frac{\underline{V} - \underline{V}_s}{\underline{I}} = R + jX + sL \quad (2.8)$$

where $X = \omega_0 L$ and $\underline{Z}(0)$ indicates the steady-state impedance. The above notation will be used frequently in this thesis.

Moreover, (2.7) can be equivalently derived by elaborating the complex components:

$$L \frac{d(I_d + jI_q)}{dt} + j\omega_0 L(I_d + jI_q) = (V_d + jV_q) - (V_{sd} + jV_{sq}) - R(I_d + jI_q) \quad (2.9)$$

By separating the real and imaginary parts, the famous dynamic equations of RL circuits in dq reference frames can be obtained:

$$L \frac{dI_d}{dt} = V_d - V_{sd} - RI_d + \omega_0 L I_q \quad (2.10)$$

$$L \frac{dI_q}{dt} = V_q - V_{sq} - RI_q - \omega_0 L I_d \quad (2.11)$$

where all the variables are real in this model; in fact, by choosing a proper rotating reference frame they become constant with respect to time in steady-state so that the design of controller becomes much simpler.

In the later sections the first model developed will idealize the internal control and consider only the droop control and network dynamics, followed by the presentation of different reduced-order models with an explicit demonstration of the failure based on a quasi-stationary approximation. Finally, the generalization to the network cases will be investigated in order to consider practical microgrid settings. The models presented in the following sections are also reported in the author's collaborative

paper [21]¹.

2.2 5th-order Electromagnetic Model

As shown in Figure 2-1(a), the inverter with its *LC* filter is considered as an effective voltage source connected to the terminal through virtual impedance. Based on the simplified circuit, a set of Ordinary Differential Equations (ODEs) can be derived. First, the droop control and the power filters described in equations (2.1) and equations (2.2) can form:

$$\omega = \omega^{set} - \frac{k_p\omega_0}{\tau s + 1}P \quad (2.12)$$

$$V = V^{set} - \frac{k_q}{\tau s + 1}Q \quad (2.13)$$

Multiplying both sides by $\tau s + 1$ and replacing s by d/dt , the above equations become:

$$\tau \frac{d\omega}{dt} = \omega^{set} - \omega - k_p\omega_0 P \quad (2.14)$$

$$\tau \frac{dV}{dt} = V^{set} - V - k_q Q \quad (2.15)$$

where ω^{set} and V^{set} are assumed constant by time. For the network dynamics, equations (2.10) and (2.11) can be applied by considering that the *d*-axis of the rotating reference frame is aligned with the stiff voltage source at the PCC. This implies that the stiff voltage source is of the form, $\underline{V}_s = V_s + j0$, whereas the internal voltage source becomes $\underline{V} = V \cos \theta + jV \sin \theta$ with θ denoting the angle with respect to the stiff voltage source. Therefore, a 5th-order electromagnetic (EM) model in the *dq* reference frame is initiated:

¹Great appreciation to Prof. Petr Vorobev (first author), Prof. Mohamed Al Hosani, Prof. James Kirtley, and Prof. Konstantin Turitsyn for their contributions and efforts.

$$\frac{d\theta}{dt} = \omega - \omega_0 \quad (2.16)$$

$$\tau \frac{d\omega}{dt} = \omega^{set} - \omega - k_p \omega_0 P \quad (2.17)$$

$$\tau \frac{dV}{dt} = V^{set} - V - k_q Q \quad (2.18)$$

$$L \frac{dI_d}{dt} = V \cos \theta - V_s - RI_d + \omega_0 L I_q \quad (2.19)$$

$$L \frac{dI_q}{dt} = V \sin \theta - RI_q - \omega_0 L I_d \quad (2.20)$$

where

$$P = V \cos \theta I_d + V \sin \theta I_q \quad (2.21)$$

$$Q = V \sin \theta I_d - V \cos \theta I_q. \quad (2.22)$$

where (2.16) tracks the relative angle of the internal voltage source, equations (2.17) and (2.18) represent the dynamics of the terminal voltage and frequency by incorporating the low-pass filters of the inverter power control system characterized by the bandwidth $w_c = \tau^{-1}$, and equations (2.19) and (2.20) model the electromagnetic dynamics of the complex current $\underline{I} = I_d + jI_q$. The values $L = L_m + L_c + L_l$ and $R = R_m + R_c + R_l$ are the aggregate inductance and resistance of the virtual, coupling, and line impedances. This model can be validated by directly running simulation versus the detailed inverter average model containing all the inverter internal states. The justification for such an assumption will be validated in the later chapter.

For the described system, the time constant of a short line (assuming the line is 1 km long based on the parameters shown in Table 6.1) is $L/R \approx 3.1ms$, whereas the filter time constant is $\tau \approx 31.8ms$ (droop dynamics). Thus, this obvious time-scale separation encourages further model order reduction by assuming that the line current equilibrates much faster than the slow droop states. This procedure is equivalent to neglecting the derivative terms on the left-hand side of (2.19) and (2.20). Although such an approximation is generally accepted for small-signal stability anal-

ysis in conventional power systems, the following discussion will address on the failures of applying such an assumption for microgrids.

2.3 Model Order Reduction

2.3.1 3rd-order Conventional Model

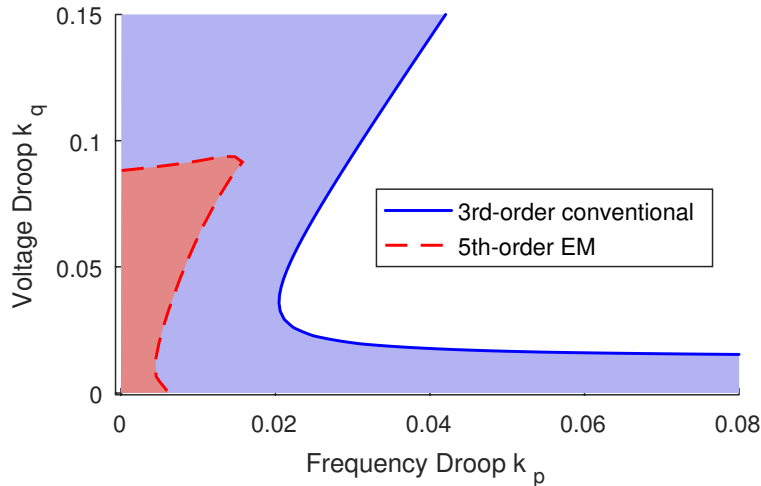


Figure 2-3: Comparison of stability regions predicted by the 5th-order EM and 3rd-order conventional models: $X = 0.42\%$, $R = 0.28\%$, and $\tau = 0.0318$.

The quasi-stationary approximation (0th-order approximation) is first investigated to demonstrate the reduction procedure. By neglecting the effect of current dynamics, equivalently setting the derivative terms in the left-hand side of (2.19) and (2.20) to zero, the line current can be expressed as:

$$\underline{I}^0 = \frac{V e^{j\theta} - V_s}{R + j\omega_0 L} \quad (2.23)$$

where ω_0 denotes the steady-state frequency, and the superscript ⁰ indicates the result under 0th-order order approximation. (2.23) can further lead to the expression of the

active and reactive power:

$$P^0 = \text{Re}\{Ve^{j\theta}\underline{I}^0\} = B \sin \theta + G(V/V_s - \cos \theta) \quad (2.24)$$

$$Q^0 = \text{Im}\{Ve^{j\theta}\underline{I}^0\} = B(V/V_s - \cos \theta) - G \sin \theta \quad (2.25)$$

where \underline{I}^0 denotes the complex conjugate of \underline{I}^0 , $B = VV_s\omega_0 L/(R^2 + \omega_0^2 L^2)$, and $G = VV_s R/(R^2 + \omega_0^2 L^2)$. Substitution of equations (2.24) and (2.25) into equations (2.16)-(2.18) along with linearization can generate:

$$\tau \lambda_p \ddot{\delta\theta} + \lambda_p \dot{\delta\theta} + \frac{\partial P^0}{\partial \theta} \delta\theta + \frac{\partial P^0}{\partial V} \delta V = 0 \quad (2.26a)$$

$$\tau \lambda_q \dot{\delta V} + \lambda_q \delta V + \frac{\partial Q^0}{\partial \theta} \delta\theta + \frac{\partial Q^0}{\partial V} \delta V = 0 \quad (2.26b)$$

where $\lambda_p = (\omega_0 k_p)^{-1}$, $\lambda_q = (k_q)^{-1}$, $\tau = w_c^{-1}$, $\omega_0 = 100\pi$, and $\delta\theta$ as well as δV are the small-signal deviations of the angle and voltage, respectively. Assuming the system is operating in nominal conditions [20, 31] ($\theta \approx 0$ and $V \approx V_s = 1 \text{ pu}$), the system in (2.26) reduces to a concise form:

$$\tau \lambda_p \ddot{\vartheta} + \lambda_p \dot{\vartheta} + B\vartheta + G\rho = 0 \quad (2.27a)$$

$$\tau \lambda_q \dot{\rho} + (\lambda_q + B)\rho - G\vartheta = 0 \quad (2.27b)$$

where $\vartheta \triangleq \delta\theta$, $\rho \triangleq \delta V$, and the expressions for B and G are simplified to:

$$B = \frac{X}{R^2 + X^2}, \quad G = \frac{R}{R^2 + X^2} \quad (2.28)$$

with $X = \omega_0 L$. It should be noted that ρ , B , and G are all dimensionless in this expression and ϑ is in rad. This linear model serves as the first reduced-order model to describe the droop-controlled inverter shown in Figure 2-1. To validate its effectiveness, one may perform time-domain analysis against the 5th-order EM model and compare the dynamic responses between two models. A more comprehensive method is to plot the small-signal stability region with respect to control parameters (droop gains) predicted by the two models. For the 3rd-order model, the Jacobian matrix is implic-

itly given so it is rather obvious to compute the eigenvalues, while for the 5th-order EM model (non-linear), the procedure described in Chapter 1.3 is needed to identify whether the system is stable given a pair of droop gains (details of the procedure are also shown in the appendixes). In general, this method requires to sample parameter space to draw stability boundaries. An example is shown in Figure 2-3, where two corresponding stability regions are plotted together with respect to the droop gains, k_p and k_q . It can be seen that the prediction from the 3rd-order model in (2.27) is quite inaccurate as compared to the EM model. The 3rd-order model is, in fact, too optimistic and any pair of droop gains outside the region predicted by the EM model is actually unstable. Adopting this approximation may jeopardize the control design and result in system failures. Thus, a remedy is needed and will be discussed in the next subsection.

2.3.2 3rd-order High-Fidelity Model

The inappropriate assumption of employing quasi-stationary approximation has been shown in the previous subsection. The main reason behind the failure is due to missing the participation of electromagnetic modes. In fact, electromagnetic transients play a critical role in droop instability despite their short timescale [20, 31]. Equivalently, these electromagnetic transients have influences on the derivative terms of the left-hand side of equations (2.19) and (2.20) which cannot be fully ignored [21]. In fact, it is possible to account for these transients while performing the model order reduction. The procedure necessarily leads to a more accurate model, which is referred as a *3rd-order high-fidelity model*. Now the Laplace operator s is considered such that the current representation becomes:

$$\underline{I} = \frac{V e^{j\theta} - V_s}{R + j\omega_0 L + sL} = \frac{\underline{I}^0}{1 + sL/(R + j\omega_0 L)}. \quad (2.29)$$

By using the Taylor series expansion on the Laplace operator s , (2.29) can be expressed as:

$$\underline{I} \approx \underline{I}^0 - \frac{Ls}{R + j\omega_0 L} \underline{I}^0. \quad (2.30)$$

where the high-order terms (greater than one) are truncated and \underline{I}^0 is given in (2.23).

Returning back to the time domain, (2.30) can be rewritten as

$$\underline{I} \approx \underline{I}^0 - \frac{L}{R + j\omega_0 L} \frac{d\underline{I}^0}{dt} \quad (2.31)$$

Then, the approximate values of P and Q are obtained as follows:

$$P \approx P^0 - G' \delta \dot{V} - B' \dot{\delta \theta} \quad (2.32)$$

$$Q \approx Q^0 - B' \delta \dot{V} + G' \dot{\delta \theta}, \quad (2.33)$$

where G' and B' are given by

$$B' = \frac{2LRX}{(R^2 + X^2)^2}, \quad G' = \frac{L(R^2 - X^2)}{(R^2 + X^2)^2}. \quad (2.34)$$

It can be seen that the active and reactive power flows now depend not only on the voltage magnitude and angle, but also on their rates of change. Although G' and B' are small as compared to the zeroth order terms, they influence significantly on the droop stability of IBMGs.

Substituting equations (2.32) and (2.33) into equations (2.16)-(2.18), the dynamical equations for angular and voltage now become:

$$\tau \lambda_p \ddot{\vartheta} + (\lambda_p - B') \dot{\vartheta} + B\vartheta + G\rho - G'\dot{\rho} = 0 \quad (2.35a)$$

$$(\tau \lambda_q - B') \dot{\rho} + (\lambda_q + B)\rho - G\vartheta + G'\dot{\vartheta} = 0 \quad (2.35b)$$

Based on the above equations, two simple stability estimates can be observed:

- (1) The coefficient of the first-order term for the angle in (2.35a), $\lambda_p - B'$, should be positive; (2) The coefficient of the first-order term for the voltage in (2.35b), $\tau \lambda_q - B'$, should also be positive. The first condition is based on the second-order angle oscillator in (2.35a), $\tau \lambda_p \ddot{\vartheta} + (\lambda_p - B') \dot{\vartheta} + B\vartheta$, whereas the second condition is derived by assuming that the first-order system of voltage in (2.35b) have only

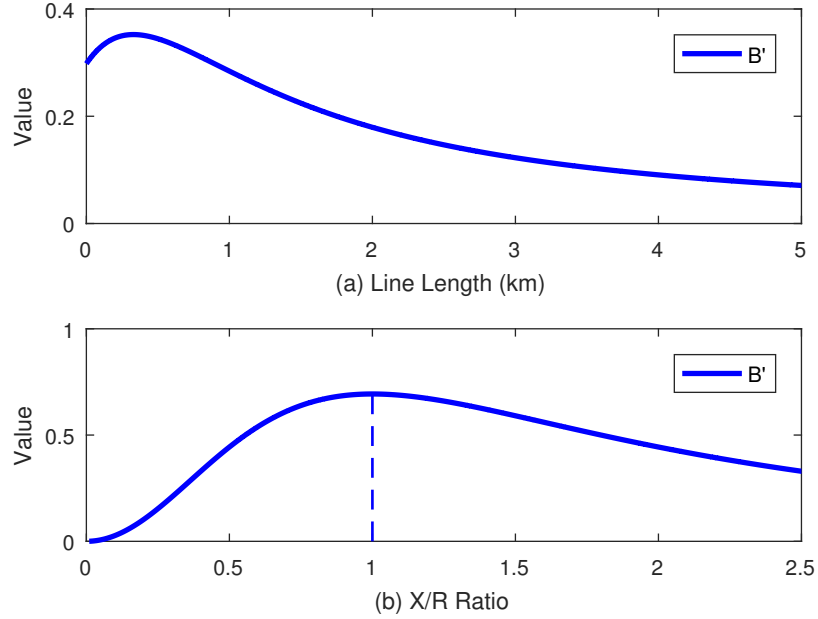


Figure 2-4: Variation of B' with respect to: (a) Line length (km); (b) X/R ratio.

positive coefficients. Therefore, the following conditions can then be further derived:

$$0 < k_p < \frac{1}{\omega_0 B'}, \quad 0 < k_q < \frac{\tau}{B'}, \quad (2.36)$$

where it becomes clear that B' has influence on the upper limits of both k_p and k_q . It should be emphasize that the droop gains are constrained to be positive, so the later stability conditions in this thesis will not explicitly show the positiveness requirement. In fact, B' capture the electromagnetic participation on the droop mode - referred as *transient susceptance* in [21]. By using the expression in (2.34), it is possible to analyze the effect of network on the value of B' . Considering the equivalent circuit in Figure 2-1(a), the variation of B' with respect to the line length ($X_l/R_l = 0.5$ is assumed) is shown in Figure 2-4(a). Moreover, in Figure 2-4(b), the value of B' is plotted by varying the overall X/R ratio of the total impedance. It can be seen that B' has greater values whenever: (1) The line is short; (2) The overall X/R is around unity. In fact, these two properties are exactly the reason why small-scale microgrids suffer from the droop instability since lines are short and relatively resistive.

It is important to emphasize that the relations in (2.36) do not represent the

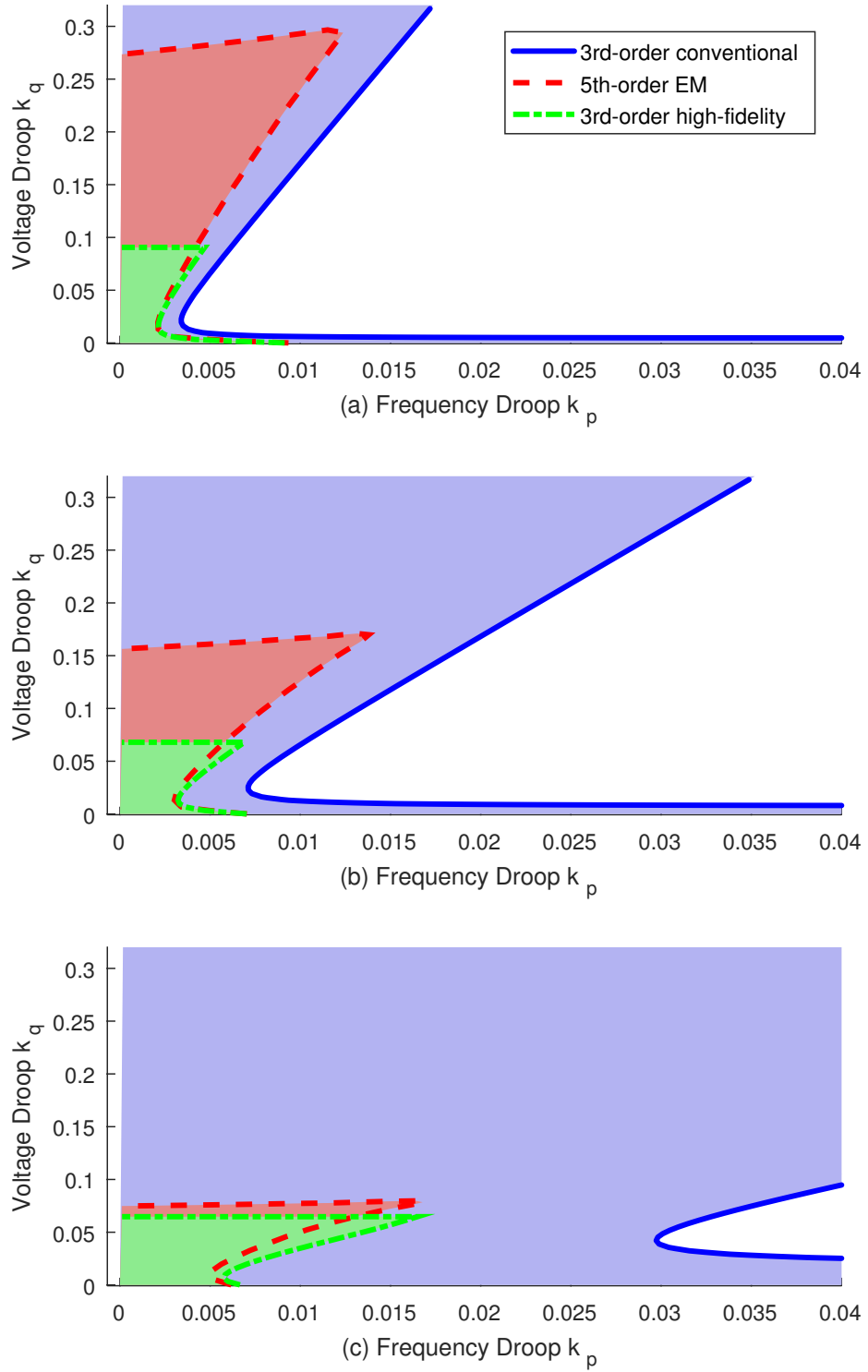


Figure 2-5: Comparison of stability regions predicted by different models: $Z = 0.5\%$; (a) $X/R = 0.7$; (b) $X/R = 1.0$; (c) $X/R = 1.7$.

exact stability criteria but rather a general estimation of the small-signal stability boundary. Rigorous stability certificates will be derived in the later chapter. In fact,

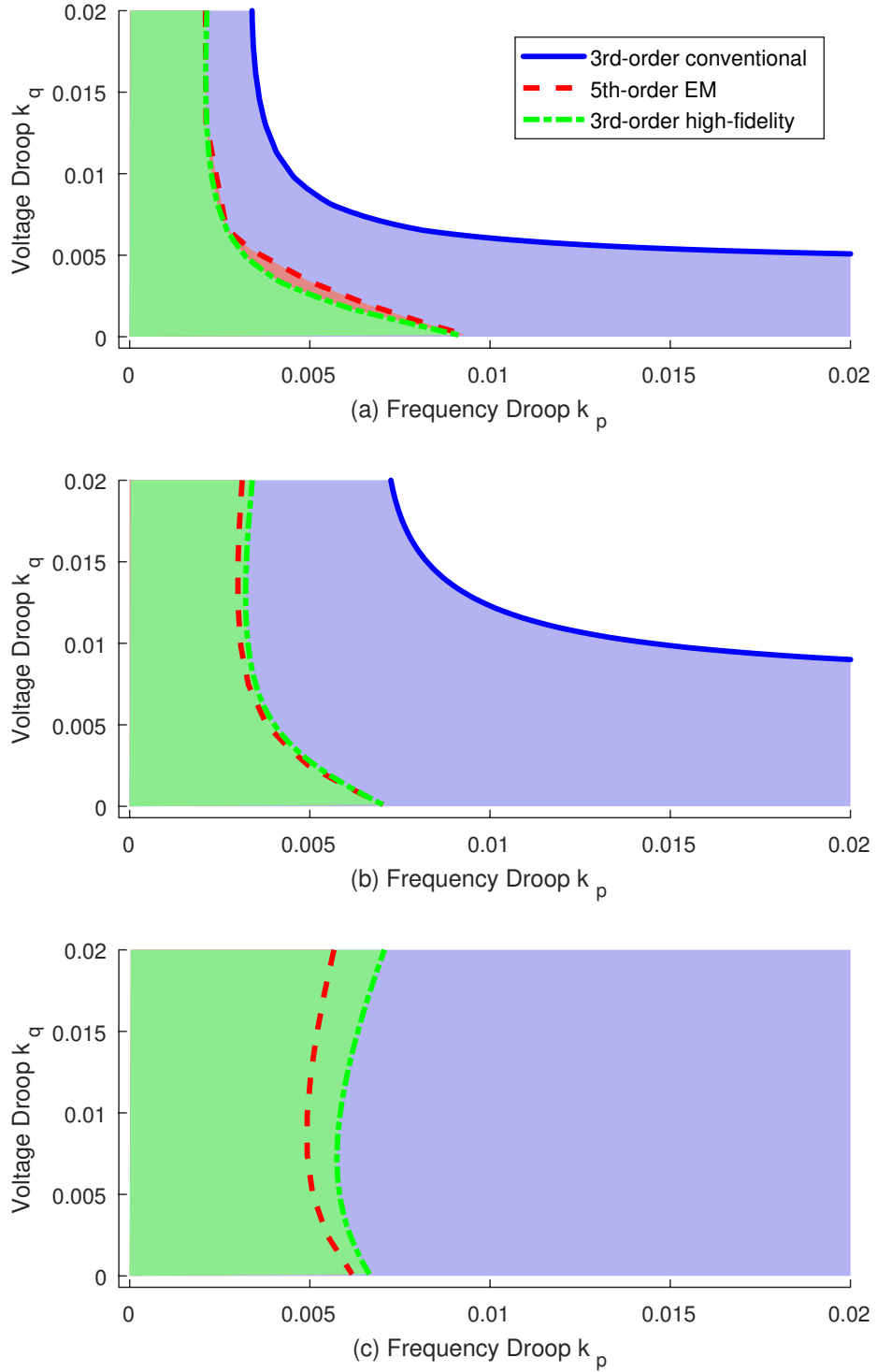


Figure 2-6: Zoom-in comparison of stability regions predicted by different models: $Z = 0.5\%$; (a) $X/R = 0.7$; (b) $X/R = 1.0$; (c) $X/R = 1.7$.

these general stability properties have no analogy for large-scale power systems since short transmission lines often indicate a positive influence of system stability [32],

which is opposite to what has been revealed for microgrids.

For further validation, the comparisons of three different models (the 5th-order EM model presented in (2.16)–(2.20), the 3rd-order conventional model and the 3rd-order high-fidelity model) based on different X/R ratios are presented in Figure 2-5, where the prediction of the high-fidelity 3rd-order model demonstrates some conservativeness for k_q while that of the conventional model is completely inaccurate. In general, the prediction for k_q improves when X/R ratios are higher. The comparisons in Figure 2-5 are not very effective since the scales of k_p and k_q are quite different. For practical droop control systems, the droop gains are around 1 – 3%; therefore, the zoom-in plots of the stability regions are shown in Figure 2-6 for further validation. Overall, the high-fidelity model outperforms the conventional model in all cases and will be later used to develop systematic control strategies.

2.4 Network Generalization

In the section, a generalization approach will be discussed to extend the framework for modeling multiple inverters and loads. First, considering that all the inverters follow the same structure of the droop control in equations (2.17) and (2.18) and the loads are linear, the generalization of the model presented in Section 2.3.2 to networks is done directly by constructing dynamic equations similar to (2.35) for every inverter node. Thus, following the standard stamping procedure, a network admittance matrix $\underline{\mathbf{Y}}^U(s)$ (with the Laplace operator s) is constructed using network parameters with all the line and load impedances $\underline{Z}_{ij}(s)$ written in the Laplace domain (i.e., $\underline{Z}_{ij} = R_{ij} + j\omega_0 L_{ij} + sL_{ij}$). Since network configurations can be arbitrary, the obtained network admittance matrix $\underline{\mathbf{Y}}^U(s)$ may contain some virtual nodes to which there are no inverters connected. This means that the system can be described in the following form:

$$\begin{bmatrix} \underline{\mathbf{I}}_{inv}(s) \\ \mathbf{0} \end{bmatrix} = \begin{bmatrix} \underline{\mathbf{Y}}_{11}^U(s) & \underline{\mathbf{Y}}_{12}^U(s) \\ \underline{\mathbf{Y}}_{21}^U(s) & \underline{\mathbf{Y}}_{22}^U(s) \end{bmatrix} \begin{bmatrix} \underline{\mathbf{V}}_{inv}(s) \\ \underline{\mathbf{V}}_v(s) \end{bmatrix}. \quad (2.37)$$

where $\underline{\mathbf{I}}_{inv}(s)$ denotes the complex vector of the current into the inverter nodes, $\underline{\mathbf{V}}_{inv}(s)$ represents the complex voltage at the inverter nodes, and $\underline{\mathbf{V}}_v(s)$ is the complex voltage at the virtual nodes. Thus, the Kron reduction method can be applied to eliminate the virtual nodes:

$$\underline{\mathbf{I}}_{inv}(s) = \underline{\mathbf{Y}}(s)\underline{\mathbf{V}}_{inv}(s) \quad (2.38)$$

where $\underline{\mathbf{Y}}(s)$ is the $N \times N$ Kron-reduced admittance matrix:

$$\underline{\mathbf{Y}}(s) = \underline{\mathbf{Y}}_{11}^U(s) - \underline{\mathbf{Y}}_{12}^U(s) (\underline{\mathbf{Y}}_{22}^U(s))^{-1} \underline{\mathbf{Y}}_{21}^U(s) \quad (2.39)$$

Then, the next step is to expand the admittance matrix using the Taylor series expansion on the Laplace operator s :

$$\underline{\mathbf{Y}}(s) \approx \underline{\mathbf{Y}}^0 + \underline{\mathbf{Y}}^1 s \quad (2.40)$$

where

$$\underline{\mathbf{Y}}^0 = \underline{\mathbf{Y}}(0) \quad (2.41a)$$

$$\underline{\mathbf{Y}}^1 = \frac{\partial \underline{\mathbf{Y}}(s)}{\partial s} \Big|_{s=0} \quad (2.41b)$$

Since the matrix $\underline{\mathbf{Y}}(s)$ links inverter voltages to inverter currents, it is convenient to separate the admittance matrix into the *network* (denoted by the subscript N) and the *load* (denoted by the subscript L) parts:

$$\underline{\mathbf{Y}}(s) = \underline{\mathbf{Y}}_N(s) + \underline{\mathbf{Y}}_L(s) \quad (2.42)$$

where $\underline{\mathbf{Y}}_L(s)$ is a diagonal matrix and the elements in $\underline{\mathbf{Y}}_N(s)$ follow:

$$\sum_{j=1}^N Y_{N,ij} = 0, \quad \forall i \in \{1, \dots, N\} \quad (2.43)$$

In fact, the separation procedure can be done by subtracting the absolute sum of off-diagonal elements from the diagonal element for every row. This applies to the matrix after the approximation such that (2.38) can be now approximated as:

$$\underline{\mathbf{I}}_{inv}(s) = [\underline{\mathbf{Y}}_N^0 + \underline{\mathbf{Y}}_L^0] \underline{\mathbf{V}}_{inv}(s) + [\underline{\mathbf{Y}}_N^1 + \underline{\mathbf{Y}}_L^1] s \underline{\mathbf{V}}_{inv}(s) \quad (2.44)$$

After switching back to time domain, a time-domain version of (2.31) is obtained:

$$\underline{\mathbf{I}}_{inv}(s) = [\underline{\mathbf{Y}}_N^0 + \underline{\mathbf{Y}}_L^0] \underline{\mathbf{V}}_{inv}(s) + [\underline{\mathbf{Y}}_N^1 + \underline{\mathbf{Y}}_L^1] \dot{\underline{\mathbf{V}}}_{inv}(s) \quad (2.45)$$

Then, the (2.45) can be used to construct the generalized dynamic equations of a network with multiple inverters and loads (similar to (2.35)):

$$\tau \Lambda_p \ddot{\vartheta} + (\Lambda_p - \mathbf{B}') \dot{\vartheta} + \mathbf{B} \vartheta + (\mathbf{G} + \tilde{\mathbf{G}}) \boldsymbol{\varrho} - \mathbf{G}' \dot{\boldsymbol{\varrho}} = 0 \quad (2.46a)$$

$$(\tau \Lambda_q - \mathbf{B}') \dot{\boldsymbol{\varrho}} + (\Lambda_q + \mathbf{B} + \tilde{\mathbf{B}}) \boldsymbol{\varrho} - \mathbf{G} \vartheta + \mathbf{G}' \dot{\vartheta} = 0 \quad (2.46b)$$

where ϑ , $\boldsymbol{\varrho}$ are the vectors of inverter angles and (relative) voltages, respectively; and \mathbf{B} , $\tilde{\mathbf{B}}$, \mathbf{G} , $\tilde{\mathbf{G}}$, \mathbf{B}' , and \mathbf{G}' are square matrices with dimensions corresponding to the number of inverters in the grid; Λ_p and Λ_q represent the diagonal matrices with elements equal to the inverse of frequency and voltage droop coefficients:

$$\Lambda_p = \text{diag}([\lambda_{p,1}, \lambda_{p,i}, \dots, \lambda_{p,N}]), \quad \Lambda_q = \text{diag}([\lambda_{q,1}, \lambda_{q,i}, \dots, \lambda_{q,N}]) \quad (2.47)$$

where $\lambda_{p,i} = (\omega_0 k_{p,i})^{-1}$ and $\lambda_{q,i} = k_{q,i}^{-1}$. Matrices \mathbf{B} , $\tilde{\mathbf{B}}$, \mathbf{G} and $\tilde{\mathbf{G}}$ can be expressed in terms of network admittance matrix:

$$\mathbf{B} = -\text{Im}\{\underline{\mathbf{Y}}_N^0\}, \quad \mathbf{G} = \text{Re}\{\underline{\mathbf{Y}}_N^0\} \quad (2.48)$$

$$\tilde{\mathbf{B}} = -2\text{Im}\{\underline{\mathbf{Y}}_L^0\}, \quad \tilde{\mathbf{G}} = 2\text{Re}\{\underline{\mathbf{Y}}_L^0\} \quad (2.49)$$

For typical networks, it is important to note that both \mathbf{B} and \mathbf{G} are singular, while $\tilde{\mathbf{B}}$ and $\tilde{\mathbf{G}}$ are diagonal matrices. Matrices \mathbf{B}' and \mathbf{G}' represent the effect of network

and load dynamics, and can be expressed as:

$$\mathbf{B}' = \text{Im} \left\{ \underline{\mathbf{Y}}_N^{-1} + \underline{\mathbf{Y}}_L^{-1} \right\} \quad (2.50a)$$

$$\mathbf{G}' = -\text{Re} \left\{ \underline{\mathbf{Y}}_N^{-1} + \underline{\mathbf{Y}}_L^{-1} \right\} \quad (2.50b)$$

In fact, this procedure can be also extended to the networks with different types of loads and sources such as constant power loads (CPL) and current-controlled inverters, which should be simply treated as constant power sources (CPS). For small-signal stability studies, it is sufficient to treat them as linearized equivalent impedances by considering the dynamic responses around the time scale of interest. For the current-controlled inverters with active participation into voltage and frequency regulation, one may need to consider modeling them as inverter nodes. Typically, the equivalent impedances of loads are much larger than the impedances of lines, so one would expect their effect to be negligible. That is, load participation is, in general, negligible for small-scale IBMGs [33, 34]. Therefore, equations in (2.46) can be reduced to:

$$\tau \Lambda_p \ddot{\vartheta} + (\Lambda_p - \mathbf{B}') \dot{\vartheta} + \mathbf{B} \vartheta + \mathbf{G} \varrho - \mathbf{G}' \dot{\varrho} = 0 \quad (2.51a)$$

$$(\tau \Lambda_q - \mathbf{B}') \dot{\varrho} + (\Lambda_q + \mathbf{B}) \varrho - \mathbf{G} \vartheta + \mathbf{G}' \dot{\vartheta} = 0 \quad (2.51b)$$

Equations (2.51) allow one to analyze the stability of a multi-inverter system based on an effective low-order form (three states for each inverter). Therefore, this model gives an important contribution for preserving the commonly-used oscillator-type framework while achieving high-fidelity through capturing the network dynamics. This significantly facilitates the development of advanced stability assessment for inverter-based microgrids [16, 17, 35].

2.5 Model Accuracy and Efficiency

To verify the accuracy of the high-fidelity reduced-order model, a system with five inverters in the cascade configuration shown in Figure 2-7 will be investigated. The

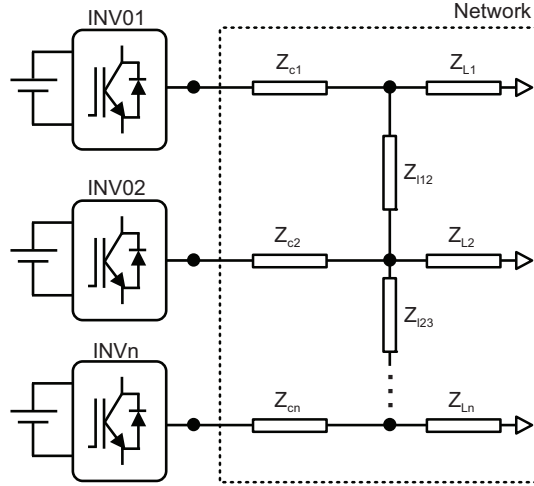


Figure 2-7: System configuration of inverter-based microgrid under study.

system parameters of five inverter-based microgrid are given in Table 2.1. First, a time-domain simulation was conducted to compare the dynamic responses (with adjusted initial conditions) predicted by different models for different values of droop coefficients, as shown in Figure 2-8. It is shown that all the models match very well when the operating droop gains are far away from the instability boundary as shown in Figure 2-8(a). The discrepancies between the models become significant when the system reaches instability as shown in Figure 2-8(b), where erroneous prediction can be observed from the 3rd-order conventional model, while the high-fidelity model gives an accurate prediction. It should be emphasized that the effectiveness of reduced-order models in time-domain simulation can not be validated when the parameters are far way from critical conditions. Furthermore, the comparison of eigenvalue movements by varying k_p for different models is given in Figure 2-9. It can be seen that the eigenvalues of the system calculated using the high-fidelity model are much closer to the EM model as compared to the conventional model, which is consistent with the simplified two-bus results presented in section 2.3.2.

Another important feature of the proposed reduced-order model is that it mitigates the computation burden on dynamic simulation (although the solution is a zero vector for the reduced-order models and initial offsets need to be added). For the EM model, all the line and load states are considered. The total number of states (N_s) is

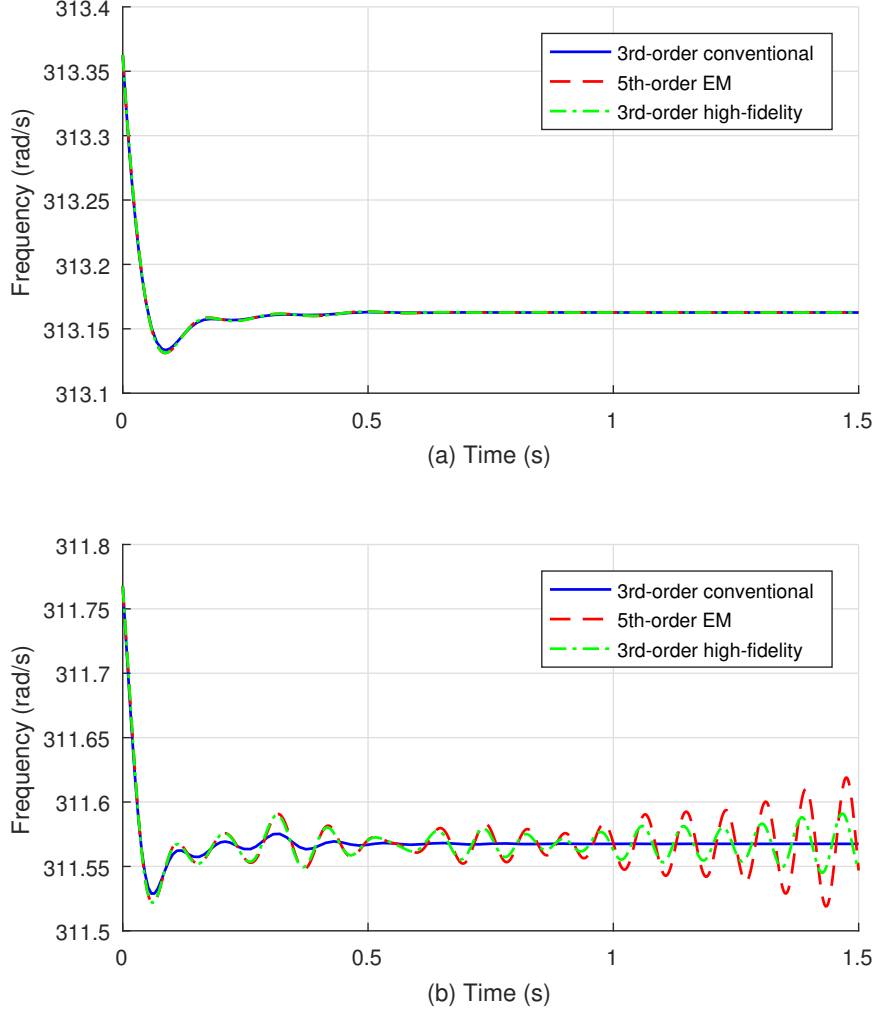


Figure 2-8: Dynamic responses (with adjusted initial conditions) of different models with different droop gains. (a) $k_p = 0.5\%$, $k_q = 3\%$. (b) $k_p = 1.3\%$, $k_q = 3\%$.

approximately 9 times the number of inverters in the cascade topology. In comparison, the proposed technique requires only 3 states per inverter, which reduces the number of states by two-thirds. This allows to handle a network system with a large number of inverters. To identify the efficiency of the proposed model, the EM and 3^{rd} -order high-fidelity models are tested via time-domain simulation by using MATLAB default ODE solvers. The inverters, coupling inductors, and the lines are assumed to be identical for simplicity. The simulation time is set to be 1 second. The results are shown in Table 2.2 for 5 and 25 inverter microgrids. These results clearly demonstrate that the proposed model reduces the number of states and improves the simulation efficiency significantly.

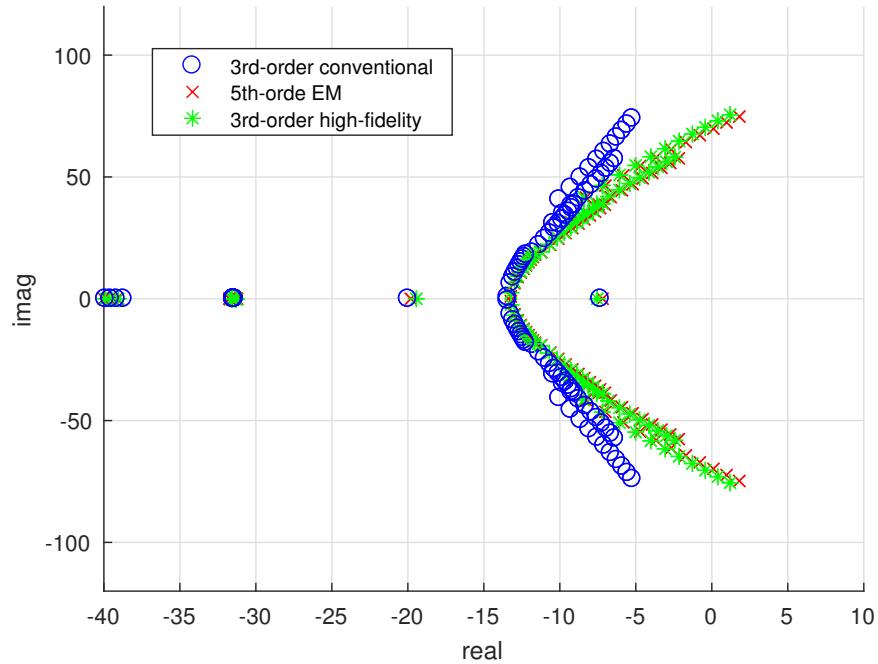


Figure 2-9: Eigenvalue plots of different models ($k_p = 0.35\% - 1.23\%$).

Table 2.1: Parameters of Five Inverter-Based Microgrid

Parameter	Description	Value
V_b	Base Voltage	381.58 V
S_b	Base Power	10 kVA
ω_0	Nominal Frequency	$2\pi \times 50$ rad/s
L_c	Coupling Inductance	0.35 mH
R_c	Coupling Resistance	30 mΩ
w_c	Filter Constant	31.4 rad/s
L_l	Line Inductance	0.26 mH km^{-1}
R_l	Line Resistance	$165 \text{ m}\Omega \text{ km}^{-1}$
l_{ij}	Line Length	[5, 4.1, 3, 6] km
Z_1	Bus 1 Load	25 Ω
Z_2	Bus 2 Load	20 Ω
Z_3	Bus 3 Load	$20 + 4.72i$ Ω
Z_4	Bus 4 Load	$40 + 12.58i$ Ω
Z_5	Bus 5 Load	$18.4 + 0.157i$ Ω
X/R	Average X/R Ratio	0.6224

2.6 Conclusions

Fast network dynamics of microgrids can significantly affect slow droop control as contrary to large-scale power systems. Particularly, the stability region with respect to

Table 2.2: Computational Time Comparison

	n = 5		n = 25	
	EM	Proposed	EM	Proposed
N_s	42	15	222	75
ode23	NA	0.118s	NA	0.119s
ode23s	17.36s	0.367s	>20s	1.727s
ode23t	0.345s	0.067s	0.926s	0.08s
ode23tb	0.384s	0.073s	1.14s	0.097s

the frequency droop gain is significantly constrained. In this chapter, an insight into the physical mechanism of instability was first presented based on a two-bus example along with a method for proper approximation of fast network modes without compromising the accuracy of the model. The failure of adopting conventional reduced-order models through the quasi-stationary approximation was clearly demonstrated. More specifically, the high-fidelity model introduces the new terms, G' and B' , that characterize the electromagnetic participation on the droop mode. The investigation indicated that the stability region is diminished by short lines and near-unity X/R ratios, which are the main properties of small-scale microgrids. The technique was then generalized to network settings with multiple inverters and arbitrary network configurations, followed by the dynamic equations derived based on inverter state variables. Finally, the high-fidelity model was validated through both time-domain simulation and eigenvalue analysis. The results showed that the high-fidelity model can achieve satisfactory balance between accuracy and computation complexity.

Chapter 3

Stability Assessment

3.1 Introduction

Although conducting eigenvalue extractions from a detailed model, in general, is not a computational burden for a small-scale microgrid system, its numerical outcomes provide very limited information for understanding the system dynamics. Moreover, there exists the separation of the participation of states into system modes, which have been reported in [13]. This leads to a more straight-forward representation of equations using the reduced-order model of high accuracy presented in the previous chapter. First, without loss of generality to a network setting, similar to Section 2 where the problem was first formulated using a simple two-bus system, this chapter starts by constructing Lyapunov function candidates for the simple case to identify the important parameters that affect system stability. Based on the derived criteria, the extension to the network case will be later discussed and investigated.

3.2 Two-Bus Example

Considering now a simple two-bus case as described in (2.35), a method of Lyapunov functions is especially convenient - by finding a positive Lyapunov function $\mathcal{V}(\mathbf{x}) > 0$ for $\mathbf{x} \neq \mathbf{0}$ (\mathbf{x} is a vector of system states), the system stability can be certified if the time-derivative of this function is negative, i.e. $\dot{\mathcal{V}}(\mathbf{x}) < 0$ for $\mathbf{x} \neq \mathbf{0}$ [36]. Although ob-

taining effective candidate functions for arbitrary systems is usually a non-trivial task, for linear systems, quadratic Lyapunov function candidates can produce reasonable results. Multiplying (2.35a) by $(c\tau\dot{\vartheta} + \vartheta)$ (c is some constant), one can obtain:

$$\begin{aligned} & \frac{d}{dt} \left\{ \frac{\lambda_p(\tau\dot{\vartheta} + \vartheta)^2}{2} + \frac{(c\tau B - B')\vartheta^2}{2} + \frac{(c-1)\tau^2\lambda_p\dot{\vartheta}^2}{2} \right\} \\ & + \tau((c-1)\lambda_p - cB')\dot{\vartheta}^2 + B\vartheta^2 + G\vartheta\rho - G'\vartheta\dot{\rho} \\ & + c\tau G\dot{\vartheta}\rho - c\tau G'\dot{\vartheta}\dot{\rho} = 0 \end{aligned} \quad (3.1)$$

where the following relations are used to transfer some of the terms under the sign of full derivative:

$$2\vartheta\dot{\vartheta} = \frac{d}{dt} \{ \vartheta^2 \}, \quad 2\dot{\vartheta}\ddot{\vartheta} = \frac{d}{dt} \{ \dot{\vartheta}^2 \}, \quad \vartheta\ddot{\vartheta} + \dot{\vartheta}^2 = \frac{d}{dt} \{ \vartheta\dot{\vartheta} \} \quad (3.2)$$

Similarly, multiplying (2.35b) by $(c\tau\dot{\rho} + \rho)$ generates:

$$\begin{aligned} & \frac{d}{dt} \left\{ \frac{((c+1)\tau\lambda_q + c\tau B - B')\rho^2}{2} + (c\tau G + G')\vartheta\rho \right\} \\ & + (\lambda_q + B)\rho^2 + c(\tau^2\lambda_q - \tau B')\dot{\rho}^2 - G\vartheta\rho \\ & - G'\vartheta\dot{\rho} - c\tau G\dot{\vartheta}\rho - 2c\tau G\vartheta\dot{\rho} + c\tau G'\dot{\vartheta}\dot{\rho} = 0. \end{aligned} \quad (3.3)$$

where the following relations are used:

$$2\rho\dot{\rho} = \frac{d}{dt} \{ \rho^2 \}, \quad \dot{\vartheta}\rho + \vartheta\dot{\rho} = \frac{d}{dt} \{ \vartheta\rho \} \quad (3.4)$$

Then, adding (3.1) and (3.3) together yields:

$$\frac{1}{2} \frac{d\mathcal{V}}{dt} = -\mathcal{Y} \quad (3.5)$$

where the Lyapunov function candidate \mathcal{V} is a quadratic form $\mathcal{V} = y^T P y$ with $y = [\tau\dot{\vartheta} + \vartheta, \dot{\vartheta}, \vartheta, \rho]^T$ and matrix P being:

$$P = \begin{bmatrix} \lambda_p & 0 & 0 & 0 \\ 0 & (c-1)\tau^2\lambda_p & 0 & 0 \\ 0 & 0 & c\tau B - B' & c\tau G + G' \\ 0 & 0 & c\tau G + G' & (c+1)\tau\lambda_q + c\tau B - B' \end{bmatrix} \quad (3.6)$$

For the decay rate \mathcal{Y} , likewise, the following quadratic form $\mathcal{Y} = z^T Q z$ can be obtained, where $z = [\vartheta, \tau\dot{\vartheta}, \tau\dot{\vartheta}, \varrho]^T$ and matrix Q :

$$Q = \begin{bmatrix} B & -cG - \frac{G'}{\tau} & 0 & 0 \\ -cG - \frac{G'}{\tau} & c\lambda_q - \frac{c}{\tau}B' & 0 & 0 \\ 0 & 0 & \frac{c-1}{\tau}\lambda_p - \frac{c}{\tau}B' & 0 \\ 0 & 0 & 0 & \lambda_q + B \end{bmatrix} \quad (3.7)$$

In order for the system to be stable, both Lyapunov function \mathcal{V} and decay rate \mathcal{Y} have to be positive, which is equivalent to positive definiteness of matrices P and Q from (3.6) and (3.7), respectively. Straightforward calculations using Schur's compliment lead to the following conditions for $P > 0$ (assuming that $c > 1$, $G' \ll \tau G$, and $B' \ll \tau B$):

$$\lambda_p > 0 \quad (3.8a)$$

$$\frac{c+1}{c}\lambda_q + B - GB^{-1}G > 0 \quad (3.8b)$$

Likewise, matrix Q is positive definite if:

$$\lambda_p > \frac{c}{c-1}B' \quad (3.9a)$$

$$\lambda_q - B'/\tau - cGB^{-1}G > 0 \quad (3.9b)$$

$$\lambda_q + B > 0 \quad (3.9c)$$

If one assumes that $\lambda_p > 0$ and $\lambda_q > 0$ (which corresponds to both frequency and voltage droop coefficients being positive), conditions (3.8a) and (3.9c) are always satisfied. Moreover, since $c > 1$, $B > 0$, and $B' > 0$, condition (3.9b) is stricter than (3.8b). Therefore, positive definiteness of both P and Q is guaranteed if two conditions, namely, (3.9a) and (3.9b) are satisfied. Assuming that $B' \ll \tau GB^{-1}G$, the following simplified conditions can be obtained:

$$\lambda_p > \frac{c}{c-1}B', \quad \lambda_q > cGB^{-1}G, \quad (3.10)$$

In terms of frequency and voltage droop coefficients k_p and k_q , the above equations can be derived as:

$$k_p < \frac{c-1}{c\omega_0 B'}, \quad k_q < \frac{B}{cG^2}, \quad (3.11)$$

The effect of B' on the system stability is especially evident from these equations; particularly, the active power-frequency mode suffers significantly from the increase of B' . For every value of the constant c , equations (3.11) represent sufficient stability condition corresponding to a rectangular region on the plane of k_p and k_q . Combining all those regions together - varying c from 1 to infinity - one gets the following simplified stability criterion:

$$B'\omega_0 k_p + \Gamma k_q < 1 \quad (3.12)$$

where $\Gamma = G^2/B$.

The illustration of the above stability conditions is given by Figure 3-1 where the predicted stability regions for different values of c from equations (3.11) as well as the total predicted stability region from (3.12) are plotted in the coordinates of per-unit frequency and voltage droop coefficients. The stability boundaries obtained by direct numerical analysis of equations (2.16)-(2.20) as well as (2.27) are also plotted. Moreover, the stability region predicted by the high-order detailed model is further provided to illustrate the performance of the proposed approximation. Even though the k_q predictions among all the cases are quite conservative, the practical reactive power droop gains may not leverage the extended stability range due to induced

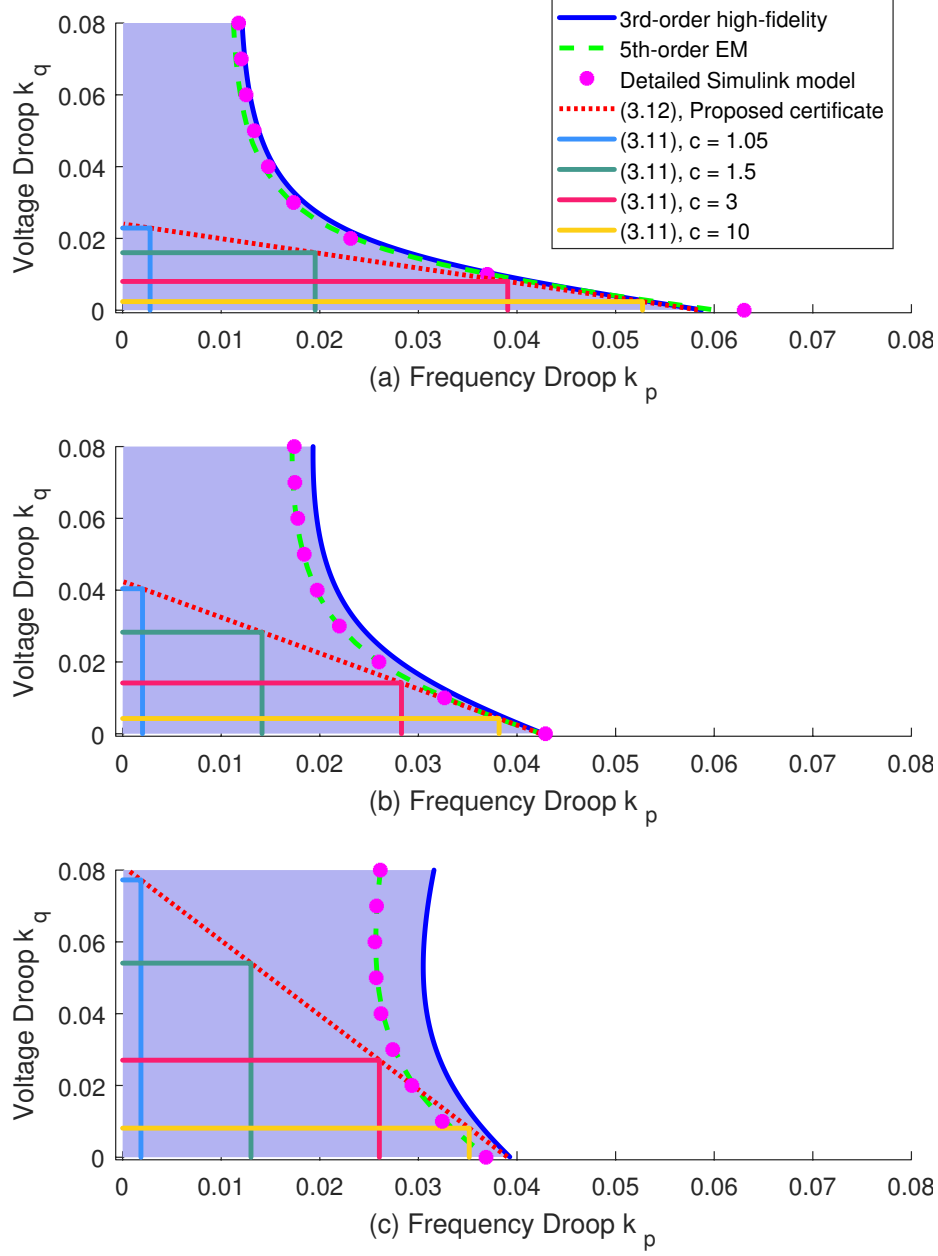


Figure 3-1: Small-signal stability regions of the two-bus system based on different models with respect to the voltage and frequency droop gains ($|Z| = 3\%$): (a) $X/R = 0.667$; (b) $X/R = 1$; (c) $X/R = 1.5$.

voltage drops. Also, it can be seen that the reduced-order model along with the proposed stability certificate tends to perform well when the X/R is around unity. Therefore, in the next chapter such an observation will be considered for practical applications. Finally, the analysis of equations (2.28), (2.34), and (3.12) leads to a general conclusion, that the increase of the impedance to the PCC extends the stable

region of droop coefficients. In fact, the most influential term is B' and it can result in very tight restrictions on the frequency droop gains for small-scale IBMGs.

3.3 Network Generalization

Starting from (2.51), the Lyapunov function and its decay rate for the two-bus case can be directly generalized for networks. Thus, the Lyapunov function is similar to the two-bus case as: $\mathcal{V}(\mathbf{y}) = 0.5\mathbf{y}^T \mathbf{P} \mathbf{y}$ with $\mathbf{y} = [\tau\dot{\boldsymbol{\vartheta}} + \boldsymbol{\vartheta}, \dot{\boldsymbol{\vartheta}}, \boldsymbol{\vartheta}, \boldsymbol{\varrho}]^T$ and the decay rate $\mathcal{Y}(\mathbf{z}) = \mathbf{z}^T \mathbf{Q} \mathbf{z}$ with $\mathbf{z} = [\boldsymbol{\vartheta}, \tau\dot{\boldsymbol{\varrho}}, \tau\dot{\boldsymbol{\vartheta}}, \boldsymbol{\varrho}]^T$. The corresponding \mathbf{P} and \mathbf{Q} matrices are given by:

$$\mathbf{P} = \begin{bmatrix} \mathbf{\Lambda}_p & 0 & 0 & 0 \\ 0 & (c-1)\tau^2 \mathbf{\Lambda}_p & 0 & 0 \\ 0 & 0 & c\tau\mathbf{B} - \mathbf{B}' & c\tau\mathbf{G} + \mathbf{G}' \\ 0 & 0 & c\tau\mathbf{G} + \mathbf{G}' & (c+1)\tau\mathbf{\Lambda}_q + c\tau\mathbf{B} - \mathbf{B}' \end{bmatrix} \quad (3.13)$$

and

$$\mathbf{Q} = \begin{bmatrix} \mathbf{B} & -c\mathbf{G} - \frac{1}{\tau}\mathbf{G}' & 0 & 0 \\ -c\mathbf{G} - \frac{1}{\tau}\mathbf{G}' & c\mathbf{\Lambda}_q - \frac{c}{\tau}\mathbf{B}' & 0 & 0 \\ 0 & 0 & \frac{c-1}{\tau}\mathbf{\Lambda}_p - \frac{c}{\tau}\mathbf{B}' & 0 \\ 0 & 0 & 0 & \mathbf{\Lambda}_q + \mathbf{B} \end{bmatrix} \quad (3.14)$$

Since \mathbf{B} is singular (shunt components are neglected), demanding $\mathbf{Q} > \mathbf{0}$ becomes tricky. Thus, for stability certification, the original Lyapunov stability theorem is no longer effective. In fact, there exists an extended version, the Lasalle's Invariance Principle, stating that the solutions of the autonomous system, $\dot{\mathbf{x}}(t) = f(\mathbf{x}(t))$, asymptotically converge to the largest invariant set if a scalar function $\mathcal{V}(\mathbf{x}(t)) \rightarrow \infty$ as $\|\mathbf{x}(t)\| \rightarrow \infty$ and $\dot{\mathcal{V}}(\mathbf{x}(t)) \leq 0$ over the entire space [36]. This means that the conditions are derived by demanding $\mathbf{P} > \mathbf{0}$ (see Appendix A.1 for further explanations) and $\mathbf{Q} \geq \mathbf{0}$ (relaxation to positive semi-definite). Thus, generalization of (3.10) can

be obtained:

$$\Lambda_p - \frac{c}{c-1} \mathbf{B}' \succeq \mathbf{0} \quad (3.15a)$$

$$\Lambda_q - c \mathbf{G} \mathbf{B}^g \mathbf{G} \succeq \mathbf{0} \quad (3.15b)$$

where the above conditions are obtained using the Schur's compliment, and \mathbf{B}^g denotes the generalized inverse of \mathbf{B} with the constraint $(\mathbf{I} - \mathbf{B}\mathbf{B}^g)\mathbf{G} = \mathbf{0}$ satisfied. For now, it becomes quite intriguing to see whether the above generalization can be directly applied to (3.12). In fact, the result may not be helpful for practical usage since checking matrix inequalities in (3.15) is most of the time a numerical procedure. Therefore, an approximation procedure of obtaining simple and analytical conditions will be revealed in the next chapter.

3.4 Conclusions

In this chapter, the stability certificates were provided through constructing the Lyapunov function candidates for both the simple two-bus and network cases. Specifically, the quadratic construction method is useful to identify the practical Lyapunov function candidates for linear systems. Although the two-bus scalar criteria can be trivially checked, for the network settings the stability certificate requires examination of the matrix inequalities and are challenging for further simplification. For more practical usage, there is a need to approximate the network criteria into a more friendly form, which will be investigated in the next chapter.

Chapter 4

Stability Enhancement

4.1 Introduction

It can be seen in Figure 3-1 that the system suffer from limited active power droop gain, k_p , which is mainly constrained by the transient susceptance B' . Thus, inspection of (2.28) shows that, in general, the transient susceptance B' is inversely proportional to the total impedance, $B' \propto (\omega_0 |\underline{Z}|)^{-1}$, and is given by:

$$B' = \frac{2LXR}{(X^2 + R^2)^2} = \frac{2X^2R}{\omega_0 |\underline{Z}|^4} \quad (4.1)$$

This means that B' increases when the coupling between the inverter and PCC becomes stronger (e.g. connection with a short line) and a specific increase in the value of coupling impedance could be required to guarantee stability of certain operating points. For the reactive power droop gain, it is not much of an issue as can be seen from Figure 3-1. In fact, the proposed stability criterion in (3.12) captures the k_q bound by using $\Gamma \propto |\underline{Z}|^{-1}$:

$$\Gamma = \frac{G^2}{B} = \frac{R^2}{X|\underline{Z}|^2} \quad (4.2)$$

Although the predicted k_q region is relatively conservative, high values of k_q may be considered uncommon due to induced voltage drops. This practical consideration enables the use of the proposed certificate that balances the active and reactive droop

gains in the same scale. To extend the stable regions of the droop gains, adding a large amount of physical impedance into the system is not practical due to the size and cost of required inductors/resistors. Therefore, emulation of virtual components (e.g. inductance, reactance, or resistance) via high-bandwidth digital controllers have been commonly seen in literature [12,23,25,26,30]. Consider now that the total impedance \underline{Z} is reformulated as

$$\underline{Z}(s) = \underline{Z}_{mc}(s) + \underline{Z}_l(s) \quad (4.3)$$

where $\underline{Z}_l(s)$ is the line impedance to the PCC and $\underline{Z}_{mc}(s) = \underline{Z}_m(s) + \underline{Z}_c(s)$ is the aggregation of the virtual and coupling impedances, which will be referred as *controlled impedance* since it is the known and controllable parameters (recall that $\underline{Z}(s) = R + jX + sL$). By choosing a particular X_{mc}/R_{mc} , it is possible to show that $B'\omega_0$ and Γ are strictly decaying given the X_l/R_l ratio of the line. An example of using a certain line characteristic is demonstrated in Figure 4-1 [13]. This idea is very interesting and will serve as the core for deriving useful and concise approximation for the stability criteria in (3.15).

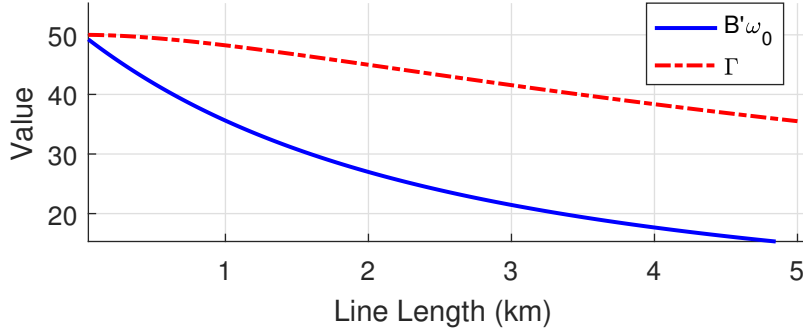


Figure 4-1: Variation of $B'\omega_0$ and Γ with respect to the line length ($X_{mc} = R_{mc} 1\%$, and $X_l/R_l = 0.5$).

4.2 Approximated Stability Rules

Proceeding with the stability criteria in (3.15), one can search for a set of virtual impedances for stable operation given the desired droop gains of an IBMG. However, these conditions in (3.15) are not very intuitive for control engineers to size virtual

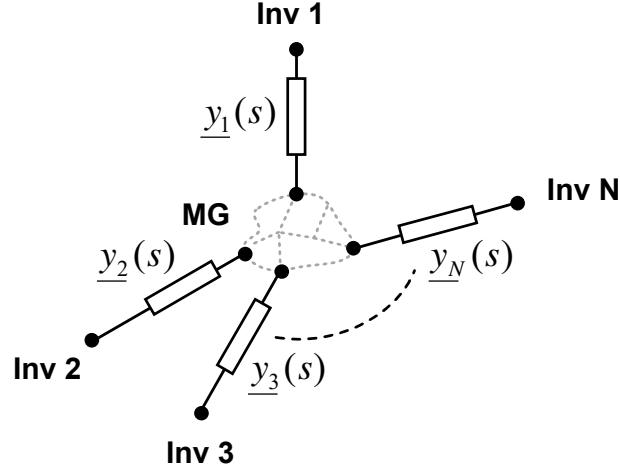


Figure 4-2: Star topology of a microgrid by aggregating the network into a single node.

impedances. Therefore, in this section, an approximation is intended to obtain simple and concise rules for tuning virtual impedances. Since it is possible to choose a particular X/R ratio of the controlled impedance (virtual and coupling) to achieve the decaying property of B' and Γ with respect to the additional line length (as illustrated in Figure 4-1), one can design the controlled impedances by assuming a worst-case scenario, which is a set of inverters $i \in \mathcal{N}$ connected to a PCC node only with their controlled impedances and no lines, as shown in Figure 4-2. Furthermore, all inverters are imposed to have the same X_{mc}/R_{mc} ratio of their controlled impedances. Under this condition, the controlled admittance of inverter i can be written as (see (2.8) for detailed explanations):

$$\underline{y}_i(s) = \alpha_i \underline{y}(s) = \frac{\alpha_i}{R_{mc} + jX_{mc} + sL_{mc}} \quad (4.4)$$

where $\underline{y}(s)$ is some reference admittance common for all inverters (recall that the underline denotes a complex value), and α_i is the positive scaling factor for inverter i . Then, the admittance matrix of the original network (inverters connected to PCC) can be represented as an $(N + 1) \times (N + 1)$ matrix $\underline{\mathbf{Y}}_{PCC}(s) = \underline{y}(s)\Psi_{PCC}$, where Ψ_{PCC} denotes the following matrix (the subscript PCC is referring to the system

before the Kron reduction):

$$\Psi_{PCC} = \left[\begin{array}{ccc|c} \alpha_1 & \cdots & 0 & -\alpha_1 \\ \vdots & \ddots & \vdots & \vdots \\ 0 & \cdots & \alpha_N & -\alpha_N \\ \hline -\alpha_1 & \cdots & -\alpha_N & A \end{array} \right] \quad (4.5)$$

Here, the top-left block represents a diagonal $N \times N$ matrix with elements α_i (denoted it as Φ), and

$$A = \sum_{i=1}^N \alpha_i. \quad (4.6)$$

Since the Kron reduction only affects matrix Ψ_{PCC} (all the controlled impedances are of the same X/R ratio), the reduced $N \times N$ admittance matrix $\underline{\mathbf{Y}}(s)$ becomes:

$$\underline{\mathbf{Y}}(s) = y(s)\Psi, \quad \Psi = \Phi - A^{-1}\mathbf{a}\mathbf{a}^T \quad (4.7)$$

where $\mathbf{a} = [\alpha_1 \cdots \alpha_N]^T$. The convenience of representation (4.7) lies in the fact that all the matrices \mathbf{B} , \mathbf{G} and \mathbf{B}' from (3.15) are proportional to the same matrix Ψ :

$$\mathbf{B} = -\text{Im} \{ \underline{\mathbf{Y}}_N^0 \} = b\Psi, \quad b = \frac{X_{mc}}{R_{mc}^2 + X_{mc}^2} \quad (4.8)$$

$$\mathbf{G} = \text{Re} \{ \underline{\mathbf{Y}}_N^0 \} = g\Psi, \quad g = \frac{R_{mc}}{R_{mc}^2 + X_{mc}^2} \quad (4.9)$$

$$\mathbf{B}' = \text{Im} \{ \underline{\mathbf{Y}}_N^1 \} = b'\Psi, \quad b' = \frac{2L_{mc}X_{mc}R_{mc}}{(R_{mc}^2 + X_{mc}^2)^2} \quad (4.10)$$

where the definition for the matrices \mathbf{B} , \mathbf{G} and \mathbf{B}' can be found in equations (2.48) and (2.50). The reason behind the proportional property is because all the controlled

impedances are of the same X/R ratio. Therefore, (3.15) can be rewritten as:

$$\boldsymbol{\Lambda}_p - \frac{c}{c-1}b\boldsymbol{\Psi} \geq \mathbf{0} \quad (4.11a)$$

$$\boldsymbol{\Lambda}_q - c\frac{g^2}{b}\boldsymbol{\Psi} \geq \mathbf{0} \quad (4.11b)$$

where $\mathbf{G}\mathbf{B}^g\mathbf{G} = (g^2/b)\boldsymbol{\Psi}$ in (4.11). In fact, the matrix $\mathbf{a}\mathbf{a}^T$ in (4.7) is always positive semi-definite and A is positive so that:

$$\boldsymbol{\Phi} = \boldsymbol{\Psi} + A^{-1}\mathbf{a}\mathbf{a}^T \geq \boldsymbol{\Psi} \quad (4.12)$$

Therefore, conditions (4.11) can be substituted by more conservative ones:

$$\boldsymbol{\Lambda}_p - \frac{c}{c-1}b'\boldsymbol{\Phi} \geq \mathbf{0} \quad (4.13a)$$

$$\boldsymbol{\Lambda}_q - c\frac{g^2}{b}\boldsymbol{\Phi} \geq \mathbf{0}. \quad (4.13b)$$

Since $\boldsymbol{\Phi} = \text{diag}([\alpha_1 \dots \alpha_N])$ is a diagonal matrix, now all matrices in (4.13) are diagonal and positive semi-definiteness can be certified by considering separate conditions for every diagonal element, i.e:

$$\lambda_{p,i} \geq \frac{c}{c-1}b'\alpha_i, \quad \forall i \in \mathcal{N} \quad (4.14a)$$

$$\lambda_{q,i} \geq c\frac{g^2}{b}\alpha_i, \quad \forall i \in \mathcal{N} \quad (4.14b)$$

or equivalently (recall that $\lambda_{p,i} = (\omega_0 k_{p,i})^{-1}$ and $\lambda_{q,i} = k_{q,i}^{-1}$ in (2.47)):

$$k_{p,i} \leq \frac{c-1}{c\omega_0 b'\alpha_i}, \quad \forall i \in \mathcal{N} \quad (4.15a)$$

$$k_{q,i} \leq \frac{b}{cg^2\alpha_i}, \quad \forall i \in \mathcal{N} \quad (4.15b)$$

where every condition is directly analogous to equations (3.11) for the two-bus case.

4.3 Plug-and-Play Compliant Control Rules

Equations in (4.15) imply that the stability criteria are approximated from matrix inequalities to a set of scalar conditions for individual inverters. That is, this set of distributed rules are given to allow the selection of the controlled impedance independent of the network and other inverters. In the thesis, such functionality is referred as the Plug-and-Play (PnP) compliant control - introduction of new inverters only needs to satisfy these approximated local rules for droop stability. Similar to the derivation of (3.12), equations in (4.15) produce the following criterion:

$$b' \omega_0 \alpha_i k_{p,i} + \frac{g^2}{b} \alpha_i k_{q,i} < 1, \quad \forall i \in \mathcal{N} \quad (4.16)$$

With the particular choice of $X_{mc} = \omega_0 L_{mc} = R_{mc}$ (based on the assumption of the line characteristic, $X_l/R_l = 0.5$), substituting b' , g , and b in equations (4.8)-(4.10), (4.16) can be further simplified to:

$$k_{p,i} + k_{q,i} < 2X_{mc,i}, \quad \forall i \in \mathcal{N} \quad (4.17)$$

where $X_{mc,i} = X_{mc}/\alpha_i$ and the equation becomes fairly simple to use for sizing the virtual impedances. Also, the choice of $X_{mc}/R_{mc} = 1$ can further benefit the performance of the stability rules and the fidelity of the reduced-order model as depicted in Figure 3-1.

Table 4.1: Distances in Kilometers to PCC of Five-Inverter Test Cases: $X_l = 0.28\%\text{km}^{-1}$, $R_l = 0.56\%\text{km}^{-1}$.

Case	Line 1	Line 2	Line 3	Line 4	Line 5
1	0.5	3.0	2.5	0.7	1.5
2	0.0	3.0	2.5	0.0	1.5
3	0.0	0.0	0.0	0.0	0.0
4	0.0	∞	∞	0.0	∞

To verify the proposed control rules, a simple five-inverter to PCC system is constructed with arbitrary line lengths as shown in Table 4.1. The projected stability

regions based on (2.51) along with the region given in (4.17) are plotted with respect to the universal droop gains (k_p and k_q are the same for all inverters) as shown in Figure 4-3. First, it can be identified that Case 1 with the greatest scale gives the largest projected stability region; however, whenever there are short paths (between Inverter 1 and Inverter 4) the region becomes bottle-necked by such connections so that Case 3 and Case 2 are almost identical. In fact, this issue has been identified in [37] for multi-microgrid stability and referred as *critical links*. It should also be emphasized that Figure 4-3 may not be sufficient to reflect the actual multi-dimensional stability regions since the droop gains are constrained to be equal for all inverters.

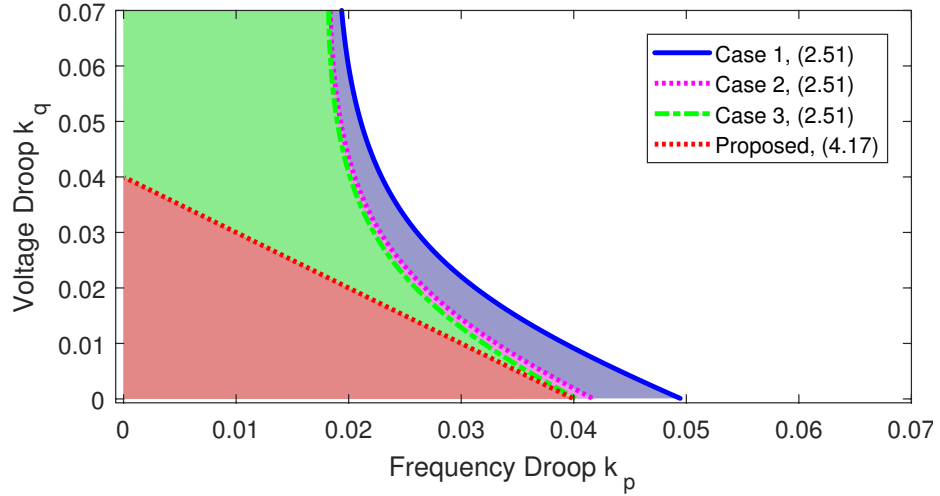


Figure 4-3: Comparison of low-dimensional projected stability regions of (4.17) and (2.51) for a microgrid with five inverters ($n = 5$, star topology) of different scales with symmetric droop gains and controlled impedances: $k_{p,i} = k_p$, $k_{q,i} = k_q$, $X_{mc,i} = R_{mc,i} = 2\%$ (line parameters are shown in Table 4.1).

Therefore, in Figure 4-4 the stability boundaries from different perspectives are plotted with respect to the active power droop gains of Inverter 1 and Inverter 4 (k_{p1}, k_{p4}) to show the effect of the critical links: the remaining droop gains are fixed as described and one can imagine slicing Figure 4-3 by different k_q gains. First, significant reduction of stability regions is mainly affected by the short distance between Inverter 1 and Inverter 4 by comparing Case 1 and Case 2 (zeroing Line 1 and Line 4), whereas the region reduction becomes insignificant from zeroing other lines (between Case 2 and Case 3). Also, similar to Figure 4-4, the proposed PnP rules show further

conservativeness as k_q increases. In Figure 4-5 ($k_{q,i} = 0\%$), Case 4 is introduced to demonstrate the greatest stability region due to infinite lengths of lines 2, 3 and 5 (such a condition effectively reduces to a two-inverter system). By adding inverters back in and reducing their lines to the PCC (Case 2 and Case 3, sequentially), it can be seen that the stability region reduces and is eventually of a square shape. In fact, the proposed PnP rules predict the same boundary as Case 4 indicating conservative predictions against the worst-case scenario with no lines.

4.4 Power Sharing of Multiple Inverters

As stated in Section 1.2, the power sharing for multiple inverters depends on their relative droop gains. While the reactive power sharing is sensitive to the network characteristics, the active power sharing, in general, depends on (2.17) since the frequency is a universal signal. Therefore, in steady-state, one can obtain the ideal power sharing equation:

$$k_{p,1}P_1 = k_{p,2}P_2 = \dots = k_{p,i}P_i, \quad \forall i \in \mathcal{N} \quad (4.18)$$

By defining $k_{p,i} = k_p/s_i$ with k_p being the common droop base and s_i denoting the sharing ratio, the sharing equation becomes:

$$\frac{P_1}{s_1} = \frac{P_2}{s_2} = \dots = \frac{P_i}{s_i}, \quad \forall i \in \mathcal{N} \quad (4.19)$$

In fact, this notation of sharing ratio s_i becomes convenient for investigating multi-dimensional stability regions. If the notation is chosen: $k_{p,i} = k_p/s_i$ and $k_{q,i} = k_q/s_i$, where k_p and k_q denote the parameters base, (4.17) can be rewritten as:

$$k_p + k_q < 2s_i X_{mc,i}, \quad \forall i \in \mathcal{N} \quad (4.20)$$

The above equation indicates that the inverters with smaller sharing ratios demand larger controlled impedances since the left-hand terms of the N conditions are con-

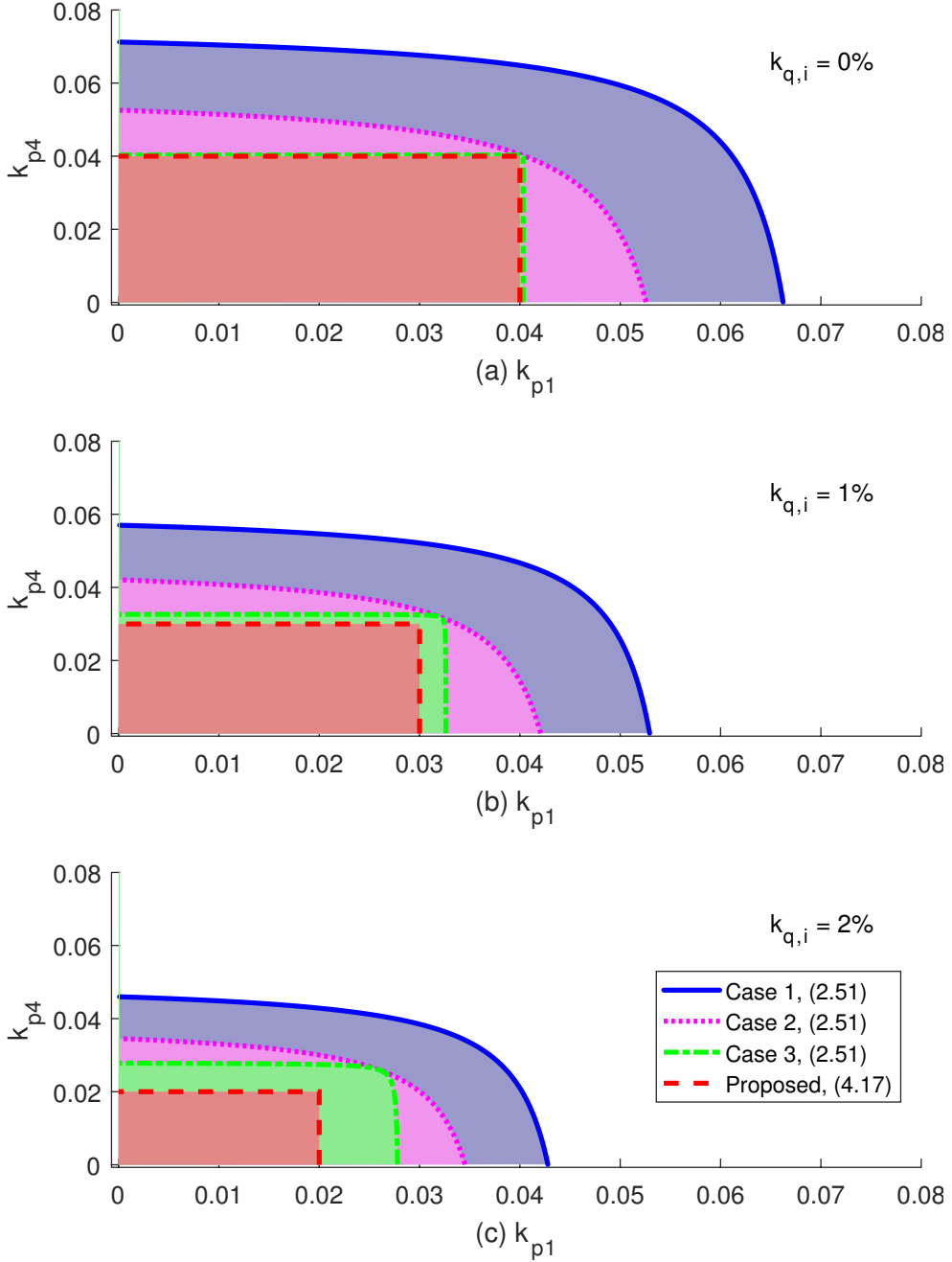


Figure 4-4: Comparison of projected stability regions with respect to k_{p1}, k_{p4} : $X_{mc,i} = R_{mc,i} = 2\%$; (a) $k_{p2} = k_{p3} = k_{p5} = 4\%$, $k_{q,i} = 0\%$; (b) $k_{p2} = k_{p3} = k_{p5} = 3\%$, $k_{q,i} = 1\%$, (c) $k_{p2} = k_{p3} = k_{p5} = 2\%$, $k_{q,i} = 2\%$ (line parameters are shown in Table 4.1).

stant. Therefore, it is convenient to scale the controlled impedance according to the sharing ratio, $X_{mc,i} = X_{mc}/s_i$, where X_{mc} is the reactance of the common controlled

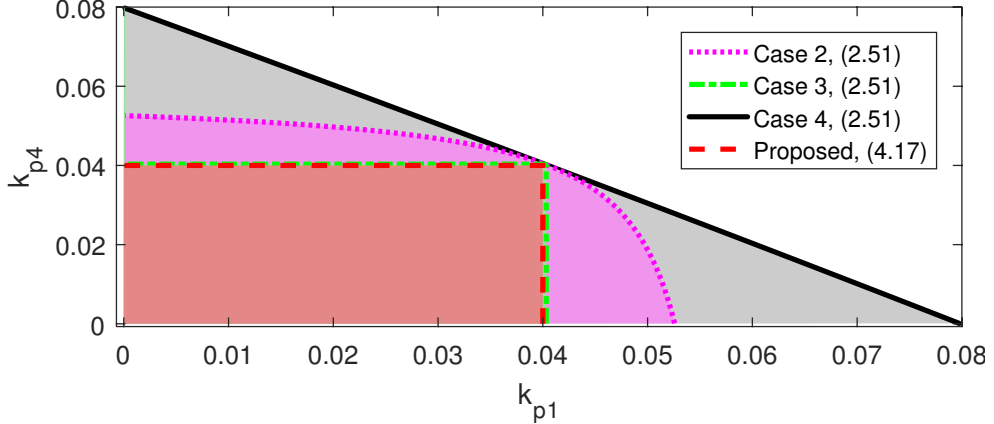


Figure 4-5: Comparison of projected stability regions with respect to k_{p1}, k_{p4} : $X_{mc,i} = R_{mc,i} = 2\%$, $k_{p2} = k_{p3} = k_{p5} = 4\%$, $k_{q,i} = 0\%$ (line parameters are shown in Table 4.1).

impedance. Thus, (4.20) reduces to a single condition:

$$k_p + k_q < 2X_{mc} \quad (4.21)$$

By satisfying the above condition, the N local conditions are automatically satisfied if both droop gains and controlled impedances are scaled proportionally using s_i . Therefore, in this thesis, the usage of s_i will be abused for convenience due to difficulty in visualizing multi-dimensional stability regions.

4.5 Implementation of Virtual Impedances

4.5.1 Conventional Virtual Impedance Control

Virtual impedance control has been widely adopted to provide enhancement of droop stability due to its effectiveness [12, 23, 25, 26, 30]. Generally, the concept is derived from emulating the dynamics of a physical set of inductors in response to the output current via the voltage control. Figure 4-6 shows that from the terminal, the inverter behaves like an internal voltage source connected to its terminal via a virtual impedance. In synchronous reference frames (with ω denoting the frequency), the

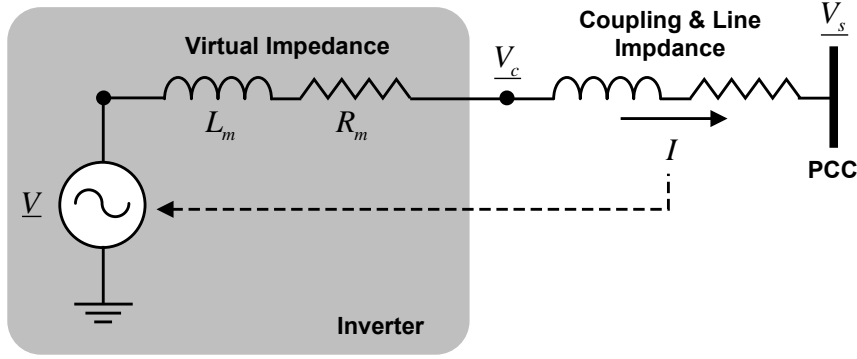


Figure 4-6: Equivalent circuit of the virtual impedance.

dynamic equation of the virtual impedance becomes:

$$\underline{V} - \underline{V}_c = R_m \underline{I} + j\omega L_m \underline{I} + L_m \frac{d\underline{I}}{dt} \quad (4.22)$$

where \underline{V} and \underline{V}_c are reference and capacitor voltages, respectively, \underline{V}_s is the stiff voltage at the PCC, and R_m and L_m are the virtual resistance and inductance, respectively. Now assuming that the inverter has an ideal voltage controller such that capacitor voltage \underline{V}_c equals to a given voltage reference, \underline{V}_c^* , the following control form in dq reference frames can emulate the dynamics described in (4.22) [25]:

$$V_{cd}^* = V - R_m I_d + \omega L_m I_q - \frac{\omega_f s}{s + \omega_f} L_m I_d \quad (4.23a)$$

$$V_{cq}^* = 0 - R_m I_q - \omega L_m I_d - \frac{\omega_f s}{s + \omega_f} L_m I_q \quad (4.23b)$$

where the d -axis is aligned with the internal voltage source so that $\underline{V} = V + j0$ and $\underline{V}_c^* = V_{cd}^* + jV_{cq}^*$, and ω_f is cut-off frequency for the filtered derivative terms. After selecting the desired impedance, one can simply implement the equations (4.23a) and (4.23b) with the typical internal control containing two regulator loops (the current control and voltage loops shown in Figure 2-1).

Since the configuration of the internal control contains many feedback loops, its closed-loop stability should raise certain concerns (the details of typical internal control design are shown in Appendix A.2). To study the effect of the virtual impedance

on internal stability, it is not straightforward to analyze the system separately (voltage controllers are still coupled due to imperfect feed-forward compensation). Thus, it is convenient to employ complex transfer functions so that both voltage and current become phasors [38].

Now consider a simplified block diagram by setting R_m and L_m to zero for simplicity, as shown in Figure 4-7, where the non-ideal voltage regulator can be represented using the complex transfer function $\underline{C}_v(s)$ of output capacitor voltage to the input voltage reference. The overall open-loop system becomes:

$$\underline{Q}(s) = \underline{C}_v(s) \frac{jX_m}{\underline{Z}_t(s)} \quad (4.24)$$

where $\underline{Z}_t(s) = R_t + sL_t + X_t$ is used to denote the aggregation of coupling and line impedance (see notation in (2.8)). Figure 4-8 shows that the bode plots of $\underline{Q}(s)$ for different X_m based on an inverter with the zero line length. It should be noticed that the frequency axis is defined as $sgn(\omega)\log_{10}|\omega|$ with the control and filter parameters taken from [13]. Also, the positive (negative) frequency is to denote the forward (reverse) rotation. From Figure 4-8, it can be identified that for the positive frequency range, keeping sufficient phase and gain margins is not much a problem; however, in negative frequency range the system could attain a gain higher than unity with 180° phase shift, resulting in closed-loop instability. The main causes of such a phenomenon are twofold: (1) High virtual reactance increases the overall gain; (2) The voltage regulator $\underline{C}_v(s)$ introduces additional positive phase shift (like delays) at negative frequency. From the investigation, it shows that a trade-off has to be made between the droop and internal stability through adjusting the virtual reactance: A larger impedance deteriorates internal stability while a smaller impedance may result in droop instability. This issue makes the design of the control constrained and sensitive. Therefore, there is a need for a improved control scheme.

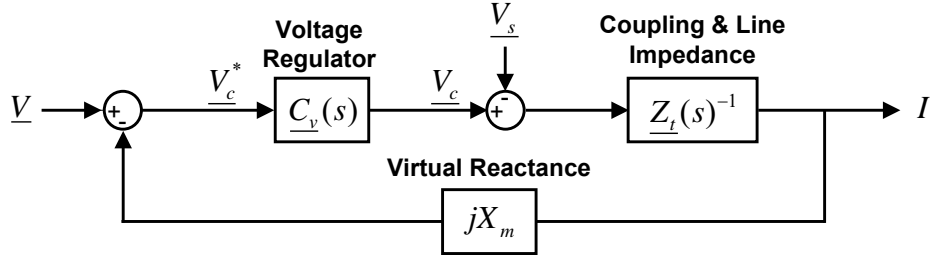


Figure 4-7: Block diagram of the virtual reactance method.

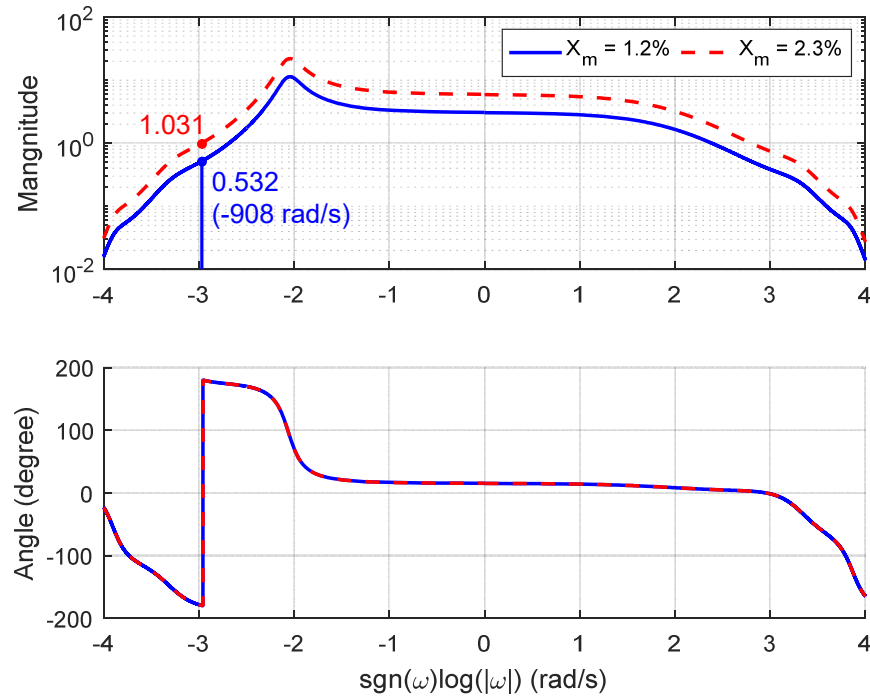


Figure 4-8: Bode plots of (4.24) for different X_m (zero line length).

4.5.2 Proposed Virtual Impedance Control

In this subsection, the main focus is to develop the control structure that provides direct emulation of dynamic behavior of impedances without an explicit voltage control loop, which causes unnecessary delays and phase shifts. First, the equivalent circuit of the filter current injection into the PCC is shown in Figure 4-9(a), where $\underline{Z}_t(s)$ denotes the aggregated coupling and line impedance, and $\underline{Z}_s(s) = (sC_f + j\omega C_f)^{-1}$ denotes the shunt impedance (filter capacitors). The filter current I_f is generally reg-

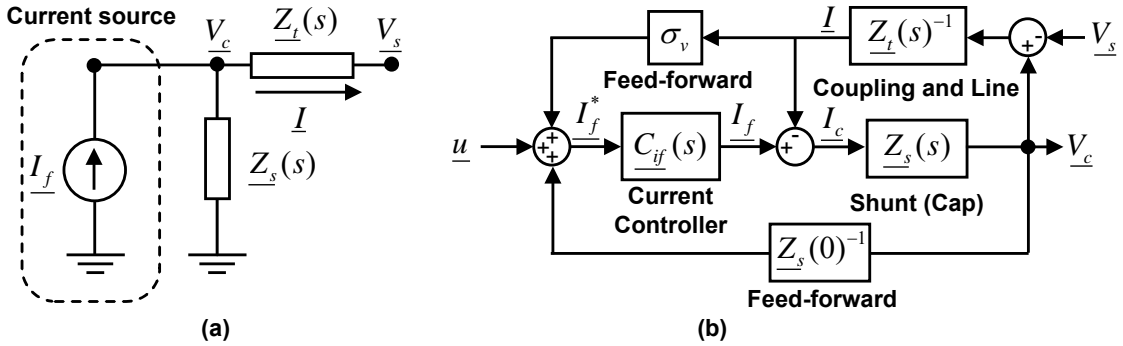


Figure 4-9: (a) Filter current injection into the PCC; (b) Block diagrams of the internal control.

ulated with high bandwidth current controller; thus, it is convenient and simpler to assume $I_f = I_f^*$ for derivations so that the transfer function from I_f^* to V_c becomes:

$$\underline{V}_c = \frac{\underline{Z}_t(s)\underline{Z}_s(s)}{\underline{Z}_t(s) + \underline{Z}_s(s)} I_f^* \quad (4.25)$$

Then, the filter current reference can be generated as (in analogy to (A.4)):

$$I_f^* = \underline{u} + \sigma_v \underline{I} + \underline{Z}_s(0)^{-1} \underline{V}_c \quad (4.26)$$

where \underline{u} denotes the temporary reference input, σ_v is the output current feed-forward gain, and $\underline{Z}_s(0) = (j\omega C_f)^{-1}$ is the steady-state shunt impedance of the capacitor filter. The last two terms of (4.26) are normally referred as the feed-forward compensation, which aims at canceling the known disturbances of output current and the capacitor current in synchronized reference frames. Now it becomes interesting to explore the open-loop characteristics from \underline{u} to V_c , which can be depicted using the block diagram shown in Figure 4-9(b). By using the standard loop deduction technique, one can obtain the synthesized form of:

$$\underline{V}_c = \frac{\underline{Z}_s'(s)\underline{Z}_t(s)}{\underline{Z}_s'(s) + \underline{Z}_t(s)} \underline{I}^* + \frac{\underline{Z}_s'(s)}{\underline{Z}_s'(s) + \underline{Z}_t(s)} \underline{V}_s \quad (4.27)$$

where $\underline{Z}'_s(s) = (1 - \sigma_v)/sC_f$ and $\underline{I}^* = \underline{u}/(1 - \sigma_v)$ is the output current reference. In fact, equation (4.27) represents an equivalent circuit shown in Figure 4-10.

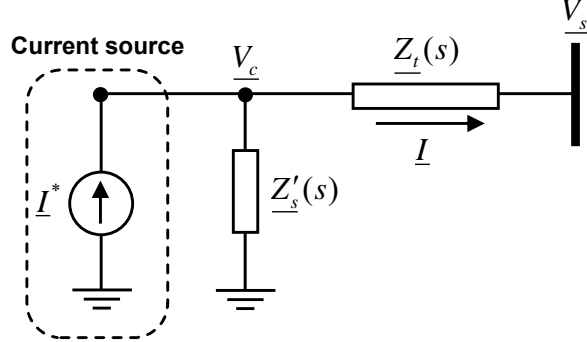


Figure 4-10: The equivalent circuit of (4.27).

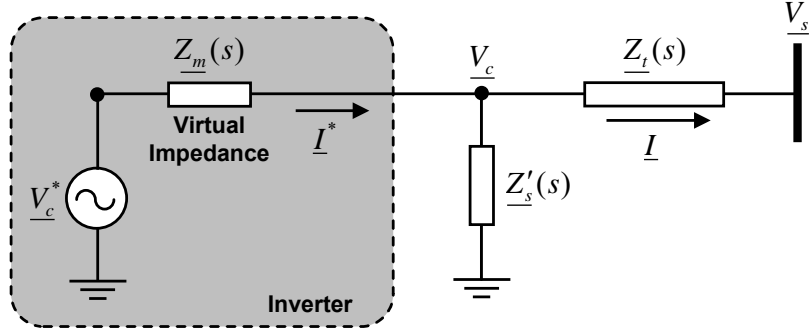


Figure 4-11: The equivalent circuit of the virtual impedance.

The equivalent circuit in Figure 4-10 shows that the control structure allows to regulate the output current into the PCC (the shunt element, $\underline{Z}'_s(s)$, becomes infinite in steady-state). Thus, to emulate the dynamic behavior of the virtual impedance, the output current reference can be computed by measuring the terminal voltage \underline{V}_c :

$$\underline{I}^* = \frac{\underline{V} - \underline{V}_c}{\underline{Z}_m(s)} \quad (4.28)$$

where $\underline{Z}_m(s) = sL_m + R_m + jX_m$ denotes the virtual impedance. The overall system is illustrated in Figure 4-11. It should be emphasized that there are many possible alternative forms in the literature [12, 23, 30]. In the thesis, the main concept is to

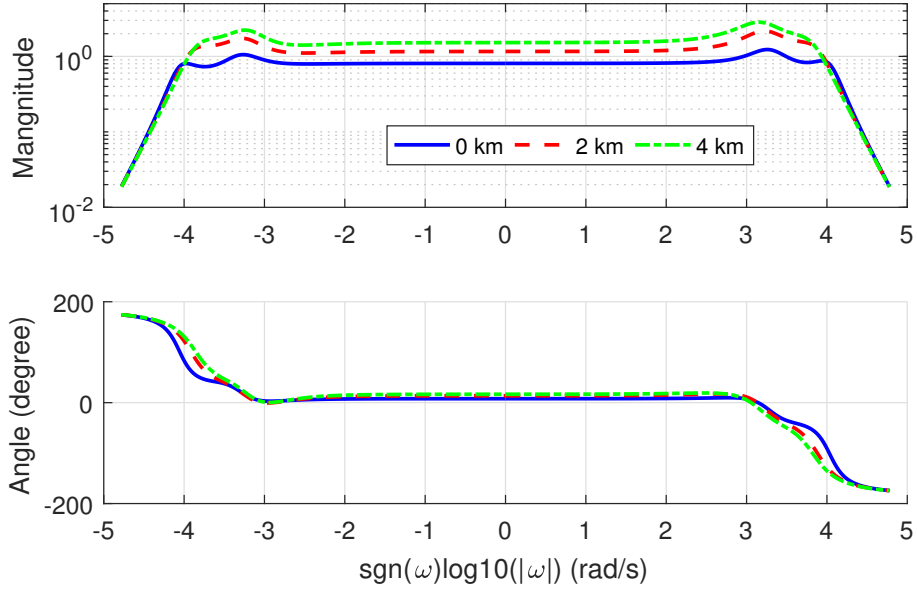


Figure 4-12: Bode plots of the transfer functions with different line lengths.

allow direct emulation of the dynamical responses of the impedance without the need of an explicit voltage control loop. Also, it is very common to employ virtual damper circuits (along with physical damper circuits) to mitigate the resonance of the CL network. The general idea is to add an RC filter in parallel to the output capacitor by adding the damping current into the current references:

$$\Delta \underline{I}^* = \frac{s/R_{vd}}{s + 1/(R_{vd}C_{vd})} V_c \quad (4.29)$$

where R_{vd} and C_{vd} are the virtual resistance and capacitance, respectively. With the virtual damper control and considering the filter current regulation, the bode plots of the transfer function from \underline{I}^* to \underline{V}_c based on different line lengths are shown in Figure 4-12. It can be observed the gains of 180 degree phase shifts in both positive and negative frequency regions are much smaller than unity. Although adding virtual impedance may reshape the bode plot shown in Figure 4-12, it actually reduces the overall gain as can be seen in (4.29). Thus, the issue of internal oscillation with large virtual impedance does not persist with the proposed control. Also it should be emphasize that the shunt elements are quite insignificant in affecting the droop

stability due to their much greater values as compared to the series elements around the frequency of the droop mode. Effectively, only series impedances are considered for droop stability.

4.5.3 Voltage and Power Quality

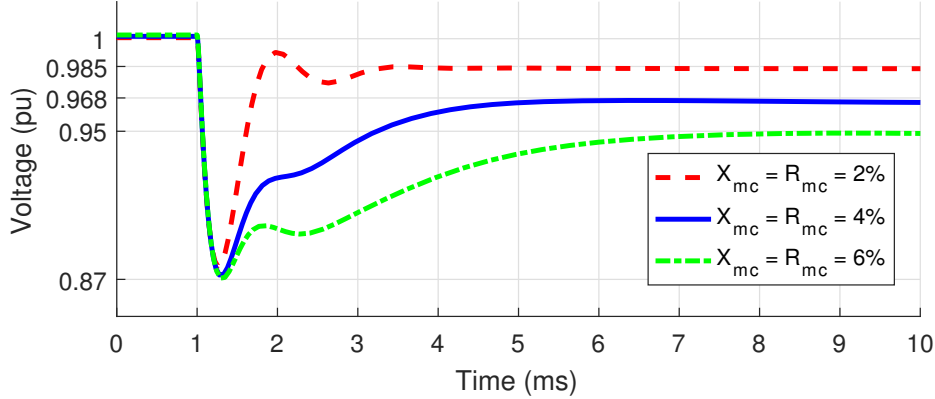


Figure 4-13: Output voltage responses for a sudden load change (1 pu resistive) with different controlled impedances (virtual and coupling impedances).

Employing large virtual impedances helps to mitigate droop instability and allows a wider margin for tuning frequency and voltage droop coefficients. However, steady-state voltage deviations are affected (the transient voltage dips are more relevant to the internal inverter control and filter parameters). For example, the output voltage responses for a single inverter under resistive load stepping of 1 pu for different controlled impedances ($Z_{mc}(s) = Z_m(s) + Z_m(s)$) are shown in Figure 4-13. It is evident from Figure 4-13 that the values of transient dip are similar for all three cases - around 0.87 pu . The steady-state voltage drops, however, are significantly different (98.5%, 96.8%, 95%) and depend on the amount of virtual impedance. This means that using large virtual impedances may result in significant steady-state voltage drops, in fact, on top of the droop drops. Therefore, compromises need to be made between sharing accuracy, droop stability, and voltage/frequency variations, which are typical for droop-controlled sharing schemes. In general, for voltage/frequency sensitive applications, a secondary compensation scheme is recommended to resolve such an

issue [1].

4.6 Conclusions

This chapter addressed on the topic of stability enhancement. The approximated stability rules were first proposed to allow the flexible integration of inverters to form a microgrid. In addition, the details of the proposed virtual impedance method had been shown with an emphasis on direct emulation of virtual impedance without an explicit voltage control loop. The design principles and the effects of the virtual impedance method were well revealed to provide a guideline for the development of primary (droop) control.

Chapter 5

Secondary Compensation

5.1 Introduction

For islanded operation, voltage and frequency regulation capability is essential for the MGs to maintain reliable and sufficient energy supply to loads. Although droop control allows power sharing and set-point regulation between inverters without communication, the major drawback of droop control is voltage and frequency deviations.

To handle the droop drops, compensation schemes have been proposed in [1,39–42] to achieve set-point restoration in both DC and AC MG control. Particularly, the hierarchical control scheme commonly used in conventional power systems is well suitable for energy management in MGs, as shown in Figure 5-1 [1]. The reason is that such hierarchical structure allows the separation of objectives and priorities based on different time scales: First, droop control (also referred as primary control) is responsible for fast dynamics and power sharing. Then, secondary control takes on the tasks for efficiency optimization such as power dispatch and set-point restoration. Finally, tertiary control allows energy transfer in between microgrids and external grids (for islanded microgrids, tertiary control is not implemented). Based on this simple structure, the reliability can be significantly improved since it encourages the error-proof design for each layer against failures from other layers. For example, if communication or secondary control fails, droop control can still maintain equal power sharing among inverters (though inevitable set-point deviation exists). The approach brings

the potential of using communication to enhance regulation capability while securing system reliability. In addition, many recent papers [1, 39, 43] have demonstrated the significant benefits of communication to enhance system reliability, power quality, and stability.

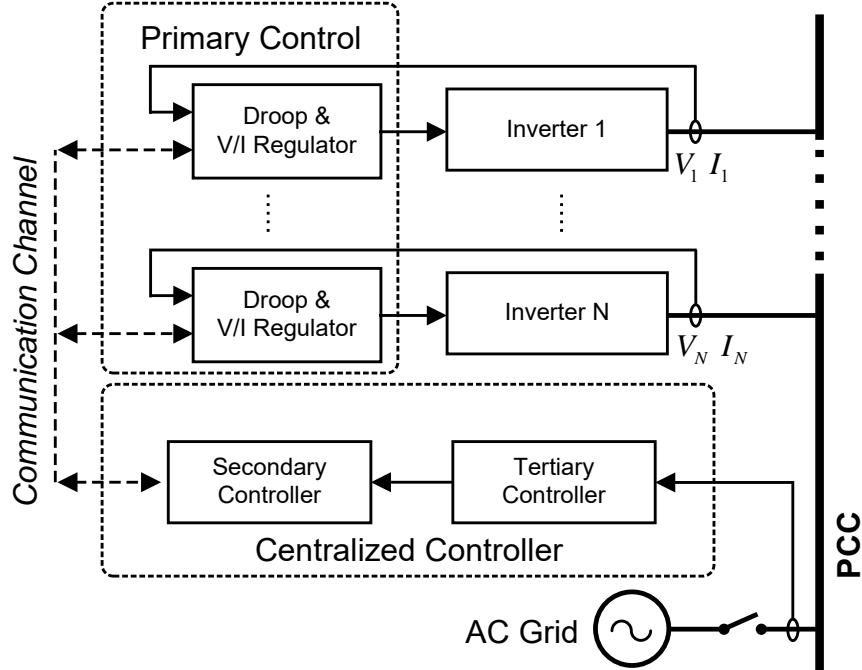


Figure 5-1: Hierarchical control of AC Microgrids [1].

When it comes to the implementation, physical connections may vary from different devices based on Ethernet, optical fibers, wireless/radio techniques, or power line communication (PLC). To incorporate different types of devices, IEC61850 was suggested in [44] as a common protocol for exchanging data. Among different means, cost-effective solutions using PLC can be seen in low voltage distribution networks. However, since power lines are not originally designed for data transmission, it had been reported that data transmission using PLC suffers signal attenuation in time-varying or capacitive load conditions, resulting undesirable communication [45]. An alternative way of employing the Controller Area Network (CAN) protocol was also proposed for MG control, showing the potential of reducing the cost of communication due to its high availability in modern power electronics applications [46].

In general, high-bandwidth communication may be of favorable solutions. How-

ever, in many applications sophisticated communication infrastructure may add up the burden for securing a reliable and affordable energy solution. As a result, using non-explicit communication to assist MG management scheme is likely to be more feasible. In fact, droop-based control schemes are well suitable for the use of cost-effective communication due to their communication-free mechanism of high bandwidth. Thus, only low-bandwidth secondary compensation signals are needed to adjust the voltage and frequency set-points. This brings further flexibility and failure tolerance for microgrid operations. In the following sections, the development of the secondary control for islanded microgrids will be investigated in details.

5.2 Set-Point Restoration

5.2.1 Naive Compensation

The basic principle of secondary compensation can be obtained by modifying equations (1.6a) and (1.6b):

$$\omega_i = \omega^{set} - k_{pi}P_i + \Delta\omega_i \quad (5.1a)$$

$$V_i = V^{set} - k_{qi}Q_i + \Delta V_i \quad (5.1b)$$

where ω^{set} and V^{set} are universal set-points for frequency and voltage (in this simple representation they are in per-unit), respectively, and $\Delta\omega_i$ and ΔV_i are secondary compensation signals. To restore the set-point deviations caused by the negative product terms, a naive solution can be first investigated by introducing the integral control implemented locally by individual units:

$$\Delta\omega_i = \int(\omega^{set} - \omega_i)dt \quad (5.2a)$$

$$\Delta V_i = \int(V^{set} - V_i)dt \quad (5.2b)$$

Assuming that the system is stable, the terms inside the bracket of the integral form become all zeros: $\omega_1 = \omega_2 = \dots = \omega_i = \omega^{set}, \quad \forall i \in \{1\dots N\}$ and $V_1 = V_2 = \dots =$

$V_i = V^{set}, \quad \forall i \in \{1 \dots N\}$, where N denotes the number of participants. In fact, a practical system has essentially many non-ideal factors, as mentioned in Section 1.2, including reference and calibration errors. Therefore, a practical setup should model such non-ideal factors so that the equations (5.2a) and (5.2b) become:

$$\Delta\omega_i = \int (\omega^{set} - \omega_i - \epsilon_{\omega i}) dt \quad (5.3a)$$

$$\Delta V_i = \int (V^{set} - V_i - \epsilon_{V i}) dt \quad (5.3b)$$

where $\epsilon_{\omega i}$ and $\epsilon_{V i}$ denote the reference errors for frequency and voltage, respectively. Considering only the frequency droop and assuming the steady-state frequency being ω^{ss} , (5.3a) becomes:

$$\Delta\omega_i = \int (\omega^{set} - \omega^{ss} - \epsilon_{\omega i}) dt \quad (5.4)$$

where it can be noticed that the terms, $\omega^{set} - \omega^{ss}$, are in fact the same for all the inverters; this means that it is impossible for all the terms inside the integral form to become zero since $\epsilon_{\omega i}$ is different across units. That is, the system has no solution and the assumption is violated. This type of control actually causes the same problem without droop control since all the units compete against each others and result in circulating power or instability. Thus, a better control scheme should be investigated.

5.2.2 Average Secondary Compensation

A more ideal way is to utilize communication channels for secondary compensation. Since droop control can achieve power sharing of high-bandwidth, the communication speed does not require high bandwidth as the main goal is to restore the set-points by slowly adjusting offsets to compensate the droop terms. Instead of using the local measured frequency and voltage, an improved method utilizes the average measure-

ment from all units (similar to the DC case proposed in [47]):

$$\Delta\omega_i = \int(\omega^{set} - \omega^{avg})dt \quad (5.5a)$$

$$\Delta V_i = \int(V^{set} - V^{avg})dt \quad (5.5b)$$

where

$$\omega^{avg} = \sum_{i=1}^N \frac{\omega_i + \epsilon_{\omega i}}{N}, \quad V^{avg} = \sum_{i=1}^N \frac{V_i + \epsilon_{V i}}{N}. \quad (5.6)$$

Now assume that there exists an universal steady-state frequency, $\omega_i = \omega^{ss} \quad \forall i \in \{1 \dots N\}$, (5.5a) becomes (after the substitution using (5.6)):

$$\Delta\omega_i = \int(\omega^{set} - \omega^{ss} - \epsilon_{\omega}^{avg})dt \quad (5.7)$$

where

$$\epsilon_{\omega}^{avg} = \sum_{i=1}^N \frac{\epsilon_{\omega i}}{N} \quad (5.8)$$

Since (5.7) is the same for all the units as all the terms inside the bracket are identical, the solution exists and the steady-state frequency becomes:

$$\omega^{ss} = \omega^{set} - \epsilon_{\omega}^{avg} \quad (5.9)$$

where ϵ_{ω}^{avg} is fairly small and should not affect the restoration performance. The idea of this average compensation is similar to the common/differential-mode concept; the competition is resulted from differential modes (error difference) and using a common-mode signal for compensation avoids such competition. The above derivation can be trivially extended to the voltage compensation, and the steady-state voltage becomes:

$$V^{ss} = V^{set} - \epsilon_V^{avg} \quad (5.10)$$

where ϵ_V^{avg} denotes the average voltage reference errors.

5.3 Power Dispatch via Secondary Compensation

As mentioned in Section 1.2 the coupling between frequency to active power and voltage to reactive power essentially leads to the design of droop control that allows power sharing. Similarly, it is also possible to utilize the concept to control power flows, or equivalently power dispatch. Therefore, a modified form in equations (5.5a) and (5.5b) can be used to allow such a capability:

$$\Delta\omega_i = \int (P_i^* - P_i) dt \quad (5.11a)$$

$$\Delta V_i = \int (Q_i^* - Q_i) dt \quad (5.11b)$$

where P_i^* and Q_i^* are the active and reactive power references, and P_i and Q_i are the active and reactive power measurement. In fact, this power dispatch capability can be directly integrated with the set-point compensation (similar to the DC case proposed in [41]):

$$\Delta\omega_i = \int \{k_f(\omega^{set} - \omega^{avg}) + \gamma_p(P_i^* - P_i)\} dt \quad (5.12a)$$

$$\Delta V_i = \int \{k_v(V^{set} - V^{avg}) + \gamma_q(Q_i^* - Q_i)\} dt \quad (5.12b)$$

where $k_f, k_v, \gamma_p, \gamma_q$ are compensation gains and they can be tuned independently to allow different compensation speeds. To be more specific, the overall procedure is as follows:

1. The local control units send the local measure signals, ω_i , V_i , P_i , and Q_i , to the central control unit (It is more beneficial to send the output capacitor voltage magnitude, V_{ci}).
2. The central control unit computes the average voltage and frequency, ω^{avg} and V^{avg} ; the power references are also computed through assigning the dispatch ratios, d_i^p and d_i^q :

$$P_i^* = d_i^p P^{total}, \quad Q_i^* = d_i^q Q^{total} \quad (5.13)$$

where

$$P^{total} = \sum_{i=1}^N P_i, \quad Q^{total} = \sum_{i=1}^N Q_i \quad (5.14)$$

and

$$\sum_{i=1}^N d_i^p = 1, \quad \sum_{i=1}^N d_i^q = 1 \quad (5.15)$$

It should be noticed that the dispatch ratios can become negative unlike the sharing ratios, s_i (since an inherent positive feedback loop may occur when using negative droop gains).

3. After receiving the commands from the central control unit, the local control units enforce the control rule stated in equations(5.12b) and (5.11b).

The secondary controller, in fact, overrides droop control in terms of the power sharing. Particularly, it allows a more flexible choice of the dispatch ratios as compared to the sharing ratios for droop control. More importantly, the issue of non-ideal reactive power sharing can be easily resolved thanks to the integral control employed by the secondary controller. This offers great flexibility of energy management and efficiency optimization while maintaining high reliability against failures (such overriding power only exists when secondary control is enabled).

5.4 Conclusions

Cost-effective communication along with secondary compensation enables great flexibility for optimizing the operation efficiency of microgrids. It had been shown that the compensation scheme allows effective restoration of set-point deviations caused by droop control and precise dispatch of active and reactive power. The separation of the primary and secondary control layers further enhances operation reliability such that communication failure does not cause loss of load.

Chapter 6

Validation

6.1 Introduction

In this chapter, the simulation models with detailed implementation of control loops in MATLAB/Simulink along with a miniature experimental prototype are used to verify the effectiveness of the proposed approach. For computing the stability region of the Simulink model, *linmod* and *trim* functions in Matlab are used to extract the linearized transition matrix and eigenvalues. In addition, the experimental prototype was tested by using commercial inverters, self-designed filter boards, and the control boards with microcontrollers. Also, the constant power load is also considered by using the commercial PFC power supplies along with transformers for voltage adjustment since the base power and voltage are both scaled down for conceptual validation. Both the simulation and experiment shares the same base impedance and therefore the parameters are intended to be identical in *pu* system. The system configuration is shown in Figure 6-1 with the basic settings and parameters described in Table 6.1. The details of the simulation models and experiment can be found in the Appendixes.

6.2 Stability Region

In Figure 6-2, the case considers that the sharing ratios: $s_1 : s_2 : s_3 = 1 : 0.67 : 0.33$ and the load types (pu): $1.0 + j0.0$ (resistive load), $0.4 + j0.71$ (inductive and resis-

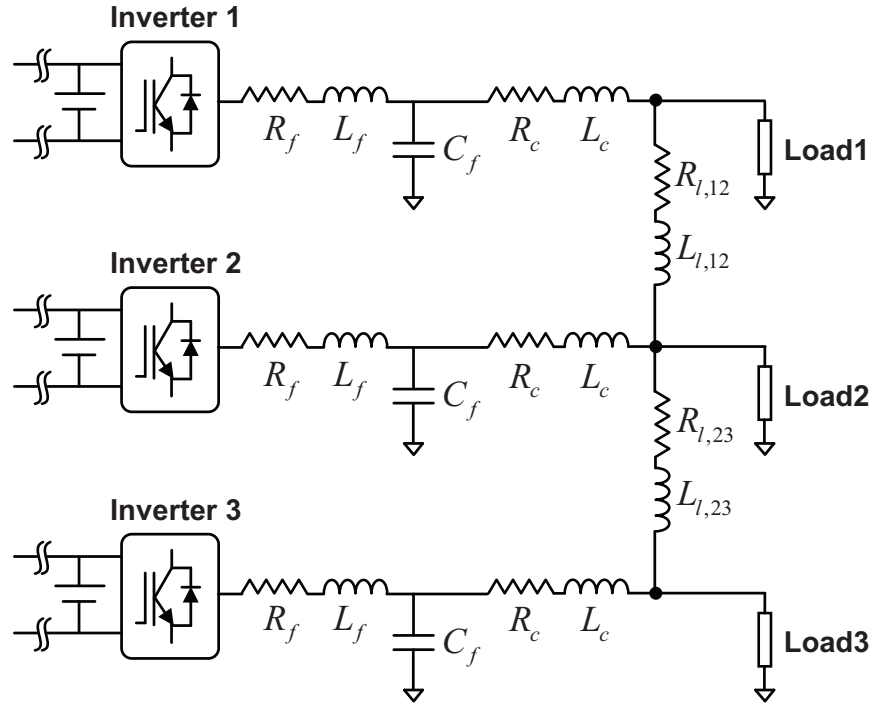


Figure 6-1: Three-inverter test system.

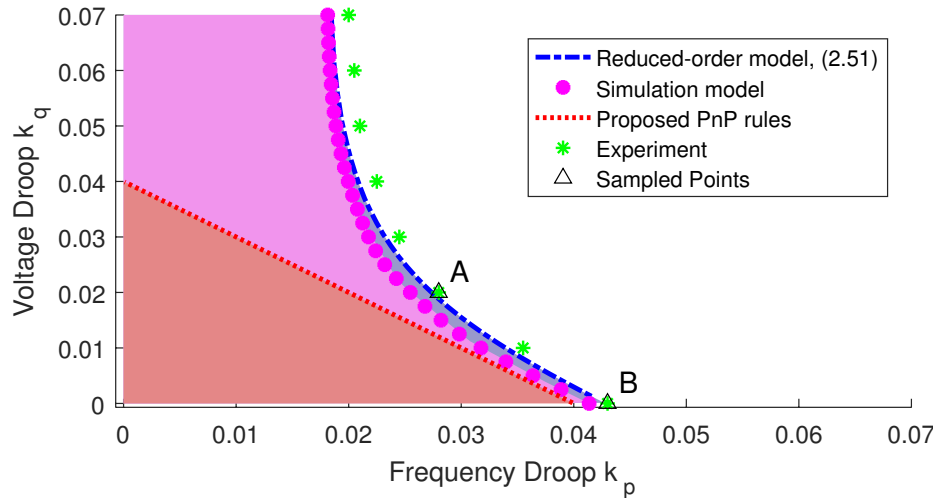


Figure 6-2: Comparison of projected stability regions: $k_{p,i} = k_p/s_i$, $k_{q,i} = k_q/s_i$, $X_{mc,i} = R_{mc,i} = 2/s_i\%$.

tive load), $0.57 + j0.0$ (constant active power load) for loads 1, 2 and 3, respectively. The projected stability region with respect to the common droop bases k_p and k_q are shown, with the individual droop gains and controlled impedance scaled according to their sharing ratios ($k_{p,i} = k_p/s_i$, $k_{q,i} = k_q/s_i$, $X_{mc,i} = R_{mc,i} = 2/s_i\%$). It should be

Table 6.1: Parameters of Three Inverter Test System

Parameter	Description	Value
V_b	Base Voltage (simulation)	381 V
S_b	Base Power (simulation)	5 kVA
V_b	Base Voltage (prototype)	71 V
S_b	Base Power (prototype)	174 VA
Z_b	Base Impedance	29Ω
ω_0	Nominal Frequency	$2\pi \times 50 \text{ rad/s}$
w_c	Frequency Filter Constant	$2\pi \times 5 \text{ rad/s}$
f_{sw}	Switching Frequency	10 kHz
f_{com}	Communication Frequency	10 Hz
σ_i	voltage feed-forward gain	1
σ_v	current feed-forward gain	0.5
L_c	Coupling Inductance	0.35 mH
R_c	Coupling Resistance	80 mΩ
L_f	Filter Inductance	1 mH
C_f	Filter Capacitance	30 μF
R_{vd}	Virtual Damping Resistance	5 ohm
C_{vd}	Virtual Damping Capacitance	0.25 mF
k_{pc}, k_{ic}	Current Loop PI Gains	8, 18 000
L_l	Line Inductance	0.26 mH km^{-1}
R_l	Line Resistance	$165 \text{ m}\Omega \text{ km}^{-1}$
l_{12}	Line Length (Bus 1 to 2)	0.6 km
l_{23}	Line Length (Bus 2 to 3)	3.25 km

emphasized that the proportional scaling of the droop gains and virtual impedances are just for plotting convenience according to (4.20) and one may choose any values within the upper bounds of the droop gains (lower bounds of the virtual impedances when fixing droop gains, vice versa). The results show that the predicted boundaries between the reduced-order model, detailed simulation model, and experiment coincide closely with very small deviations. In fact, it should be emphasized that the reduced-order model does not consider load participation and can still generate accurate predictions. Moreover, the effect of critical link is verified by plotting the stability region with respect to the active power droop gains of Inverter 1 and Inverter 2, shown in Figure 6-3. In this case, other parameters are fixed as described in the caption with the only variables being k_{p1} and k_{p2} . Similarly, the predicted boundaries

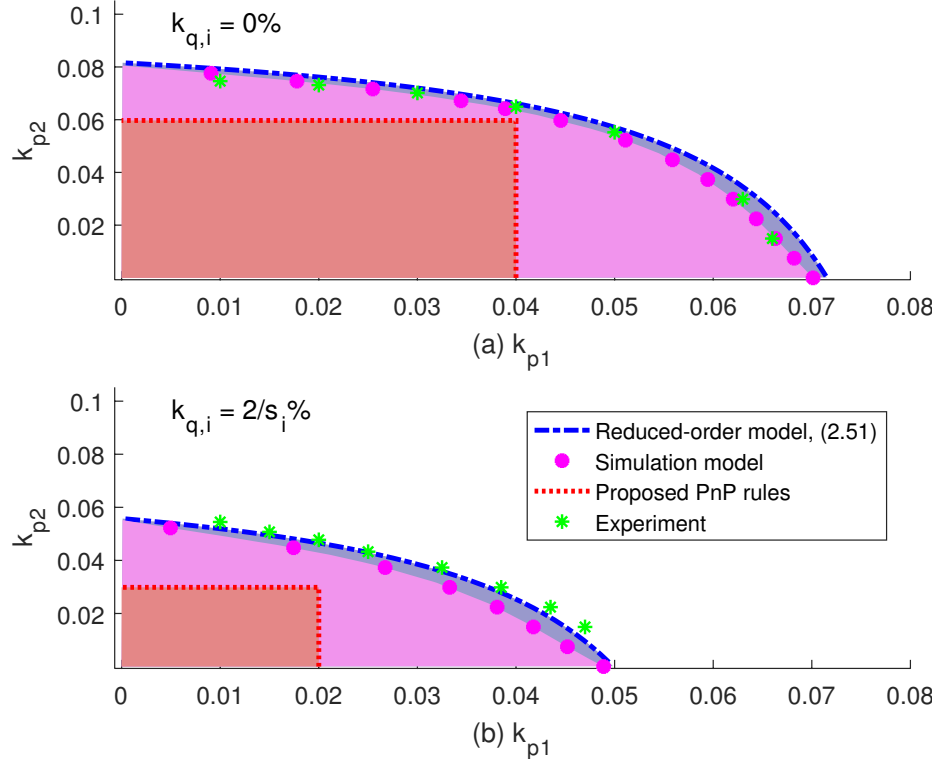


Figure 6-3: Comparison of projected stability regions with respect to k_{p1} and k_{p2} :
 $s_1 : s_2 : s_3 = 1 : 0.67 : 0.33$, $X_{mc,i} = R_{mc,i} = 2/s_i\%$; (a) $k_{q,i} = 0$, $k_{p3} = 12.12\%$; (b) $k_{q,i} = 2/s_i\%$, $k_{p3} = 6.06\%$.

are very close among all models, verifying the investigation in Chapter 4.

The above results validate that: (1) load participation under small virtual impedance is limited; (2) the projected stability region is constrained by the short link between bus 1 and bus 2; (3) the reduced-order model achieves high prediction accuracy; (4) the proposed PnP control rule demonstrates conservativeness when k_q increases (Figure 6-3(b)).

6.3 Time-domain Analysis

6.3.1 Droop Control

In addition to the validation of the stability regions, the time-domain analysis is carried out based on both experiment and simulation. Particularly, relatively large droop gains are chosen to show that the virtual impedance method can effectively

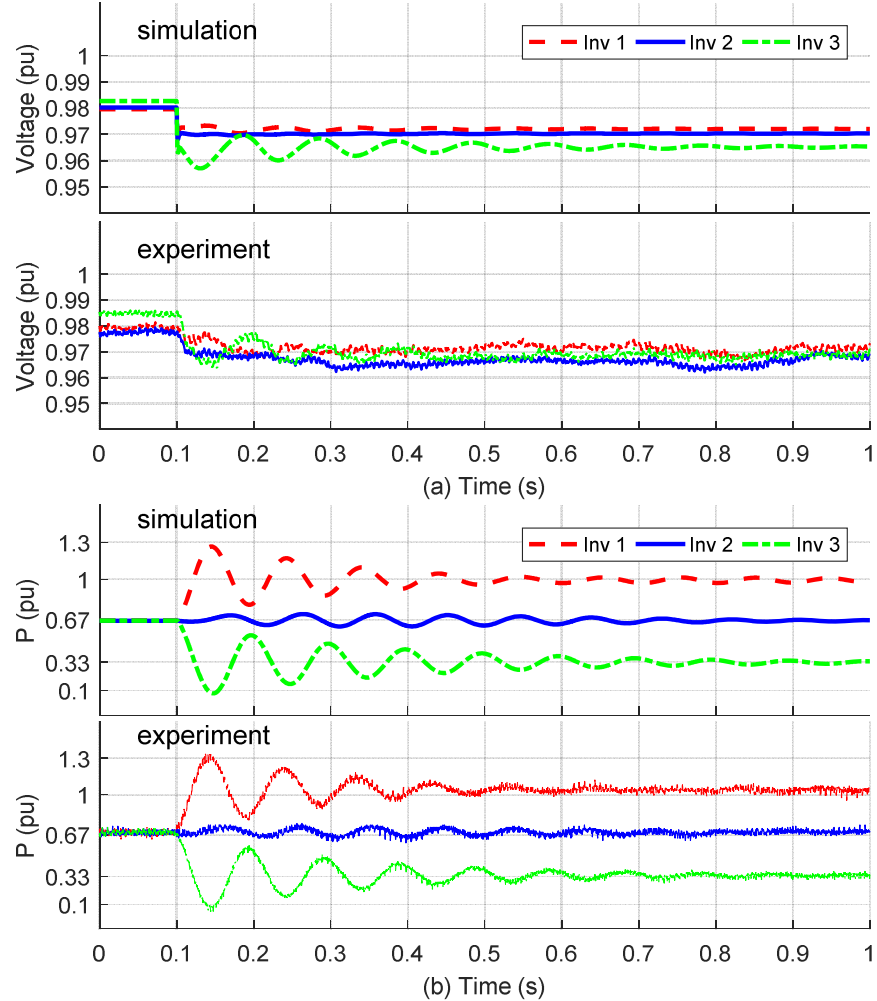


Figure 6-4: Time-domain results for a step change of sharing ratios, s_i , from 1 : 1 : 1 to 1 : 0.67 : 0.33: $k_{p,i} = k_{q,i} = 2/s_i\%$, $X_{mc,i} = R_{mc,i} = 2/s_i\%$; (a) Output voltages; (b) Filtered active power.

damp the droop oscillations. Under the same loading condition as shown in the previous subsection, the system dynamical responses after a step change of sharing ratios from 1 : 1 : 1 to 1 : 0.67 : 0.33 are shown in Figure 6-4 and 6-5. In this case, both droop gains and virtual impedances are of a step change at 0.1s - $k_{p,i} = k_{q,i} = 2/s_i\%$ and $X_{mc,i} = R_{mc,i} = 2/s_i\%/\%$. It can be seen that active and reactive power sharing changes according to the sharing ratios; the oscillation is damped due to the conservative nature of the proposed PnP rule; the voltage and frequency drop due to the overall increase of the virtual impedances and droop gains; the dynamic responses

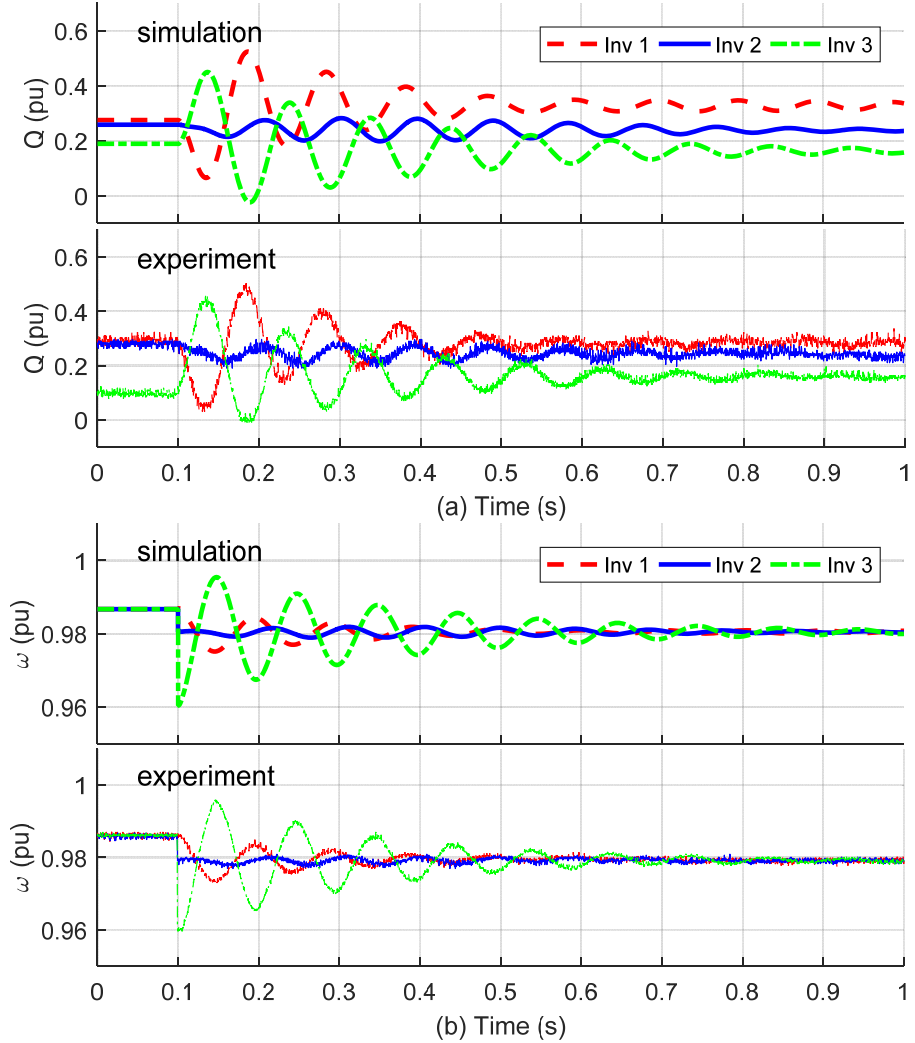


Figure 6-5: Time-domain results for a step change of sharing ratios, s_i , from 1 : 1 : 1 to 1 : 0.67 : 0.33: (a) Filtered reactive power; (b) Frequency.

between the simulation and experiment match closely despite some DC deviations due to calibration errors and un-modeled component tolerances.

Figure 6-6 shows the oscillations around two sampled critically stable operating conditions (Sampled points, A and B, in Figure 6-2, difference of the critical droop gains between the simulation and experiment is $\sim 0.1\%$). It can be seen that choosing higher active power droop gains result in higher frequencies of oscillations. Also, the critical link between inverters 1 and 2 leads to a dominant magnitude of oscillation between them as compared to inverter 3.

In Figure 6-7, voltage responses for a sudden resistive load stepping of 2 pu based

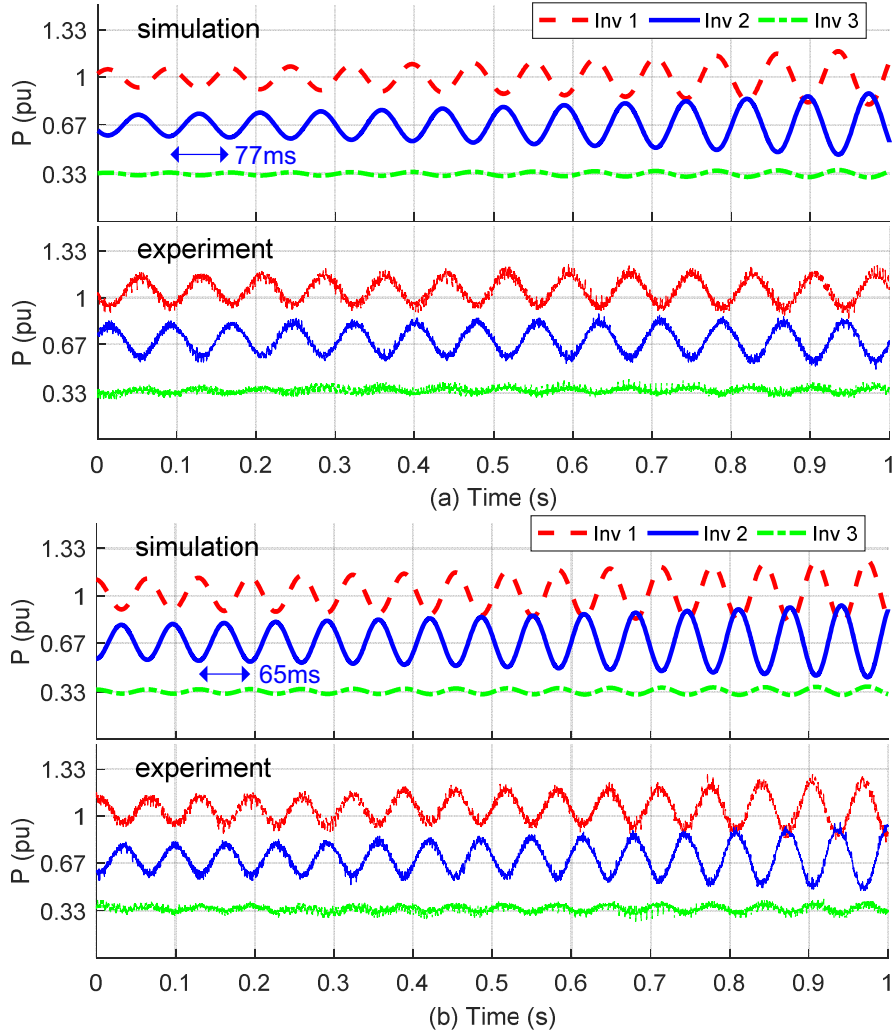


Figure 6-6: Droop oscillations beyond critically stable conditions: sharing ratios 1 : 0.67 : 0.33, $X_{mc,i} = R_{mc,i} = 2/s_i\%$; (a) $k_{p,i} = \sim 2.8/s_i\%$, $k_{q,i} = 2/s_i\%$; (b) $k_{p,i} = \sim 4.3/s_i\%$, $k_{q,i} = 0/s_i\%$.

on different values of controlled impedances are demonstrated. Similarly, discrepancies between the simulation and experiment can be observed due to measurement noises, calibration errors, and un-modeled digital delays. In general, the transient voltage dips for few hundred microseconds in simulation are around 0.88 to 0.94 pu (0.85 to 0.93 pu for experiment) and are not sensitive to the controlled impedance since it is mainly affected by the internal control, network characteristics, and types and locations of the load. In steady state, it can be seen that the voltage variations are proportional to the value of controlled impedance as expected. The filtered active

power responses for the same test is shown in Figure 6-8. The responses are almost identical regardless of the discrepancies of voltage responses due to larger filtering time constants.

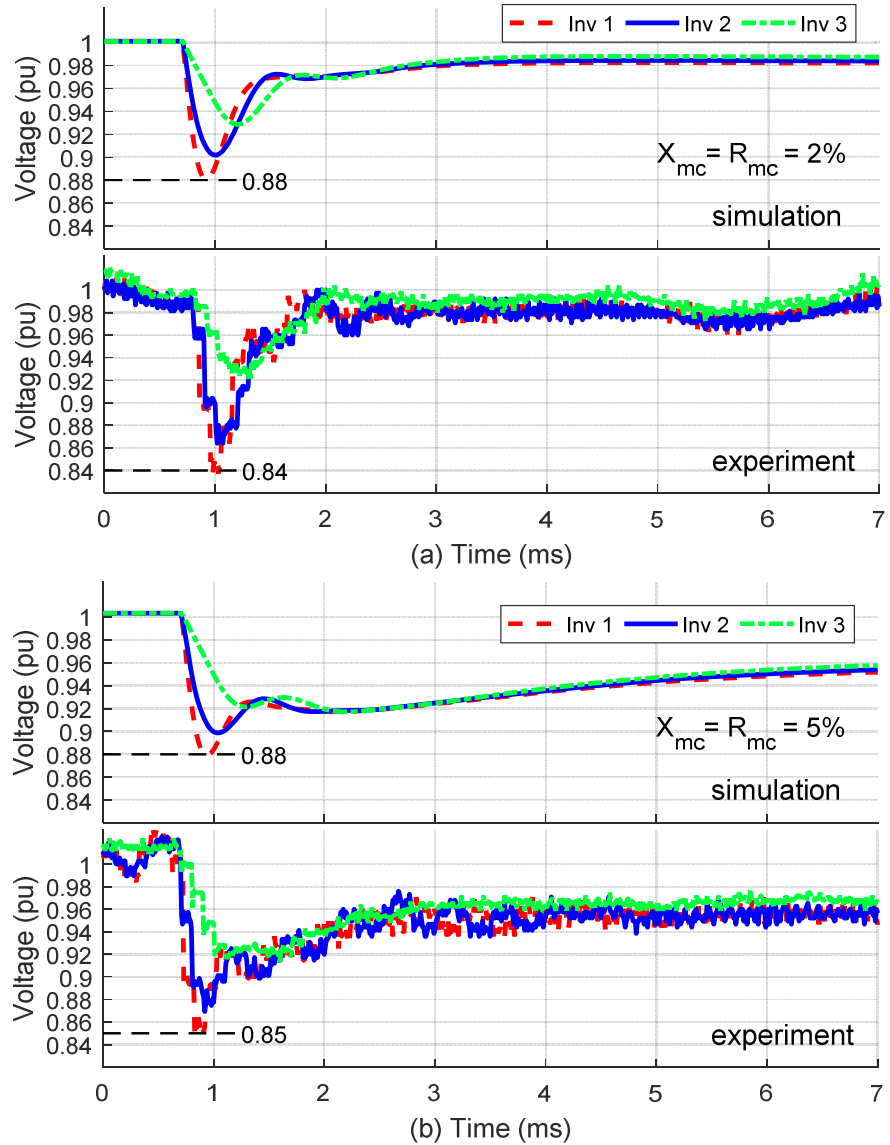


Figure 6-7: Dynamic responses of output voltages during load stepping: sharing ratios $1 : 0.67 : 0.33$, $k_{p,i} = 2/s_i\%$, $k_{q,i} = 2/s_i\%$; (a) $X_{mc,i} = R_{mc,i} = 2/s_i\%$; (b) $X_{mc,i} = R_{mc,i} = 5/s_i\%$.

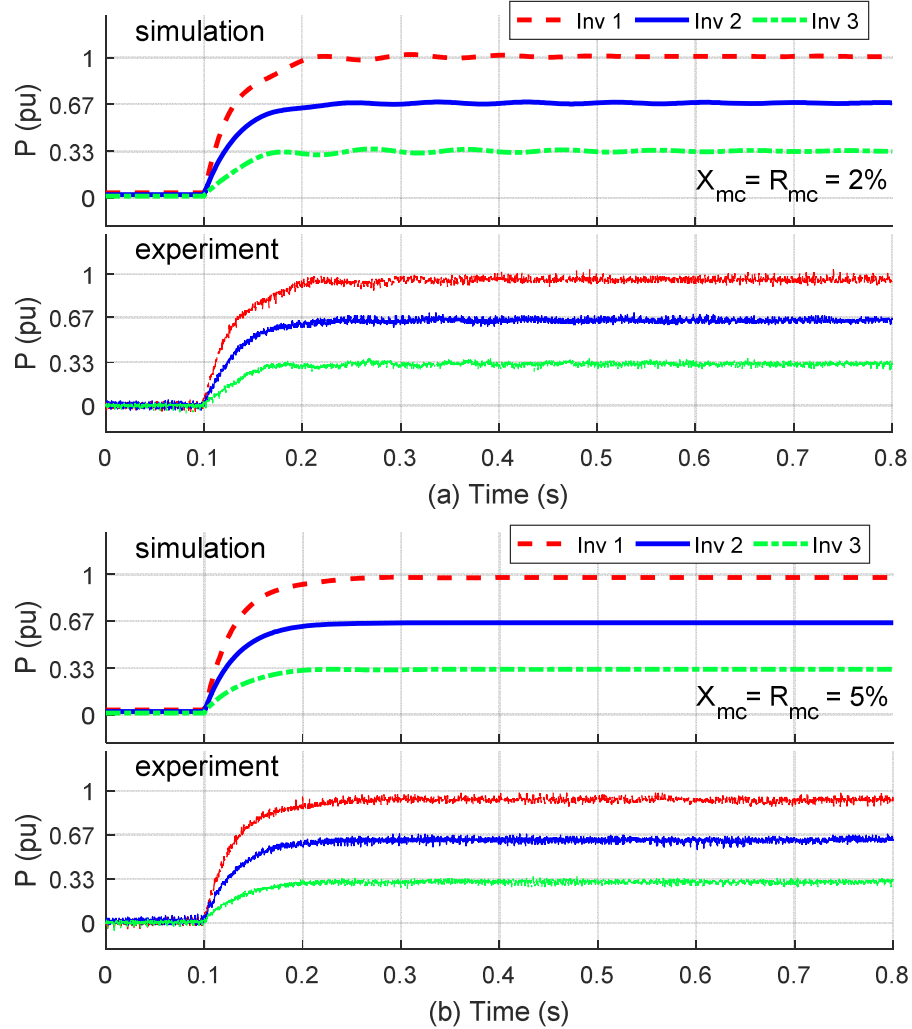


Figure 6-8: Dynamic responses of filtered active power during load stepping: sharing ratios $1 : 0.67 : 0.33$, $k_{p,i} = 2/s_i\%$; $k_{q,i} = 2/s_i\%$; (a) $X_{mc,i} = R_{mc,i} = 2/s_i\%$; (b) $X_{mc,i} = R_{mc,i} = 5/s_i\%$.

6.3.2 Secondary Compensation

To validate the developed secondary compensation scheme for restoring set-points and dispatching active and reactive power, a time-domain case is built by testing the dynamical responses after enabling the control scheme. In this case, the sharing ratios for the droop control are chosen as $s_i = 1 : 1 : 1$ while both the active and reactive power dispatch ratios, d_i^p and d_i^q , are set as $0.5 : 0.333 : 0.167$. In addition, the droop gains and controlled impedance are both set to be relatively large to exaggerate the

effect of set-point deviation ($k_p = k_q = 4\%$ and $R_{mc} = X_{mc} = 5\%$). In this case, the communication speed is of 10Hz. The dynamic responses are shown in Figure 6-9 and 6-10. It can be seen that the voltage and frequency are both restored to the nominal value after the activation of the secondary compensation; also, the power dispatch ratios override the sharing ratios dictated by the droop control. Particularly, the reactive power dispatch can achieve very high accuracy as compared to the droop control, indicating the effectiveness of using low-bandwidth communication.

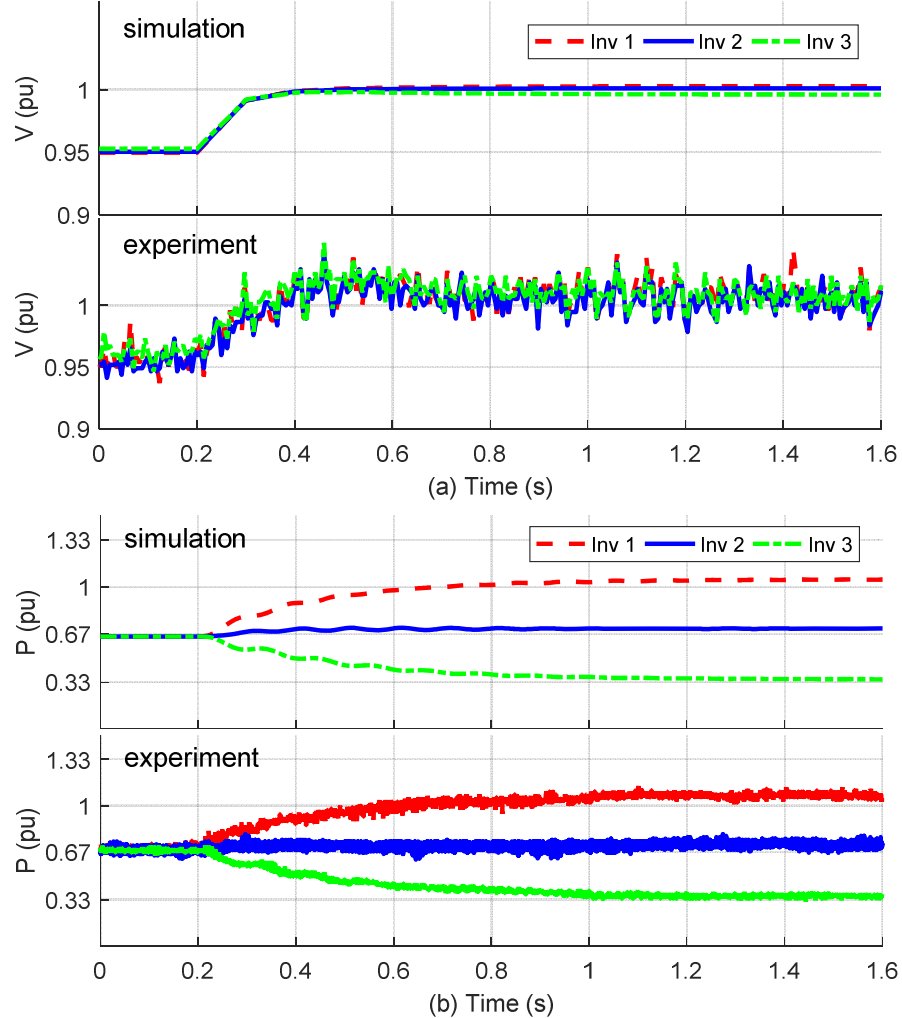


Figure 6-9: Time-domain results for the activation of the secondary compensation: $k_{p,i} = k_{q,i} = 4/s_i\%$, $X_{mc,i} = R_{mc,i} = 5/s_i\%$; (a) Output voltages; (b) Filtered active power.

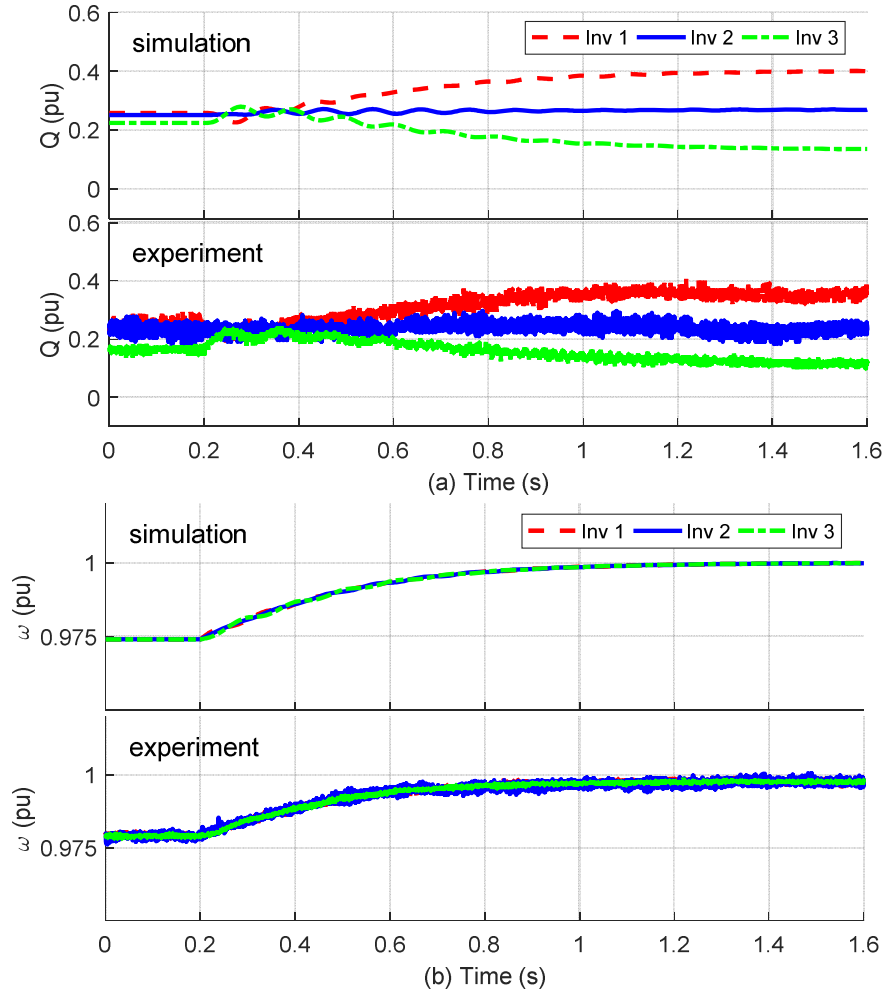


Figure 6-10: Time-domain results for the activation of the secondary compensation: $k_{p,i} = k_{q,i} = 4/s_i\%$, $X_{mc,i} = R_{mc,i} = 5/s_i\%$; (a) Filtered reactive power; (b) frequency.

6.4 Conclusions

The results based on the detailed simulation models and experimental set-up effectively validate the high-fidelity reduced-order model and the proposed PnP control rules. The efficacy of the proposed virtual impedance method against the droop instability was demonstrated; the performance of the secondary compensation can be also seen in optimizing the operation efficiency based on a practical setting of the microgrids. Despite the calibration errors and un-modeled dynamics, the discrepancies of the dynamic performance between the simulation and experiment are very little, justifying the systematic control strategy proposed in the thesis.

Chapter 7

Conclusions and Future Work

7.1 Conclusions

The specific nature of inverter-based microgrids where line impedances are relatively small and X/R ratios are around unity leads to instability when operating in droop-controlled modes. The instability is mainly caused by electro-magnetic delays in lines and become significant with reduction in network size. Such a mechanism was investigated in Chapter 2 based on the high-fidelity reduced-order model for a simple two-bus case. The generalization was then taken to extend the model to arbitrary networks.

In order to derive a more intuitive stability conditions, Chapter 3 began by constructing Lyapunov function candidates to allow the development of stability certificates for two-bus and network cases. It was then revealed that the stability conditions for the network case are complicated for practical usages. Thus, Chapter 4 explored an interesting property based on the two-bus case study. It was found that the freedom of choosing controlled impedance can facilitate the development of the concise plug-and-play stability rules. The integration of new inverters into the network become flexible with the only need to satisfy a set of local rules. Also, virtual impedance control was investigated in details in consideration of various aspects including droop stability, internal stability, and voltage deviations.

Chapter 5 developed a comprehensive secondary compensation scheme by using

low-bandwidth communication. The optimization of the microgrid operation can then be easily taken without compromising system stability. Chapter 6 validated all the analytical and numerical findings through detailed models in both MATLAB/Simulink and experiment.

To sum up, the investigation of the reduced-order models in this work presented many great insights into the physical origin of droop instability such that the design principles for small-scale microgrids were well revealed. The simple and concise Plug-and-Play control rules further provide a convenient way for sizing virtual impedance. Moreover, the developed secondary compensation scheme eases the design complexity for high-level power and energy management schemes. The overall systematic control strategy offers practical and useful guidelines for realistic microgrid design and operations.

7.2 Future Work

There are many interesting aspects which are not discussed in the thesis. For the modeling of the microgrids, the framework, in fact, can be further extended to consider different types of sources and loads including current-source inverters, machines, and non-linear loads. To consider these components, the preservation of concise model representation becomes critical for generalization. Detailed investigation is expected to understand the participation of different sources/loads into droop stability. Particularly, for the hybrid microgrids with both inverters and synchronous machines, it is very interesting to see the influence of the machines on droop stability.

As mentioned in Chapter 3, the simplification of the network stability criteria is not a straight-forward procedure due to a set of matrix inequalities. Therefore, an alternative method might be more beneficial in dealing with the network case. This may require a significant modification/revision of the proposed framework to facilitate the development.

In Chapter 4, a few interesting ideas could also be developed. Since the lines are typically short in microgrids, the proposed PnP rules preserve competitive perfor-

mance. However, for the mid-scale microgrids, the development of a less conservative rule could be greatly appreciated. The emulation of the line though the controlled impedance by choosing the same X/R ratio could make the stability certificate less conservative. Moreover, a more flexible design (without fixing the X/R ratios of the controlled impedances) may be interesting for applications in which voltage deviations are critical. That is, a high X/R ratio may be more favorable when reactive power consumption is low.

In Chapter 5, the developed secondary control scheme enables a great potential for high-level energy and power management. The optimization for the economic and efficient microgrid operation is a very interesting topic for the future work based on the developed framework. Also, it is expected that the development of highly distributed secondary control schemes could become essential for enhancing reliability, resiliency, and security of future grids. Finally, a full-scale experimental prototype is indeed appreciated to provide more realistic validations.

Appendix A

Derivations and Notes

A.1 Generalized Stability Criteria for Networks

In Section 3.3, system stability is certified using the Lasalle's Invariance Principle [36], meaning that the conditions are derived by demanding $\mathbf{P} > \mathbf{0}$ and $\mathbf{Q} \geq \mathbf{0}$. However, it becomes not obvious to analyze the condition $\mathbf{P} > \mathbf{0}$ (strictly greater) since \mathbf{G} , \mathbf{B} , and \mathbf{G}' are all singular due to negligence of shunt admittances. In fact, a modified form can assist in certifying the positive-definiteness of \mathbf{P} . By choosing $\mathbf{y} = [\boldsymbol{\vartheta}, \boldsymbol{\rho}, \boldsymbol{\vartheta} + c\tau\boldsymbol{\vartheta}]^T$, the corresponding \mathbf{P} becomes [48]¹:

$$\mathbf{P} = \begin{bmatrix} \frac{c-1}{c}\Lambda_{\mathbf{p}} + c\tau\mathbf{B} - \mathbf{B}' & c\tau\mathbf{G} + \mathbf{G}' & 0 \\ c\tau\mathbf{G} + \mathbf{G}' & (c+1)\tau\Lambda_{\mathbf{q}} + c\tau\mathbf{B} - \mathbf{B}' & 0 \\ 0 & 0 & \frac{1}{c}\Lambda_{\mathbf{p}} \end{bmatrix} \quad (\text{A.1})$$

The condition for $\mathbf{P} > \mathbf{0}$ is given as (assuming that $c > 1$, $\mathbf{G}' \ll \tau\mathbf{G}$, and $\mathbf{B}' \ll \tau\mathbf{B}$):

$$\frac{1}{c}\Lambda_{\mathbf{p}} > \mathbf{0} \quad (\text{A.2a})$$

$$\frac{c-1}{c}\Lambda_{\mathbf{p}} + c\tau\mathbf{B} > \mathbf{0} \quad (\text{A.2b})$$

$$\frac{(c+1)}{c}\Lambda_{\mathbf{q}} + \mathbf{B} - \mathbf{G}\left(\frac{c-1}{c^2}\Lambda_{\mathbf{p}} + \mathbf{B}\right)^{-1}\mathbf{G} > \mathbf{0} \quad (\text{A.2c})$$

¹Great appreciation to Prof. Petr Vorobev (first author), Prof. Mohamed Al Hosani, Prof. James Kirtley, and Prof. Konstantin Turitsyn for their contributions and efforts.

where conditions (A.2a) and (A.2b) are automatically satisfied with positive droop gains and (A.2c) can be satisfied (cumbersome but straightforward derivations are required) as long as \mathbf{Q} in (3.14) is positive semi-definite. Therefore, the conditions for $\mathbf{P} > \mathbf{0}$ do not add additional constraints beyond (3.15).

A.2 Two-Loop Control

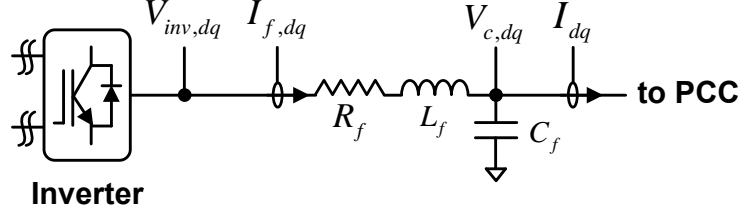


Figure A-1: Circuit diagram of the inverter system.

Normally the current controller is developed based on considering the resistance and inductance of the inductor filter, R_f , L_f , as shown in Figure A-1. To regulate the inductor current, one can derive the dynamic equations in dq reference frames:

$$sL_f I_{f,d} = V_{inv,d} - V_{c,d} - R_f I_{f,d} + \omega L_f I_{f,q} \quad (\text{A.3a})$$

$$sL_f I_{f,q} = V_{inv,q} - V_{c,q} - R_f I_{f,q} - \omega L_f I_{f,d} \quad (\text{A.3b})$$

where $s = d/dt$ is the Laplace operator and $V_{inv,d}$ and $V_{inv,q}$ are the inverter voltages. Considering that the inverter voltages are fully controllable (through PWM switching), $V_{c,dq}$ and $I_{f,dq}$ can be measured, and R_f and L_f are known parameters, the inverter voltages can be generated through:

$$V_{inv,d} = u_{i,d} + V_{c,d} + R_f I_{f,d} - \omega L_f I_{f,q} \quad (\text{A.4a})$$

$$V_{inv,q} = u_{i,q} + V_{c,q} + R_f I_{f,q} + \omega L_f I_{f,d} \quad (\text{A.4b})$$

where $u_{i,d}$ and $u_{i,q}$ denote some temporary input variables. It can be seen that in (A.4), the last three terms on the right-hand side have opposite signs as compared

to the last three terms in (A.3). That is, the purpose of introducing these terms is to cancel the effect of the known disturbances of the capacitor voltage and cross-coupling terms. This technique is commonly referred as feed-forward compensation and is widely used in dq control. Substituting (A.4) into (A.3), one can obtain:

$$sL_f I_{f,d} = u_{i,d} \quad (\text{A.5a})$$

$$sL_f I_{f,q} = u_{i,q} \quad (\text{A.5b})$$

Equivalently, the above equations can be represented using the following transfer functions from $u_{i,dq}$ to $I_{f,dq}$:

$$G_{i,d}(s) = \frac{I_{f,d}}{u_{i,d}} = \frac{1}{sL_f} \quad (\text{A.6a})$$

$$G_{i,q}(s) = \frac{I_{f,q}}{u_{i,q}} = \frac{1}{sL_f} \quad (\text{A.6b})$$

It can be seen that the system now has two independent first-order transfer functions. Thus, to regulate the dq currents, PI controllers can be used:

$$u_{i,d} = (k_{pc} + \frac{k_{ic}}{s})(I_{f,d}^* - I_{f,d}) \quad (\text{A.7a})$$

$$u_{i,q} = (k_{pc} + \frac{k_{ic}}{s})(I_{f,q}^* - I_{f,q}) \quad (\text{A.7b})$$

where k_{pc} and k_{ic} are the proportional and integral gains, respectively, and $I_{f,d}^*$ and $I_{f,q}^*$ are the desired current references. After substituting (A.7) into (A.6), the closed-loop transfer functions from $I_{f,dq}^*$ to $I_{f,dq}$ become:

$$C_{i,d}(s) = \frac{I_{f,d}}{I_{f,d}^*} = \frac{k_{ic}}{L_f s^2 + k_{pc}s + k_{ic}} \quad (\text{A.8a})$$

$$C_{i,q}(s) = \frac{I_{f,q}}{I_{f,q}^*} = \frac{k_{ic}}{L_f s^2 + k_{pc}s + k_{ic}} \quad (\text{A.8b})$$

Now the current regulation follows the above two second-order systems, so by tuning k_{pc} and k_{ic} one can achieve desired dynamic responses. In general, the current loops are very fast at around one-tenth the switching frequency; thus, they can be assumed

ideal for designing the voltage control. Similarly, the dynamic equations of the filter capacitors in dq reference frames can be described as:

$$sC_f V_{c,d} = I_{f,d}^* - I_d + \omega C_f V_{c,q} \quad (\text{A.9a})$$

$$sC_f V_{c,q} = I_{f,q}^* - I_q - \omega C_f V_{c,d} \quad (\text{A.9b})$$

where the $I_{f,dq}$ are replaced by $I_{f,dq}^*$ by assuming ideal current controllers. Thus, similar to (A.4), the following current references can be generated:

$$I_{f,d}^* = u_{v,d} + \sigma_v I_d - \omega C_f V_{c,q} \quad (\text{A.10a})$$

$$I_{f,q}^* = u_{v,q} + \sigma_v I_q + \omega C_f V_{c,d} \quad (\text{A.10b})$$

where $u_{v,d}$ and $u_{v,q}$ denote some temporary input variables and σ_v is the coefficient for feed-forward compensation. Ideally, σ_v should be one to cancel the output current; however, in practice using an unity σ_v will result in oscillation due to its positive feedback nature (also the delays and phase shits induced from realistic current controllers). Therefore, perfect disturbance rejection is not feasible such that the voltage control design becomes more complicated. However, in general, tuning of voltage control responses still follows the transfer functions shown as below (approximation):

$$C_{v,d}(s) = \frac{V_{c,d}}{V_{c,d}^*} = \frac{k_{iv}}{C_f s^2 + k_{pv}s + k_{iv}} \quad (\text{A.11a})$$

$$C_{v,q}(s) = \frac{V_{c,q}}{V_{c,q}^*} = \frac{k_{iv}}{C_f s^2 + k_{pv}s + k_{iv}} \quad (\text{A.11b})$$

where k_{pv} and k_{iv} are the PI gains of the voltage controllers.

Appendix B

Microgrid Validation

The proposed framework and control strategies were tested based on both simulation models and an experimental prototype. The details are disclosed in this appendix.

B.1 Detailed Average Simulation Models

B.1.1 Realization of ODEs

In this thesis, the detailed simulation models were first constructed to validate the high-fidelity reduced-order models. Both two-bus and network cases were established using MATLAB Simulink. To study the system stability, it is important to build all the components using the Simulink *Continuous* toolbox for small-signal analysis. In this case, the Pulse Width Modulation (PWM) signals are averaged over one switching cycle and such models are generally referred as average models. Now, to model the dynamic equations of the droop control in equations (2.16)-(2.18), a Simulink model can be built as shown in Figure B-1. In the figure, the *Integrator* modules from the toolbox are used with their input implementing the right-hand side of the ODEs. Similarly, the dynamic equations of controllers and networks can follow the same principle.

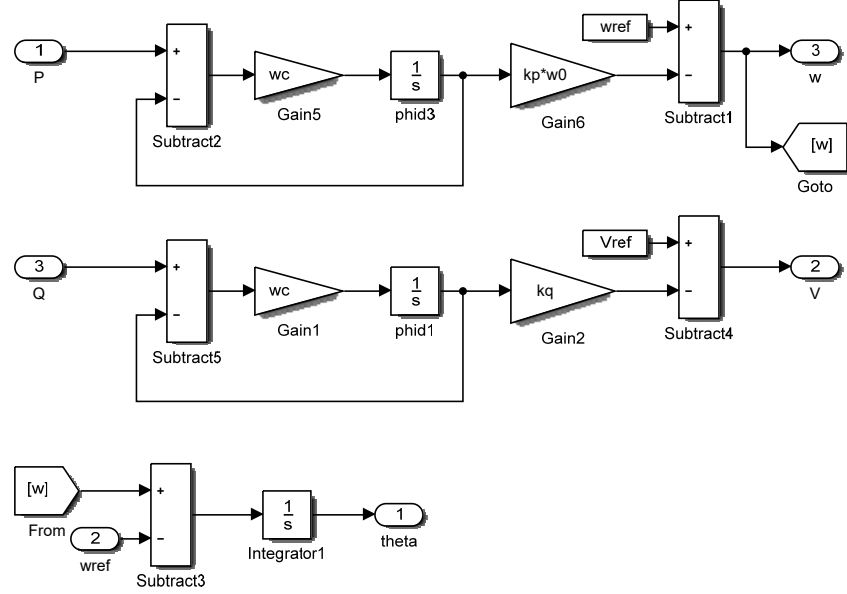


Figure B-1: Simulink model of the droop control in equations (2.16)-(2.18).

B.1.2 dq reference frames

It is more convenient to model AC systems in dq reference frames than stationary reference frames. For modeling the details of the internal control (using the two-bus case as an example), one needs to track the angle shift θ between the reference frames of the inverter and network since the inverter control is referenced to its own rotating frame. That is, the inverter voltage generated by the control needs to be converted to the reference frame of the network. The rotation is normally implemented as follows:

$$\begin{bmatrix} U_d^1 \\ U_q^1 \end{bmatrix} = \begin{bmatrix} \cos \theta & \sin \theta \\ -\sin \theta & \cos \theta \end{bmatrix} \begin{bmatrix} U_d^2 \\ U_q^2 \end{bmatrix} \quad (\text{B.1})$$

where U_d^1 and U_q^1 denote the dq components in first reference frame, U_d and U_q are the dq components in the second reference frame, the angle shift can be tracking using:

$$\theta = \int (\omega^1 - \omega^2) dt \quad (\text{B.2})$$

where ω^1 and ω^2 are the frequency of the two reference frames. For the two-bus case, one may choose the reference frame of the stiff voltage source as the global one to which all the components beside the internal control are referenced. In fact, there is no restriction when choosing a global reference frame; however, for the two-bus example it is convenient to use the stiff voltage source since in steady-state the variables become constant (otherwise one may obtain quasi-steady-state solutions). For modeling multiple inverters, the global reference frame should be aligned with any one of the inverters since there is no stiff voltage source. In this case, for all other inverters, the angle deviations need to be tracked [13].

B.1.3 Networks and loads

After deciding the global reference frame, the dq models of a RL circuit can be realized as:

$$L \frac{dI_d}{dt} = \Delta V_d - RI_d + \omega_0 LI_q \quad (\text{B.3a})$$

$$L \frac{dI_q}{dt} = \Delta V_q - RI_q - \omega_0 LI_d \quad (\text{B.3b})$$

where ω_0 denotes the frequency of the global reference frame and ΔV_d and ΔV_q denote the voltages across the component. Similarly, for a capacitor:

$$C \frac{dV_d}{dt} = \Delta I_d + \omega_0 CV_q \quad (\text{B.4a})$$

$$C \frac{dV_q}{dt} = \Delta I_q - \omega_0 CV_d \quad (\text{B.4b})$$

where ΔI_d and ΔI_q denote the currents flowing into the capacitor. For modeling networks, it is often needed to couple components to a common bus (e.g. a load bus). For example, the following differential equations are realized to implement the circuit

shown in Figure B-2:

$$L_1 \frac{dI_{1,d}}{dt} = V_{1,d} - V_{load,d} + \omega_0 L_1 I_{1,q} \quad (\text{B.5a})$$

$$L_1 \frac{dI_{1,q}}{dt} = V_{1,q} - V_{load,q} - \omega_0 L_1 I_{1,d} \quad (\text{B.5b})$$

$$L_2 \frac{dI_{2,d}}{dt} = V_{2,d} - V_{load,d} + \omega_0 L_2 I_{2,q} \quad (\text{B.5c})$$

$$L_2 \frac{dI_{2,q}}{dt} = V_{2,q} - V_{load,q} - \omega_0 L_2 I_{2,d} \quad (\text{B.5d})$$

with the algebraic equations:

$$0 = V_{load,d} - R_{load}(I_{1,d} + I_{2,d}) \quad (\text{B.6a})$$

$$0 = V_{load,q} - R_{load}(I_{1,q} + I_{2,q}) \quad (\text{B.6b})$$

It can be seen that equations in (B.6) are just algebraic constraints and Simulink can automatically substitute the reduced form of $V_{load,d}$ and $V_{load,q}$ into (B.5) with no issue. Now considering a case where the R_{load} becomes infinite, (B.6) becomes:

$$0 = I_{1,d} + I_{2,d} \quad (\text{B.7a})$$

$$0 = I_{1,q} + I_{2,q} \quad (\text{B.7b})$$

From (B.7), it becomes impossible for Simulink to perform the reduction procedure since $V_{load,d}$ and $V_{load,q}$ no longer exist in the equations. To solve the problem, a dummy resistance of a certain large value can be used (although one should avoid modeling a zero-load bus). Choosing the value for dummy resistances depends on the case: A larger dummy resistance slows down the simulation since the condition number could become fairly large; a small value may affect model fidelity. In this thesis, the dummy resistances are around 100 *pu* based on the Simulink built-in stiff solver *ode23s*. It should also be mentioned that the above issue extends to the coupling of multiple states to form algebraic constraints.

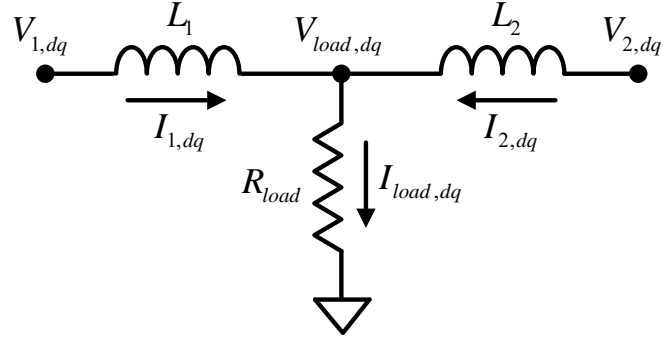


Figure B-2: An example of a load bus

B.2 Small-Signal Analysis

After the construction of the detailed average models in Simulink, time-domain simulation can be naturally performed. In fact, the models can also be used for studying small-signal stability. In order to extract the eigenvalues, steady-state solutions need to be solved first. In this case, the MATLAB *trim* function is particularly useful to solve for system equilibrium points. Then, the procedure can be extended to linearization by using the MATLAB *linmod* function. The function generates four matrices, **A**, **B**, **C**, and **D**, based on the state-space representation of a linearized model:

$$\dot{\mathbf{x}} = \mathbf{Ax} + \mathbf{Bu} \quad (\text{B.8a})$$

$$\mathbf{y} = \mathbf{Cx} + \mathbf{Du} \quad (\text{B.8b})$$

where **x**, **u**, and **y** are the system state vector, input, and output, respectively. Most importantly, the eigenvalues of the matrix **A** (computed through the MATLAB *eig* function) indicate system stability. The main use of this procedure is to draw stability regions as like the one shown in Figure 2-3. In this figure, the droop parameters were sampled from a mesh grid, followed by computing the largest real part of all the eigenvalues. If the value is positive, then the parameter pair is identified as unstable, which should be outside the stability regions.

B.3 Experimental Prototype

B.3.1 System Modules

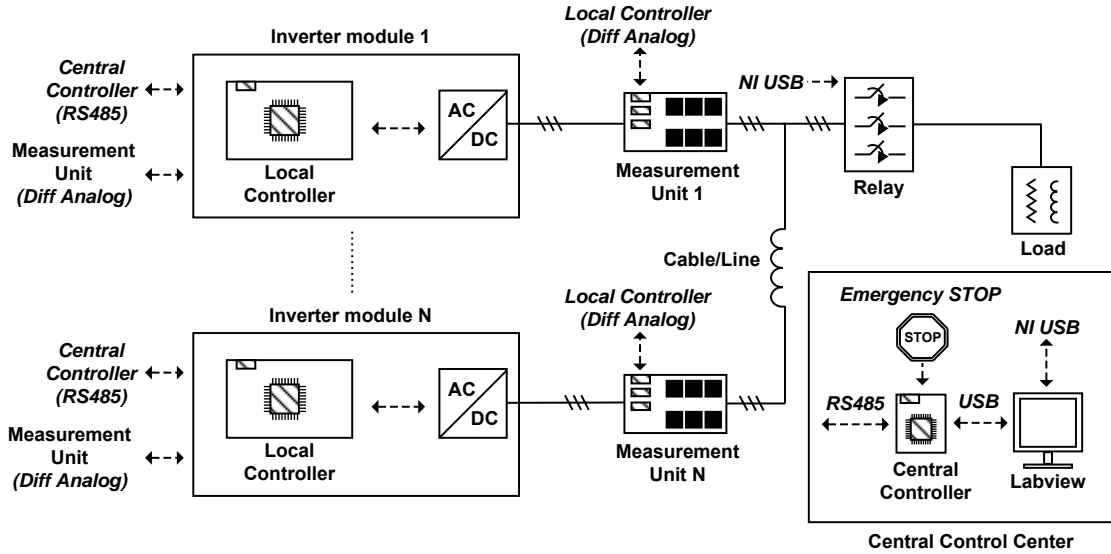


Figure B-3: System diagram of the experimental prototype.

The design of the experimental prototype extends from the testbed built in an author's collaborative project¹ and some similar design principles have been reported in [49]. The system diagram of the experimental prototype is shown in Figure B-3 and the photograph of the prototype is shown in Figure B-4. The functions of different modules are listed as follows:

- Central Control Center: The main objective is to send manual commands to and collect measurement data form the local controllers. More specifically, a central controller board is used to buffer the data exchange between the PC and local controller boards. For monitoring and commanding, a NI LabVIEW based panel is used to operate the testbed.
- Inverter Module: An inverter module consists of a local controller board and an inverter. The local controller board generates PWM signals to the inverter based

¹Great appreciation to Dr. Jorge Elizondo Martinez, Colm O'Rourke, and Matthew Overlin for their efforts and support.

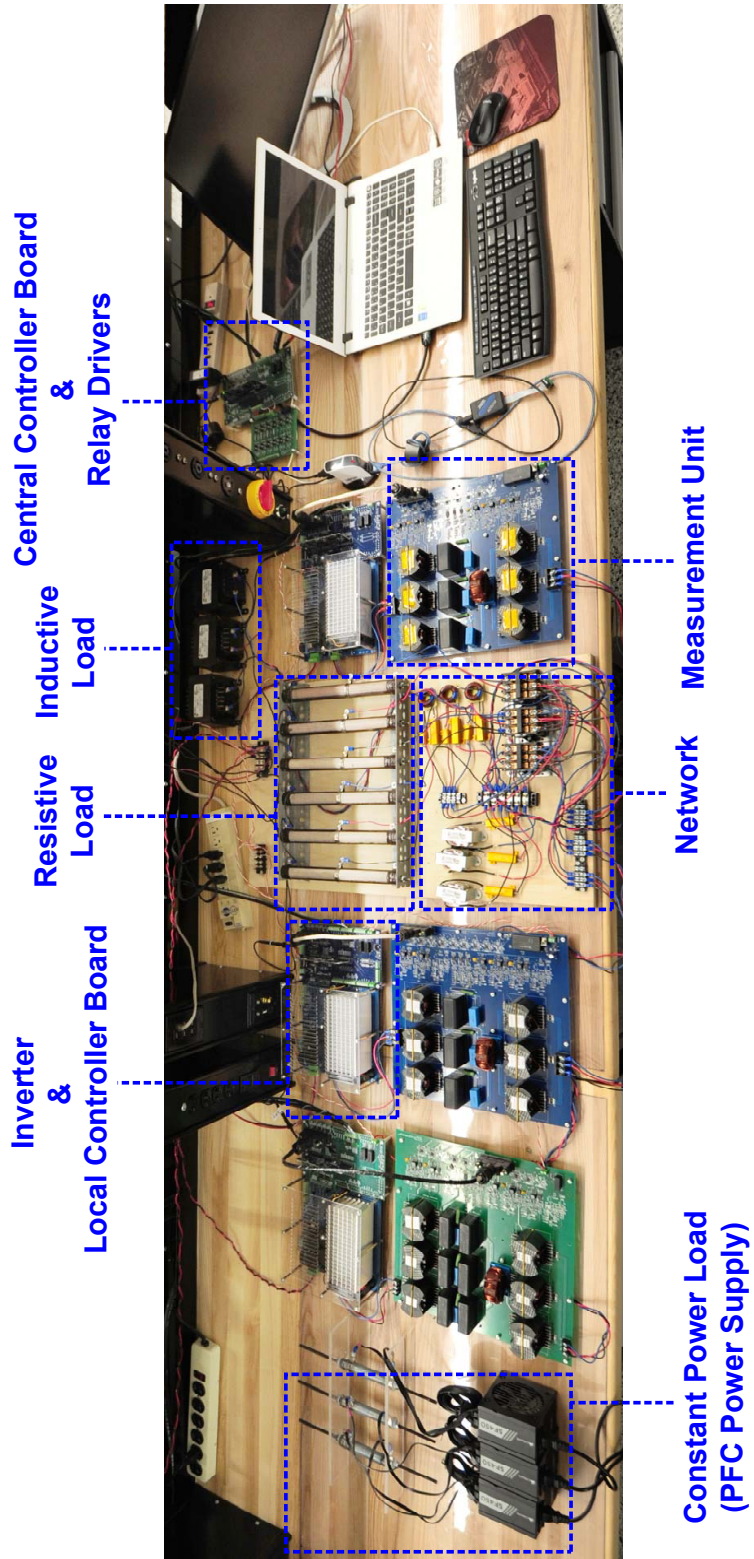


Figure B-4: Photograph of the entire system.

on the programmed control code and also sends (receives) data (commands) to (from) the central control center.

- Measurement Unit: It measures the current and voltage of the *LC* filters and inverter terminal, and transmits the measured signals to its paired local controller.
- Communication and Peripherals: Various types of communication circuits and peripheral modules are used in the system: RS485, USB, GPIO, JTAG, and differential analog transmission.
- Load and Network: To emulate the network and load dynamics.

B.3.2 Central Control Center

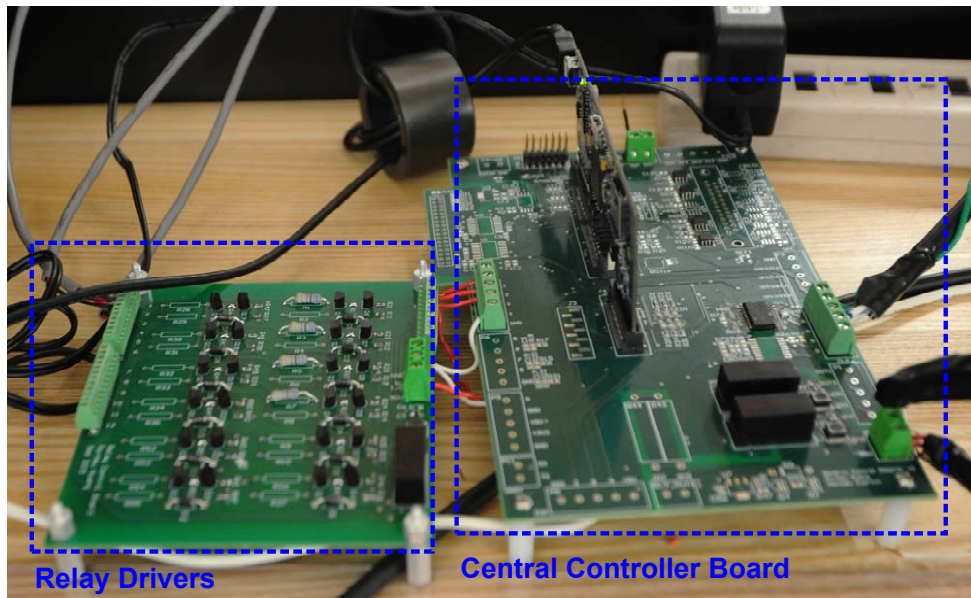


Figure B-5: Photograph of the central controller board and the relay drivers.

The central control center consists of a central controller board and a PC. The central controller board is self-made by using the Texas Instruments C28379D microcontroller (MCU), shown in Figure B-5, and the PC is used to operate the control and monitoring panel by using NI LabVIEW, as shown in Figure B-6. In fact, the

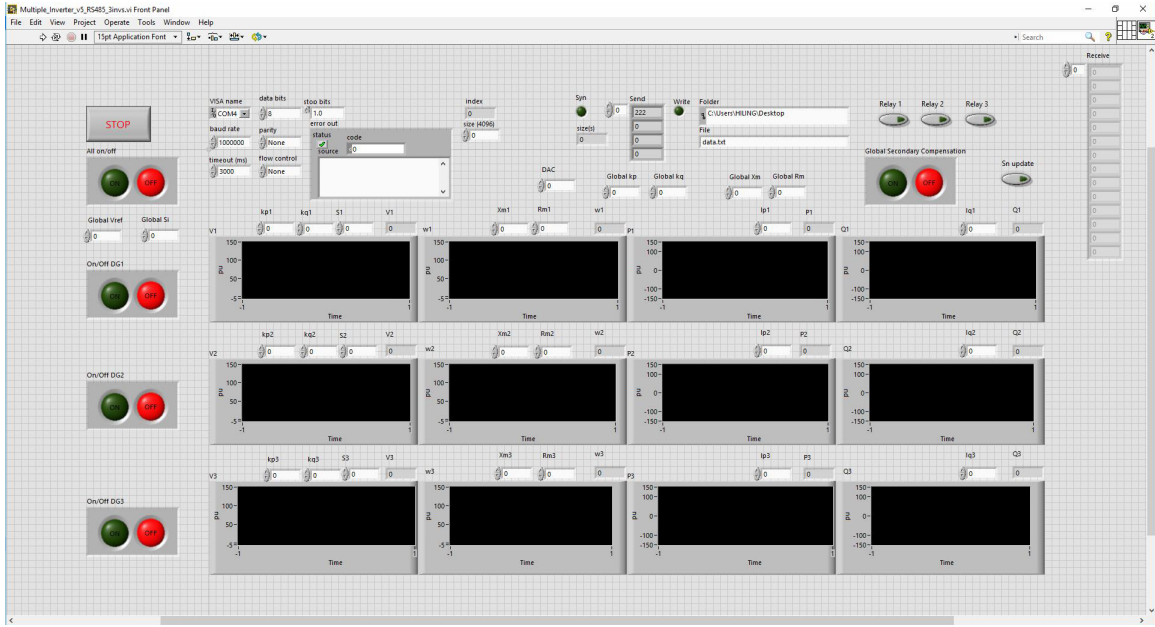


Figure B-6: Screenshot of the LabVIEW control panel.

central controller shares the same board design with the local controller board so that it provides data buffering between local controllers and the LabVIEW control panel. All the local controller boards are physically connected to the central controller board based on the RS485 communication standard so that the central controller can engage with the secondary compensation to allow power dispatch and set-point restoration, as discussed in Chapter 5. In addition, the relay drivers are connected to the GPIO pins of the central controller.

B.3.3 Inverter Module

The inverter module aggregates both a STMicroelectronics STEVAL-IHM028V2 2kW 3-phase inverter unit and a self-made local controller board. The inverter unit, shown in Figure B-7, has an internal Insulated-Gate Bipolar Transistor (IGBT) module that allows direct coupling to the PWM pins of MCUs (with additional ground isolation in this work) without the need of transistor drivers. It also provides the measurement of the DC-link voltage, making any interconnection flexible and convenient.

For the local controller board, it performs multiple functions including sending PWM signals to inverters, collecting data from measurement units, and exchanging

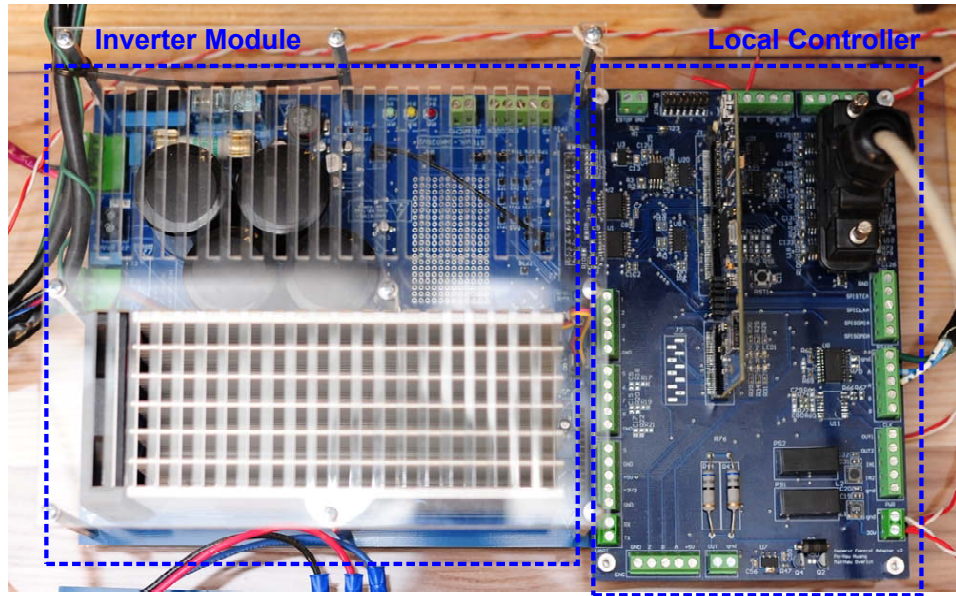


Figure B-7: Photograph of the local controller board and inverter.

data with the central controller, etc. The overall modules of the local controller board are listed:

- Socket for TI C28379D control cards
- RS485 (isolated) and USB interfaces for Universal Asynchronous Receiver/Transmitter (UART) circuits
- Relay drivers
- Digital-to-Analog (DAC) outputs
- Analog-to-Digital (ADC) inputs
- Differential analog receivers (Analog Device AD8130)
- Clock synchronization (isolated)
- PWM signal generation (isolated)

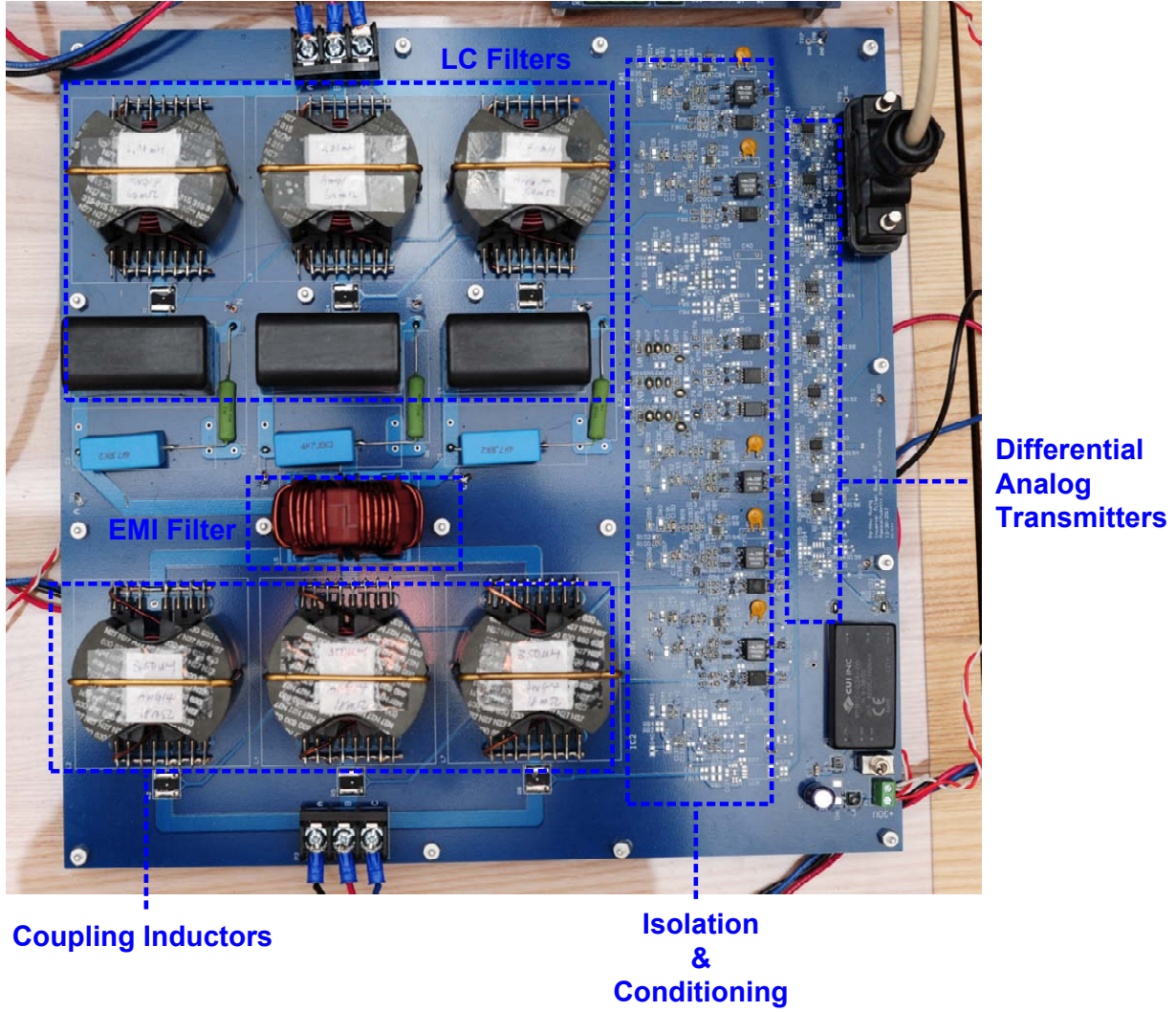


Figure B-8: Photograph of the measurement unit.

B.3.4 Measurement Unit

The measurement unit board is made for mounting the *LCL* components of the inverter and measuring the output current and voltage. The PCB design of the board follows the reference design from Texas Instruments [50]. First, the isolation and conditioning circuits for the voltage and current measurement were implemented by using Texas Instruments AMC1100. The low-voltage signals are transmitted to the local controller board through differential analog transmitters (Analog Device AD8132). A picture of the measurement unit is shown in Figure B-8.

B.3.5 Communication and Peripherals

A list of communication and peripherals used for the experimental prototype is shown:

1. RS485 and UART: They are used for the local controllers to exchange data with the central controller. The RS485 standard is based on differential signals and is suitable in noisy environment (see [49] for more details).
2. Differential Analog Transmission: The measurement signals are transmitted through the differential analog transmission circuits to the local controllers. The differential signals through twisted wires are effective against switching noise generated from PWM controlled inverters.
3. GPIO: The GPIO pins are mainly used to control the peripheral devices and relay drivers.
4. USB: The USB connections are used for the communication between the LabVIEW panel and the central controller.
5. JTAG: It is used to program the TI MCUs.

B.3.6 Load and Network

The inductive behaviors of lines are emulated through a physical set of resistors and inductors, as shown in Figure B-9, whereas the passive loads are implemented in a similar way, shown in Figures B-10 and B-11. In addition, the dynamical behavior of constant power loads is emulated by using commercial power supplies with Power Factor Correction (PFC) features.

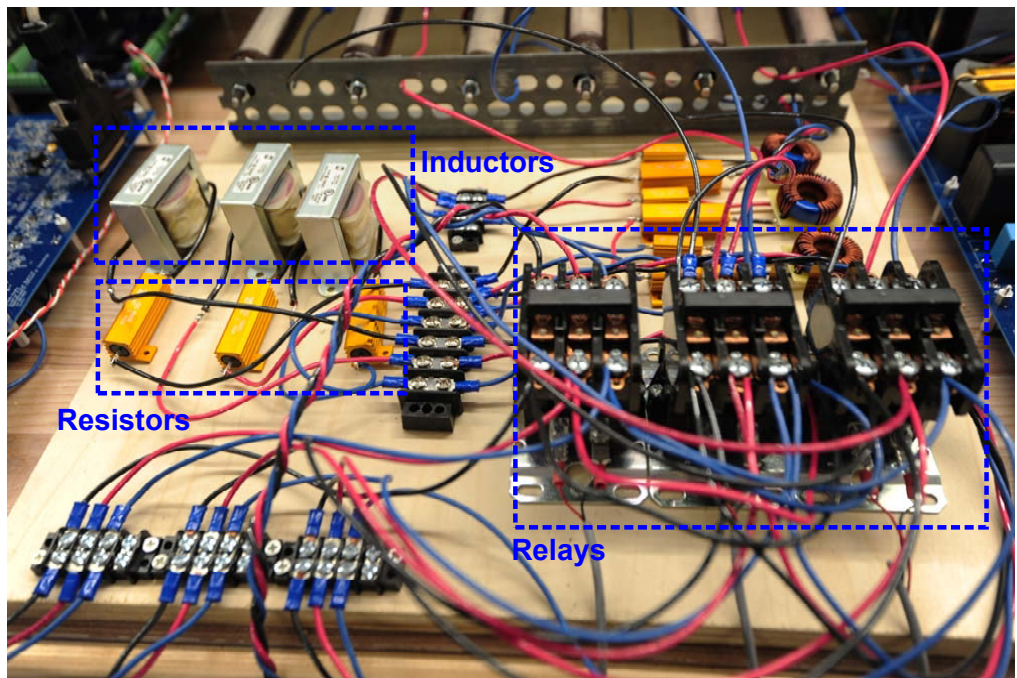


Figure B-9: Photograph of the network.



Figure B-10: Photograph of the inductive load bank.

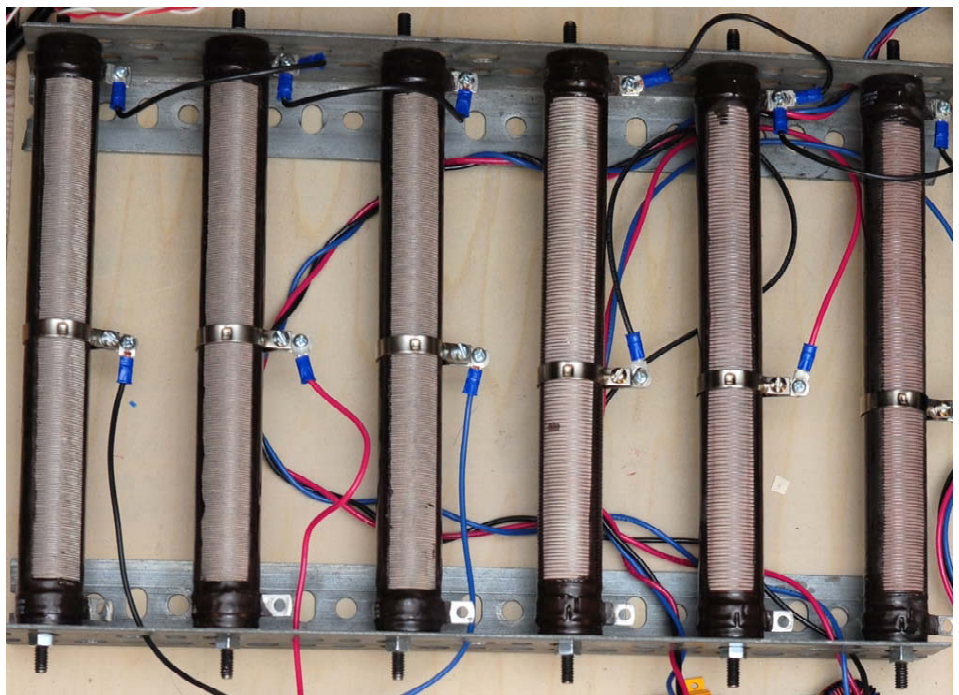


Figure B-11: Photograph of the resistive load bank.

Bibliography

- [1] J. M. Guerrero, J. C. Vasquez, J. Matas, L. G. De Vicuña, and M. Castilla, “Hierarchical control of droop-controlled ac and dc microgrids—a general approach toward standardization,” *IEEE Transactions on Industrial Electronics*, vol. 58, no. 1, pp. 158–172, 2011.
- [2] N. Hatziargyriou, H. Asano, R. Iravani, and C. Marnay, “Microgrids,” *IEEE Power and Energy Magazine*, vol. 5, no. 4, pp. 78–94, 2007.
- [3] R. H. Lasseter, “Smart distribution: Coupled microgrids,” *Proceedings of the IEEE*, vol. 99, no. 6, pp. 1074–1082, 2011.
- [4] M. Smith and D. Ton, “Key connections: The us department of energy? s microgrid initiative,” *IEEE Power and Energy magazine*, vol. 11, no. 4, pp. 22–27, 2013.
- [5] E. Romero-Cadaval, G. Spagnuolo, L. G. Franquelo, C. A. Ramos-Paja, T. Sunto, and W. M. Xiao, “Grid-connected photovoltaic generation plants: Components and operation,” *IEEE Industrial Electronics Magazine*, vol. 7, no. 3, pp. 6–20, 2013.
- [6] D. E. Olivares, A. Mehrizi-Sani, A. H. Etemadi, C. A. Canizares, R. Iravani, M. Kazerani, A. H. Hajimiragha, O. Gomis-Bellmunt, M. Saeedifard, R. Palma-Behnke *et al.*, “Trends in microgrid control,” *IEEE Transactions on Smart Grid*, vol. 5, no. 4, pp. 1905–1919, 2014.
- [7] Y. Zoka, H. Sasaki, N. Yorino, K. Kawahara, and C. C. Liu, “An interaction problem of distributed generators installed in a microgrid,” in *IEEE International Conference on Electric Utility Deregulation, Restructuring and Power Technologies*. IEEE, Apr. 2004, pp. 795–799.
- [8] J. Huang, C. Jiang, and R. Xu, “A review on distributed energy resources and microgrid,” *Renewable and Sustainable Energy Reviews*, vol. 12, no. 9, pp. 2472–2483, 2008.
- [9] S. Parhizi, H. Lotfi, A. Khodaei, and S. Bahramirad, “State of the art in research on microgrids: a review,” *IEEE Access*, vol. 3, pp. 890–925, 2015.

- [10] E. Planas, A. Gil-de Muro, J. Andreu, I. Kortabarria, and I. M. de Alegría, “General aspects, hierarchical controls and droop methods in microgrids: A review,” *Renewable and Sustainable Energy Reviews*, vol. 17, pp. 147–159, 2013.
- [11] R. Majumder, “Some aspects of stability in microgrids,” *IEEE Transactions on Power Systems*, vol. 28, no. 3, pp. 3243–3252, 2013.
- [12] X. Wang, Y. W. Li, F. Blaabjerg, and P. C. Loh, “Virtual-impedance-based control for voltage-source and current-source converters,” *IEEE Transactions on Power Electronics*, vol. 30, no. 12, pp. 7019–7037, 2015.
- [13] N. Pogaku, M. Prodanović, and T. C. Green, “Modeling, analysis and testing of autonomous operation of an inverter-based microgrid,” *IEEE Transactions on Power Electronics*, vol. 22, no. 2, pp. 613–625, 2007.
- [14] M. C. Chandorkar, D. M. Divan, and R. Adapa, “Control of parallel connected inverters in standalone ac supply systems,” *IEEE Transactions on Industry Applications*, vol. 29, no. 1, pp. 136–143, 1993.
- [15] N. Hatziargyriou, *Microgrids: architectures and control*. John Wiley & Sons, 2013.
- [16] J. W. Simpson-Porco, F. Dörfler, and F. Bullo, “Droop-controlled inverters are kuramoto oscillators,” *IFAC Proceedings Volumes*, vol. 45, no. 26, pp. 264–269, 2012.
- [17] Y. Zhang and L. Xie, “Online dynamic security assessment of microgrid interconnections in smart distribution systems,” *IEEE Transactions on Power Systems*, vol. 30, no. 6, pp. 3246–3254, 2015.
- [18] E. Coelho, P. Cortizo, and P. Garcia, “Small-signal stability for parallel-connected inverters in stand-alone ac supply systems,” *IEEE Transactions on Industry Applications*, vol. 38, no. 2, pp. 533–542, 2002.
- [19] J. M. Guerrero, L. G. De Vicuna, J. Matas, M. Castilla, and J. Miret, “A wireless controller to enhance dynamic performance of parallel inverters in distributed generation systems,” *IEEE Transactions on Power Electronics*, vol. 19, no. 5, pp. 1205–1213, 2004.
- [20] V. Mariani, F. Vasca, J. C. Vásquez, and J. M. Guerrero, “Model order reductions for stability analysis of islanded microgrids with droop control,” *IEEE Transactions on Industrial Electronics*, vol. 62, no. 7, pp. 4344–4354, 2015.
- [21] P. Vorobev, P.-H. Huang, M. Al Hosani, J. L. Kirtley, and K. Turitsyn, “High-fidelity model order reduction for microgrids stability assessment,” *IEEE Transactions on Power Systems*, vol. 33, no. 1, pp. 874–887, 2018.

- [22] E. Barklund, N. Pogaku, M. Prodanovic, C. Hernandez-Aramburoand, and T. C. Green, “Energy management in autonomous microgrid using stability-constrained droop control of inverters,” *IEEE Transactions on Power Electronics*, vol. 23, no. 5, pp. 2346–2352, 2008.
- [23] J. He and Y. W. Li, “Analysis, design, and implementation of virtual impedance for power electronics interfaced distributed generation,” *IEEE Transactions on Industry Applications*, vol. 47, no. 6, pp. 2525–2538, Nov. 2011.
- [24] Y. W. Li and C. N. Kao, “An accurate power control strategy for power-electroncis-interfaced distributed generation units operating in a low-voltage multibus microgrid,” *IEEE Transactions on Power Electronics*, vol. 24, no. 12, pp. 2977–2988, 2009.
- [25] J. M. Guerrero, L. G. de Vicuna, J. Matas, M. Castilla, and J. Miret, “Output impedance design of parallel-connected ups inverters with wireless load-sharing control,” *IEEE Transactions on Industrial Electronics*, vol. 52, no. 4, pp. 1126–1135, Aug 2005.
- [26] J. He, Y. W. Li, J. M. Guerrero, F. Blaabjerg, and J. C. Vasquez, “An islanding microgrid power sharing approach using enhanced virtual impedance control scheme,” *IEEE Transactions on Power Electronics*, vol. 28, no. 11, pp. 5272–5282, Nov. 2013.
- [27] H. Tian, Y. W. Li, and P. Wand, “Hybrid ac/dc system harmonics control through grid interfacing converters with low switching frequency,” *IEEE Transactions on Industrial Electronics*, vol. PP., no. 99, pp. 1–1, 2017.
- [28] W. Yao, M. Chen, J. Matas, J. M. Guerrero, and Z.-M. Qian, “Design and analysis of the droop control method for parallel inverters considering the impact of the complex impedance on the power sharing,” *IEEE Transactions on Industrial Electronics*, vol. 58, no. 2, pp. 576–588, 2011.
- [29] J. McElligatt, “Application report: Selection and specification of crystals for texas instruments usb 2.0 devices,” Texas Instrument, Tech. Rep. SLLA122, December 2002.
- [30] J. Kim, J. M. Guerrero, P. Rodriguez, R. Teodorescu, and K. Nam, “Mode adaptive droop control with virtual output impedances for an inverter-based flexible ac microgrid,” *IEEE Transactions on Power Electronics*, vol. 26, no. 3, pp. 689–701, 2011.
- [31] X. Guo, Z. Lu, B. Wang, X. Sun, L. Wang, and J. M. Guerrero, “Dynamic phasors-based modeling and stability analysis of droop-controlled inverters for microgrid applications,” *IEEE Transactions on Smart Grid*, vol. 5, no. 6, pp. 2980–2987, 2014.

- [32] J. Machowski, J. Bialek, and J. Bumby, *Power system dynamics: stability and control*. John Wiley & Sons, 2011.
- [33] N. Bottrell, M. Prodanovic, and T. C. Green, “Dynamic stability of a microgrid with an active load,” *IEEE Transactions on Power Electronics*, vol. 28, no. 11, pp. 5107–5119, 2013.
- [34] N. Jayawarna, X. Wu, Y. Zhang, N. Jenkins, and M. Barnes, “Stability of a microgrid,” in *IET International Conference on Power Electronics, Machines and Drives*. IET, 2006, pp. 316–320.
- [35] Y. Zhang, L. Xie, and Q. Ding, “Interactive control of coupled microgrids for guaranteed system-wide small signal stability,” *IEEE Transactions on Smart Grid*, vol. 7, no. 2, pp. 1088–1096, 2016.
- [36] J.-J. Slotine and W. Li, *Applied Nonlinear Control*. Prentice-Hall, 1991.
- [37] I. P. Nikolakakos, H. H. Zeineldin, M. S. El-Moursi, and N. D. Hatziargyriou, “Stability evaluation of interconnected multi-inverter microgrids through critical clusters,” *IEEE Transactions on Power Systems*, vol. 31, no. 4, pp. 3060–3072, 2016.
- [38] S. Gataric and N. R. Garrigan, “Modeling and design of three-phase systems using complex transfer functions,” in *IEEE Power Electronics Specialists Conference*. IEEE, 1999, pp. 691–697.
- [39] J. M. Guerrero, M. Chandorkar, T.-L. Lee, and P. C. Loh, “Advanced control architectures for intelligent microgrids part i: Decentralized and hierarchical control,” *IEEE Transactions on Industrial Electronics*, vol. 60, no. 4, pp. 1254–1262, 2013.
- [40] S. Anand, B. G. Fernandes, and J. Guerrero, “Distributed control to ensure proportional load sharing and improve voltage regulation in low-voltage dc microgrids,” *IEEE Transactions on Power Electronics*, vol. 28, no. 4, pp. 1900–1913, April 2013.
- [41] J. A. Belk, W. Inam, D. J. Perreault, and K. Turitsyn, “Stability and control of ad hoc dc microgrids,” in *IEEE 17th Workshop on Control and Modeling for Power Electronics (COMPEL)*, June 2016.
- [42] P. Huang, P. Liu, W. Xiao, and M. S. E. Moursi, “A novel droop-based average voltage sharing control strategy for dc microgrids,” *IEEE Transactions on Smart Grid*, vol. 6, no. 3, pp. 1096–1106, May 2015.
- [43] A. Giusti, M. Salani, G. A. D. Caro, A. E. Rizzoli, and L. M. Gambardella, “Restricted neighborhood communication improves decentralized demand-side load management,” *IEEE Transactions on Smart Grids*, vol. 5, no. 1, pp. 92–101, 2014.

- [44] C. Yuen, A. Oudalov, and A. Timbus, “The provision of frequency control reserves from multiple microgrids,” *IEEE Transactions on Industrial Electronics*, vol. 58, no. 1, pp. 173–183, Jan 2011.
- [45] T. A. Papadopoulos, G. K. Papagiannis, and P. S. Dokopoulos, “Low-voltage distribution line performance evaluation for plc signal transmission,” *IEEE Transactions on Power Delivery*, vol. 23, no. 4, pp. 1903–1910, Oct 2008.
- [46] C. Chen, Y. Wang, J. Lai, Y. Lee, and D. Martin, “Design of parallel inverters for smooth mode transfer microgrid applications,” *IEEE Transactions on Power Electronics*, vol. 25, no. 1, pp. 6–15, Jan 2010.
- [47] S. Anand, B. G. Fernandes, and J. Guerrero, “Distributed control to ensure proportional load sharing and improve voltage regulation in low-voltage dc microgrids,” *IEEE Transactions on Power Electronics*, vol. 28, no. 4, pp. 1900–1913, April 2013.
- [48] P. Vorobev, P. Huang, M. A. Hosani, J. L. Kirtley, and K. Turitsyn, “A framework for development of universal rules for microgrids stability and control,” in *IEEE 56th Annual Conference on Decision and Control (CDC)*, Dec 2017, pp. 5125–5130.
- [49] J. E. Martinez, “Microgrid operation strategy for improved recovery and inertial response after large disturbances,” Ph.D. dissertation, Massachusetts Institute of Technology, June 2016.
- [50] “Isolated current and voltage measurement using fully differential isolation amplifier,” Texas Instrument, Tech. Rep. TIDUA58, August 2015.